SIEMENS FINAL DESIGN REPORT

Team Angel One

Ryan Stouffer

Nicholas Lipari

Preetam Kar

Alek Garabet

Toby Coombs

Andrew Olijarczyk

April 29, 2026

TABLE OF CONTENTS

LIST OF TABLES

LIST OF FIGURES

Abstract

This report outlines the conceptual design and preliminary performance evaluation of a Medium-Altitude Long-Endurance (MALE) unmanned aerial vehicle (UAV) intended to satisfy specified Intelligence, Surveillance, and Reconnaissance (ISR) mission objectives. Designed for operations at 30,000 ft MSL, the aircraft must sustain an 8-hour circular orbit with a 10-mile radius while supporting a suitcase-sized EO/IR sensor payload. Four design concepts were generated and shown to meet the performance and feasibility requirements set by Siemens. This report also discusses the evolution of the project through the conceptual, interim, and final design stages, documenting the major design decisions and refinements that led to the development of the final UAV configuration.

Introduction

This report presents the conceptual design and analysis of the Angel One Medium-Altitude Long-Endurance (MALE) unmanned aerial vehicle (UAV) for Intelligence, Surveillance, and Reconnaissance (ISR) missions. The goal is to develop a system that meets performance requirements such as range, endurance, and payload capability while maintaining compliance with relevant safety and regulatory standards.

The UAV is designed to operate at 30,000 ft and sustain extended surveillance missions. Multiple design configurations were developed and refined through iterative analysis, focusing on aerodynamic efficiency, propulsion performance, and system integration. Overall, this report outlines the design process, key engineering decisions, and performance evaluations that led to the final UAV configuration.

CHAPTER I – CONCEPTUAL DESIGN REPORT

1.0 Design Requirements & Stakeholders

1.1 Design Requirements

The following requirements define the performance, mission, and operational characteristics of the Angel One Intelligence, Surveillance, and Reconnaissance (ISR) UAV System [7].

Range

- The AO ISR System shall meet a minimum total mission range of 750 miles, including outbound travel, ISR orbit time, and return.
- The aircraft must also meet a baseline system range of 1,125 nmi under standard cruise conditions.

Payload

- Payload consists of the EO/IR sensor package approximately the size of a suitcase along with required mission avionics.
- The electrical system must supply 12 VDC for 8 hours to support the payload and flight controls.

Takeoff & Landing Distances

- Takeoff distance: ≤ 2,345 ft
- Landing distance: ≤ 2,250 ft
- Must operate from runways ≥ 5,000 ft in length at elevations ≤ 6,000 ft MSL and temperatures ≤ 100°F.

Maximum Takeoff Weight (MTOW)

- MTOW shall support the complete mission (fuel, payload, and margins) while remaining within stated performance capabilities.

Cruise Speed

- Maximum cruise speed: 370 kn
- Never-exceed speed: 285 kn IAS, Mmo 0.64

Climb Speed / Rate of Climb

- Rate of climb: 3,424 ft/min
- System must reach an operational altitude of 30,000 ft MSL prior to entering orbit.

Operational Ceiling

- The aircraft shall have a service ceiling of 41,001 ft.

1.2 Applicable Regulatory and Certification Standards

In an effort to comply with the widest range of possible regulatory standards, the Angel One UAV will be preliminarily designed to comply with multiple aviation regulatory frameworks, including those outlined by Siemens, civil aviation regulations, military standards, and industry certification guidelines.

1.21 Federal Aviation Administration (FAA)

For aircraft operating in United States airspace, several FAA regulations are relevant.

- 14 CFR Part 23 establishes airworthiness standards for normal category aircraft, including requirements related to structural loads, flight performance, stability, and control. For example, the ultimate loads, which are equal to the limit loads multiplied by a 1.5 factor of safety, must be specified. [11].

- 14 CFR Part 25 defines certification standards for transport category aircraft and includes detailed requirements regarding structural integrity, system reliability, and operational safety. For example, a 90-degree cross component of wind velocity, demonstrated to be safe for takeoff and landing, must be established for dry runways and must be at least 20 knots or 0.2 V_{SR0}, whichever is greater, except that it need not exceed 25 knots. [12].

Operational regulations may also apply depending on the mission scenario. 14 CFR Part 91 provides general operating rules for aircraft operations within civil airspace [13], while 14 CFR Part 107 defines regulations governing small, unmanned aircraft systems and may influence certain mission operations [14]. While this small, unmanned category is likely less applicable for our larger UAV, it is still worth noting in the case of future design changes.

1.22 European Aviation Safety Agency (EASA)

- For potential international certification or operations in European airspace, guidance may also be derived from the EASA Certification Specifications for CS-23 and CS-25 aircraft. These regulations largely mirror FAA standards and define performance, structural, and operational safety requirements. These regulations standardize metrics for takeoff, landing, and structural loading. Landing performance is defined from 50 ft above to a full stop, and operational landing distance typically requires a safety margin of about 1.68 times the demonstrated landing distance to ensure runway availability. Structural sizing is guided by maneuver load factors of around +3.8g and –1.5g for normal category aircraft. Certification performance requirements also include minimum climb gradients of around 2.4% to ensure clearance during takeoff [15].

- EASA also provides Special Condition Light UAS (SC-LUAS) regulations for unmanned aircraft systems; however, these are primarily intended for smaller platforms and may be less applicable for the larger UAV considered here. Aircraft of this class are generally expected to achieve safety levels comparable to manned aircraft including catastrophic failure probabilities on the order of 10^{-9} failures per flight hour. For UAVs in the business, jet size cruise altitudes fall within the range of 25,000-50,000 ft [16].

1.23 Military Standards

Because the UAV is expected to support ISR missions, military certification and operational standards are also relevant, imposing specific structural and environmental thresholds:

- MIL-STD-1797: Provides guidelines for aircraft flying qualities and stability characteristics. To satisfy these control requirements, structural sizing is guided by maneuver load factors of around +3.8g and -1.5g. [17]
- MIL-STD-810: Outlines environmental testing procedures covering temperature, humidity, vibration, and other operational stresses [18]. Under this standard, the aircraft systems must safely withstand the following:
    - Temperature extremes ranging from -60°F to 140°F.
    - A 200-cycle salt/fog corrosion exposure requirement.

- Exposure to corrosive and harsh chemicals, including JP-8 fuel, hydraulic fluid, oxidizers, refrigerants, and hot gases.
- Environmental hazards including lightning strikes, ice, sand, and dust exposure.

- MIL-HDBK-516C: Defines airworthiness certification criteria applicable to both manned and unmanned military aircraft. This ensures system safety and reliability during ISR missions over populated areas and environmentally sensitive regions [19].

1.24 NATO Standards

In addition, NATO interoperability and airworthiness standards may influence system architecture:

- STANAG 4671 establishes airworthiness requirements for unmanned aircraft systems from weights of 150kg to 20,000kg [20]. The UAV falls into a Class 1 specification, requiring rigorous safety procedures during each phase of flight. This document segments failures into four different types, each with their own probabilities and classes. These failure conditions and probabilities are as follows:
  - Catastrophic failures shall occur $\leq 10^{-6}$ per flight hour
  - Hazardous failures shall occur $\leq 10^{-5}$ per flight hour
  - Major failures shall occur $\leq 10^{-4}$ per flight hour
  - Minor failures shall occur $\leq 10^{-3}$ per flight hour

To achieve these thresholds, the aircraft must limit load maneuvering, getting a load factor less than 3.8. In a single engine UAV, the engine must rotate no less than the stalling speed during take-off configuration and have a landing gear designed for a

$W^{\frac{1}{6}}$ limiting descent velocity of $4.4\ (\,)$. Additionally, this document outlines the ground

s

control requirements for the aircraft. This system shall consist of the following: a command-and-control data link, a communication system, UAV control station, and additional ancillary elements.

- STANAG 4586 defines standardized communication and control interfaces for UAV ground control systems, enabling interoperability with NATO ISR networks [21]. The specification classifies levels of interoperability into five levels. These levels of interoperability (LOI) are as follows:
  - Level 2: Direct receipt of ISR.
  - Level 3: Control and monitoring of the UAV payload.
  - Level 4: Control and monitoring of the UAV itself, excluding launch and recovery.
  - Level 5: Full control, including launch and recovery functions.

Because the UAV must respond to changing operating conditions, low-latency control is required. For the 1,000–10,000 kg class, the maximum delay from operator input to aircraft response is 200ms.

1.25 Industry Certification Standards

Commercial aerospace certification guidelines also play a critical role in avionics and equipment qualification. The following standards ensure the reliability and operational safety of onboard avionics and flight control systems.

- RTCA DO-160 defines environmental testing procedures for airborne electronic equipment. The systems that are designed to meet DO-160 environmental categories are:
    - Flight computer
    - Navigation Systems (GPS / INS)
    - Sensors (IMU, pressure, air data systems)
    - Power electronics
    - Optical package
    - Communication equipment

All the listed components above should be tested or designed to survive in varying temperatures, vibrations and electromagnetic conditions. For temperature and altitude tolerance, the avionics should operate across a temperature range of −55 °C ground-survival temperature, to +85 °C operating temperatures, and 55,000 ft altitude under a temperature/altitude test category [22]. This means that the designs should include thermal management, electronics rated for a wide range of temperatures and altitudes and environmental enclosure if the electronics are external. Vibration protection [22] should include vibration isolated avionics mounts, rubber dampers or shock mounts and structural mounts for electronics. These should provide protection for IMUs, flight computers, optical packages and communication equipment. Electrical protection [22] provides protection against voltage spikes, noise and electrical disturbances. The system will include voltage regulation, surge protection, power filtering and proper grounding. This will protect the avionics from generator spikes, motor/engine noise, lighting strikes and electromagnetic interferences. Environmental protection [22] will include protection from moisture, humidity, dust and water exposure that are listed in the client's requirements [7]. Sealed avionics bays, conformal coating on circuit boards and environmental enclosures are affective ways to protect the aircraft's avionics from environmental factors.

- RTCA DO-178C establishes rigorous standards for airborne software certification and safety assurance. DO-178C is the classification of software based on the severity of failure conditions, which determines how rigorous the development and verification processes must be [23]. The 5 design assurance levels are:
    - Level A – Catastrophic failure condition
    - Level B – Hazardous or severe-major failure condition
    - Level C – Major failure condition
    - Level D – Minor failure condition
    - Level E – No safety effect

For higher criticality levels require more extensive verification, documentation and testing. DO178C does not tell us which hardware to incorporate into the aircraft's design, but it defines how the aircraft's software must be developed and verified. Therefore, the UAV's systems should have reliable flight control software, verified and test software, documented software architecture, fault handling and safety logic.

1.3 Stakeholders

The AO ISR System must satisfy the needs and constraints of all major stakeholders involved in the aircraft's lifecycle, operation, and societal impact [7].

Public Health, Safety, and Welfare

- Systems must safely withstand environmental hazards such as:
  - Lightning strikes
  - Corrosive/harsh chemicals, including JP-8 fuel, hydraulic fluid, oxidizers, refrigerants, salt fog, and hot gases
  - Temperature extremes from –60°F to 140°F
  - Ice, sand, and dust exposure
- System safety ensures reliability during ISR missions over populated areas and environmentally sensitive regions.

Global, Social, and Environmental Impact

- Use of JP-8 fuel requires consideration of emissions and environmental impact.
- Material selection and corrosion control to minimize environmental degradation over the aircraft's lifetime.
- ISR operations may impact regional security, requiring compliance with ethical surveillance standards.

Economic Factors

- Target unit cost: <$20M ±5%

End User Considerations

- Designed for reliability and ease of operation by:
    - Ground crew
    - Remote pilot/flight

    crew
    - ISR operators

1.4 Motivation

Economic Factors

Global demand for UAV systems continues to rise, accelerated by recent conflicts such as the Russia–Ukraine war, which highlighted the operational value of unmanned platforms. Industry forecasts estimate 8.2 billion USD in worldwide UAV spending by 2025, with the U.S. contributing 1.9 billion USD (23.8%) [1]. Economically, UAVs reduce total lifecycle costs by offering multimission capability on a single airframe, limiting the need for multiple specialized platforms. Their ability to provide faster response times and improved data continuity further enhances operational efficiency and overall value for both defense and commercial users.

Military Factors

From a defense standpoint, UAVs offer clear advantages by eliminating pilot exposure in highthreat environments, enabling safer operations in contested airspace. Additionally, UAVs provide greater operational flexibility without requiring major fleet expansion, as modular payloads and long endurance allow a single platform to meet diverse mission requirements.

2.0 Benchmarking and Technology Availability

2.1 Benchmarking Analysis

To inform the conceptual design of the Angel One UAV, several existing aircraft were analyzed to benchmark key performance characteristics, structural configurations, and aerodynamic efficiencies.

2.1.1 General Atomics MQ-9 Reaper

The MQ-9 Reaper serves as the standard benchmark for long-endurance Intelligence, Surveillance, and Reconnaissance (ISR) dominance [10], [27], [31]:

- Max Endurance: 27 hours
- Range: 1,150 nautical miles
- Maximum Takeoff Weight (MTOW): 10,500lbs
- Engine: 910 SHP Honeywell TPE331-10 turboprop
- Wingspan: 66 ft

Design Takeaway: This aircraft demonstrates the effectiveness of combining a high aspect ratio wing with a fuel-efficient turboprop to achieve long-endurance ISR capabilities at medium altitudes.

2.1.2 WZ-9 "Divine Eagle"

The Chinese WZ-9 "Divine Eagle" was analyzed as an "anti-stealth" precedent. It utilizes a twin fuselage "catamaran" configuration with a single dorsal turbofan [32], [33]:

- Wingspan: 45 m (148 ft)
- Endurance: 30+ Hours
- Service Ceiling: 60,000 ft (18 km)

Design Takeaway: The WZ-9 demonstrates that large composite structures can achieve highaltitude persistence

2.1.3 Scaled Composites Model 281 "Proteus"

The Scaled Composites Proteus acts as a "structural" validator for design [34], [35]:

- Service Ceiling: 61,000+ ft (Record: 63,245 ft)
- Endurance: 14+ Hours (Loitering at 50,000 ft)
- Payload Capacity: 2,000lbs carried on an external pylon
- Empty Weight: 5,900lbs

Design Takeaway: The Proteus validates that a multi-boom airframe constructed from graphiteepoxy composites can achieve extreme altitudes.

2.1.4 Rutan Model 61 "Long-EZ"

The Rutan Long-EZ provides an "efficiency" benchmark [36], [37]:

- Max Range: 2,000 miles
- Fuel Efficiency: 2,000 miles on only 52 gallons of fuel
- Empty Weight: 710lbs
- Engine: Small 115 hp Piston (Lycoming 0-235)

Design Takeaway: The Long-EZ proves that a canard configuration offers superior aerodynamic efficiency for long range missions compared to conventional tail designs.

2.2 Technology Readiness and Availability

To ensure the feasibility of the Angel One concept, key systems were evaluated based on their Technology Readiness Level (TRL).

2.2.1 Structure

Carbon Fiber / Graphite-Epoxy Composites (TRL 9)

- Feasibility: Fully validated by various aircraft such as the Scaled Composites Proteus for high altitude operations [34], [35].

- Implementation: Chosen specifically because it can meet the 200-cycle salt/fog corrosion requirement without the need for heavy protective coatings, offering a distinct advantage over aluminum.

2.2.2 Propulsion

Small Turboprop (TRL 9)

- Feasibility: Represents mature technology commonly found in existing UAV benchmarks as well as the "Personal Jet" class.
- Implementation: Provides optimal propulsive efficiency and specific fuel consumption at low to medium subsonic speeds while operating on standard JP-8 fuel [2].

2.2.3 Flight Controls

Adaptive Flight Control Systems (TRL 7-8)

- Feasibility: Modern adaptive control algorithms are robust. However, implementing them for long endurance composite airframes requires specific tuning to guarantee rapid settling times and adequate disturbance rejection.
- Implementation: Crucial for managing the aircraft during operation via the onboard flight control computer and autopilot. This level of software maturity is necessary to ensure stability during prolonged missions.

3.0 Conceptual Sketches & Sizing Estimations

3.1 Conceptual Design 1

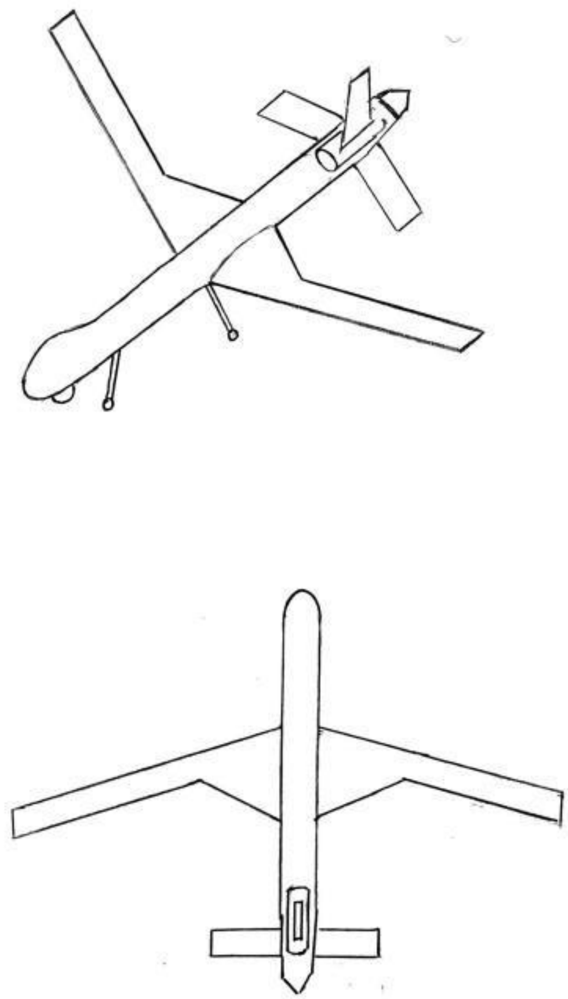

Figure 1. Conceptual top view and isometric drawing of Design 1, a high-aspect ratio turboprop ISR UAV configuration inspired by the general arrangement of the MQ-9 Reaper.

3.1.1 Overview

The first conceptual design is inspired by top of the market military UAVs including the MQ-9 Reaper. This design is a medium altitude, long endurance (MALE) turboprop UAV optimized for the missions at 30,000 ft and long transit range, as specified in the design requirements [7]. The configuration emphasizes aerodynamic efficiency with a high aspect ratio wing and moderate cruise speed.

3.1.2 Geometric Characteristics and Layout

Following the traditional component layout of the UAVs making up the top of today's market, the nose of the aircraft will house all electronics and communications systems. This includes internal systems such as the battery and avionics as well as external ones such as the EO/IR payload system. Fuel will be stored in the center of the aircraft as well as in the wings, made possible by the thick root chord design. Finally, the rear of the aircraft features an inverted y-tail chosen for its stability and control. However, this design selection would require additional thought to prevent any issues with obstructing landing and takeoff procedures. It should be noted that this selection was made primarily out of an attraction to appearance rather than any truly sound technical analysis.

Table 1: Design 1 Geometric Characteristics

Parameter	Value
Wingspan	60 ft
Length	40 ft
Fuselage diameter	4 ft
Aspect ratio, AR	16.7
Wing mean chord length	4.17 ft
Wing root chord	8 ft
Wing tip chord	2.33 ft
Wing area, S	215.66 ft^2
Wing loading, W/S	20.87 lb/ft^2
Maximum takeoff weight (MTOW)	4,500 lb
Empty weight	1,500 lb
Fuel capacity	1,500 lb
Payload (EO/IR)	500 lb

3.1.3 Weight Breakdown

Table 2: Design 1 Weight Segment Breakdown

Segment	Power (hp)	BSFC	Fuel (lb)	W_{start}	W_{end}
Takeoff	–	–	90.0	4500.0	4410.0
Transit to orbit	106.7	0.48	119.5	4410.0	4290.5
Orbit loiter (8 hr, 10-mi radius)	88.5	0.42	297.3	4290.5	3993.2
Transit return	91.9	0.48	108.2	3993.2	3885.0
Landing	–	–	20.0	3885.0	3865.0
		Total fuel used:	**635.0 lb**	**Fuel remaining: 865.0 lb**	

A 33% fuel fraction is consistent with range and endurance focused turboprop UAVs. It is worth noting that this number may likely be adjusted in the future considering too much fuel is left per mission. As seen in Table 2, the fuel fraction used is less than the total fuel capacity, even considering a 5% unusable amount. The primary reason for such a large fuel capacity is the fact that the UAV will not be carrying weapons like most UAVs this design is being based on. A weight of 1000lb is left for the engine, landing gear, electronics, and communications systems.

3.1.4 Aerodynamic Characteristics

Table 3: Design 1 Mission Segment Aerodynamic Characteristics

Segment	C_L	L/D	Alt (ft)	TAS (kt)	End (hr)	Range (nmi)
Takeoff	–	–	0–30000	–	–	–
Transit to orbit	1.135	18.925	30000	128.6	2.333	300
Orbit loiter (8 hr, 10-mi radius)	1.600	17.864	30000	105.7	8.000	845.6
Transit return	1.135	18.925	30000	122.4	2.452	300
Landing	–	–	30000–0	–	–	–

Table 4: Design 1 General Aerodynamic Characteristics

Coefficient	Value
Lift coefficient, C_L	0.808
Drag coefficient, C_D	0.045
Lift-to-drag ratio, L/D	17.88
Zero-lift drag coefficient, C_{D0}	0.030
Efficiency Factor, e	0.80
Induced drag factor, k	0.0233
Maximum lift coefficient, $C_{L,\max}$	1.6
Pitching moment coefficient, C_M	-0.05
Propulsive efficiency, η_p	0.85

The aerodynamic parameters used in the preceding performance calculations were estimated using the methods outlined by Raymer and others [2], [4], [8]. Empirical relationships for lift and drag estimations were applied to obtain realistic values for C_L, C_D and L/D. Aircraft range and endurance were calculated using the Breguet range and endurance equations as presented in the same reference. The selected wing airfoil is the NLF (1)-0115 natural laminar flow airfoil. This airfoil was chosen to promote extended laminar flow over a significant portion of the chord, thereby reducing drag and improving efficiency. Its 15% thickness-to-chord ratio provides adequate internal volume and structural depth for spars while maintaining favorable aerodynamic performance characteristics.

3.1.5 Propulsion Characteristics

The propulsion system selected for this design is the 850 hp Pratt & Whitney PT6A-42, a mediumclass turboprop widely used in both civil and military aviation. This engine was chosen due to its extensive operational history, high demonstrated reliability, and the availability of a global maintenance network. The engine power rating is well aligned with comparable UAV systems currently in service. For example, the MQ-9 Reaper, a benchmark in the ISR domain, employs a Honeywell TPE331-10 turboprop producing approximately 950 hp [27]. The PT6A-42 delivers similar performance while offering a favorable combination of size, weight, and fuel efficiency compatible with the design constraints of this UAV concept [6], [24].

3.1.6 Subsystems

In addition to the primary airframe, propulsion, and payload systems, several supporting subsystems are required to ensure the UAV satisfies mission requirements. In the interest of transparency, subsystem design was not explored in the same depth as aerodynamics and propulsion. However, reasonable preliminary selections consistent with MALE class UAVs were made. The design will incorporate an internal fuel storage system consisting of a central fuselage tank along with distributed wing-integrated fuel tanks. This was chosen to maintain favorable mass properties and minimize CG variability across mission profiles. The electrical power subsystem uses a 28V generator to power avionics, flight controls, and payload systems.

The landing gear subsystem is a retractable, electrically powered tricycle configuration. Electric power was selected for its resistance to harsh environmental conditions, while retraction reduces drag and supports long endurance performance [2]. The flight control and avionics subsystem incorporate redundant flight computers, GPS navigation, and data link capability for ISR operations. Finally, basic environmental and anti-ice provisions, such as pitot heating, are included to ensure operability at altitude.

3.1.7 Cost

Cost estimation for this aircraft is among the more challenging aspects of the design process, largely because detailed cost data for UAV subsystems and military grade technologies are not publicly available. To determine a rough estimate, UAV cost metrics presented in the *DoD Unmanned Aerial Vehicles Roadmap* were used. This article presents estimates of approximately $1,500 per pound of empty weight and $8,000 per pound of payload capacity for typical Department of Defense unmanned aircraft [3]. These values were used to determine a rough cost of $10 million USD per the weight breakdown provided previously.

3.2 Conceptual Design 2

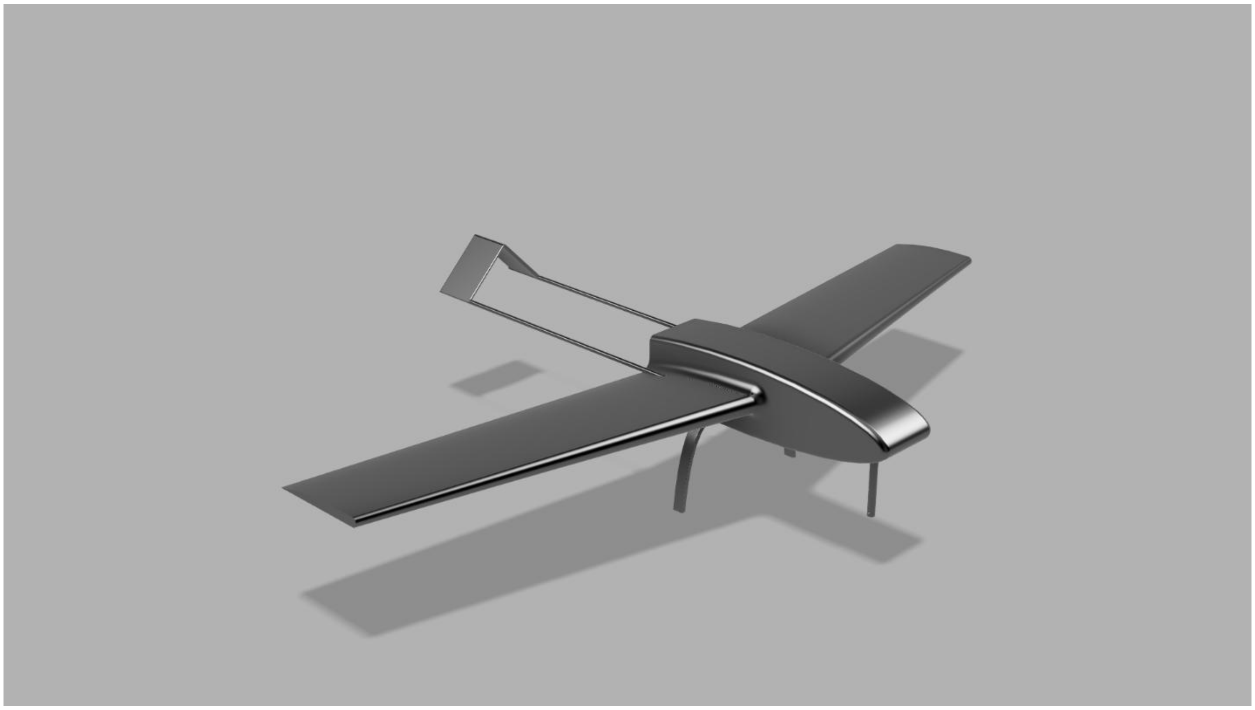

Figure 2. Early-Stage CAD Design

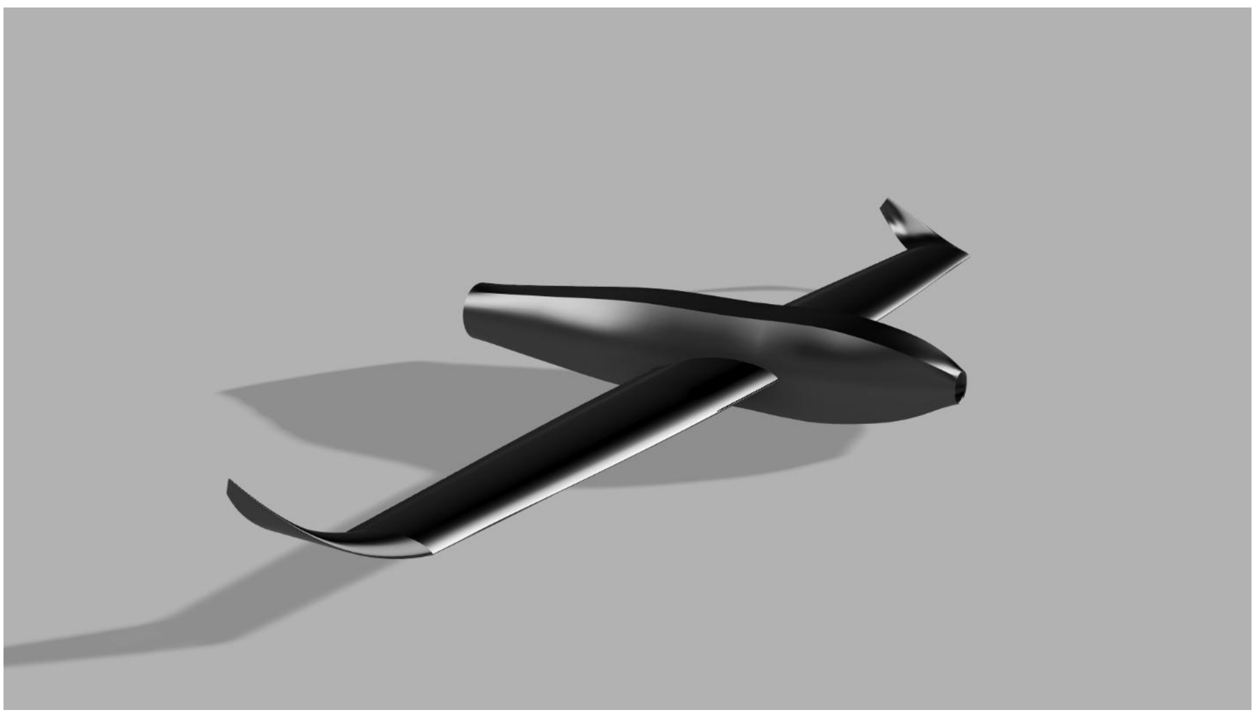

Figure 3. Updated CAD Design

3.2.1 Overview

The second conceptual design is a high efficiency, long endurance UAV configured for operation at 30,000 ft. The concept uses blended fuselage-wing geometry to reduce interference drag and improve aerodynamics during cruise. A high aspect ratio wing with moderate sweep and integrated winglets improves lift to drag ratio.

3.2.2 Geometric Characteristics and Layout

The aircraft uses a turbo prop mounted between the tail booms in a pusher configuration. This configuration minimizes aerodynamic interference with wings, allowing for cleaner airflow over the lifting surfaces. The turbo prop was selected due to its fuel efficiency, which aligns with the endurance focused mission profile. Having the propulsion system at the rear of the aircraft also allows for alternate payload configurations and integration. An inverted V-tail configuration was selected to achieve both longitudinal and directional stability while reducing the wetted area and weight. By combining the functions of the vertical and horizontal stabilizer, the design moves these control surfaces out of propeller slip streams, improves control, and reduces structural stress from prop wash. The fuselage and any structural components are designed to be fabricated from carbon fiber composites, allowing for more compact structures while maintaining proper structural integrity. The concept originally used a NACA 2412, but the updated version uses a modified NACA 2412 optimized for endurance, altitude, velocity, and temperatures.

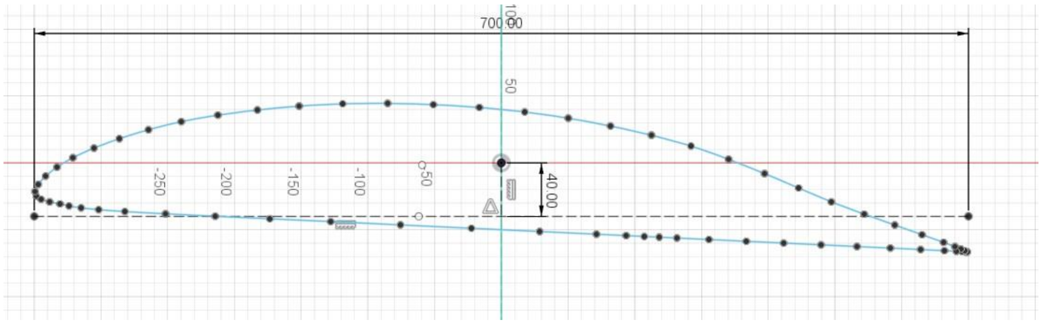

Figure 4. Updated profile of the wing

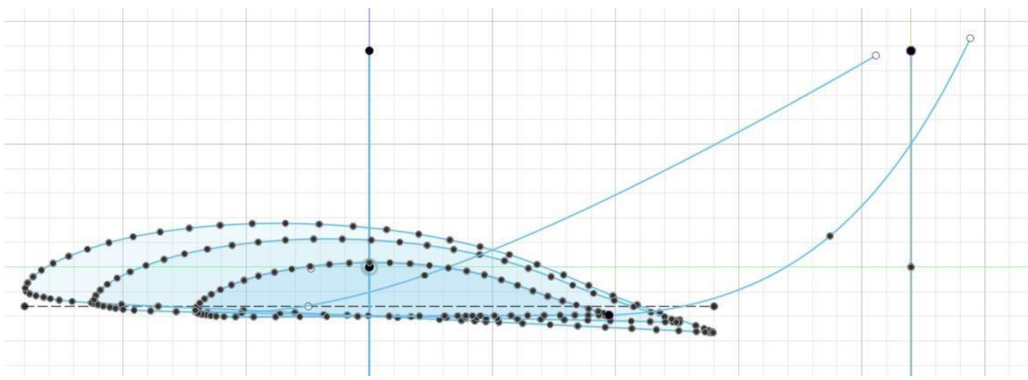

Figure 5. Wing Design

The updated wing features 6.89 ft cord length, which tapers down to around 3.42 ft at the wing tip. This taper achieves an elliptical lift distribution which reduces induced drag and minimizes structural weight at the wing tip. The profile at the end of the wing is also rotated about 2 degrees counterclockwise to locally reduce the angle of attack. This is important because it causes the wing to stall at the root first, allowing small to be more controllable and safer. This design also features

2 ft tall winglets to recover some vortex energy, reduce induced drag, and improve lift to drag ratio.

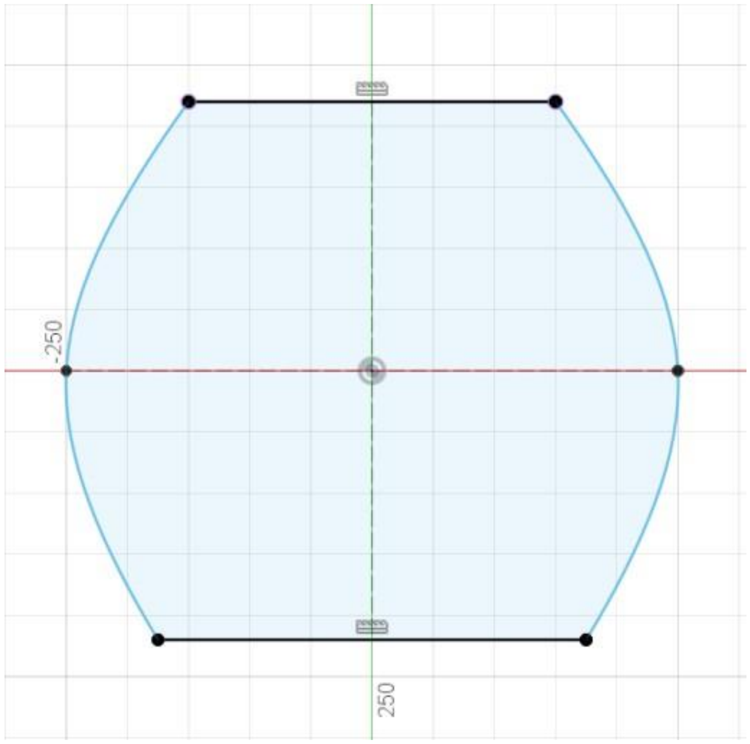

Figure 6. Fuselage Profile

Table 5: Design 2 Geometric Characteristics

Parameter	Value
Wingspan	54 ft
Length	27 ft
Fuselage Max Width	4.5 ft
Aspect Ratio	24.3
Wing Mean Chord Length	5.5 ft
Wing Root Chord	6.89 ft
Wing Tip Chord	3.42 ft
Wing Area	120.0 sq ft
Maximum Takeoff Weight (MTOW)	4000 lb
Empty Weight	1500 lb
Fuel Capacity	1500 lb
Payload (EO/IR)	1000 lb

3.2.3 Weight Breakdowns

Table 6: Design 2 Mission Segment and Weight Fraction Breakdown

Segment	Altitude (ft)	TAS (kt)	Shaft Power (hp)	BSFC	Time (hr)	End Weight (lb)
Takeoff	0–8,000	–	1300	0.50	0.25	4838
Cruise	35,000–40,000	240	750	0.50	2.00	4088
Loiter	30,000–40,000	180	500	0.50	1.00	3838
Descend	15,000–25,000	240	750	0.50	1.50	3275
Landing	25,000–0	–	300	0.50	0.20	3245

3.2.4 Aerodynamic Characteristics

Table 7: Design 2 Aerodynamic Characteristics

Parameter	Value
L/D	18
Drag Coefficient	0.028
Lift Coefficient	0.5
Endurance	11.0 hr
Range	1100 nmi
Airfoil Selection	Modified NACA 2412

The initial aerodynamic and performance values were revised to ensure physical realism and internal consistency for a 5,000lb turboprop ISR aircraft. The original L/D, drag coefficient, lift coefficient, and endurance values were overly optimistic and more representative of a high performance sailplane configuration. Updated values were selected based on typical turboprop performance ranges and conceptual design methodology to maintain consistency with fuel fraction, wing loading, and propulsion assumptions.

3.2.5 Propulsion Characteristics

This design uses a Pratt & Whitney PT6A-67 class engine. This engine is a high-power turboprop, widely known for its reliability and high power-to-weight ratio. Engines in the –67 class typically produce around 1,200 to 1,700 shaft horsepower depending on configuration [24]. This model is configured with two spools, a gas generator section, and an independent power turbine driving the propeller through a reduction gearbox. This engine is optimized for rapid throttle response, efficient power transfer to the prop, and simple engine starting. This engine class is considered a TRL 9 due to its fully certified, flight proven performance.

3.2.6 Subsystems

Hydraulic System

The aircraft uses a central hydraulic system to power primary flight control surfaces and landing gear actuation. Due to the aircraft's size and cruise speed, aerodynamic hinge moments exceed the limits of an electromechanically operated system, making hydraulics the best solution. The hydraulic system will be driven via an accessory gearbox on the turbo prop, which sends pressurized fluid to the distribution manifold. In addition, an electric pump was implemented as a redundancy in the event of engine failure. This configuration provides high force capability, reliability, and proven performance on similarly sized aircraft, giving it a high technical readiness score of 9.

Flight Control System

This aircraft uses a fully integrated avionics suite designed for autonomous long endurance UAV operation. The system includes redundant flight control computers, an integrated GPS navigation system, air data sensors, engine health monitoring, and digital flight monitoring. Mission parameters such as waypoints, loiter patterns, and altitude constraints are uploaded to the system preflight. In flight, the system automatically trims, and monitors faults ensuring stable operation. Communication between the aircraft and ground control is maintained through an encrypted line of sight data link or satellite for out-of-sight missions. The system is capable of fully autonomous flights, or flights with real time operation from the ground. In the event of any communication failures, the UAV uses an auto return to base system to safely return and land at its original location. The avionics and autonomous mission management technologies are mature and have been demonstrated on other UAVs such as the MQ-9 Reaper giving it a TRL of 8-9.

3.2.7 Cost

The projected post of this aircraft is driven by the composite airframe, propulsion system, avionics suit, and hydraulics. Designing the main structures from carbon fiber increases material and tooling costs compared to traditional aluminum. The Pratt & Whitney PT6A-67 propulsion system is one of the costliest elements of the design usually costing somewhere in the low seven figures. Including avionics, hydraulics, and ground control infrastructure, a preliminary cost estimate for this private jet sized composite UAV is $6-10 million USD per unit.

3.3 Conceptual Design 3

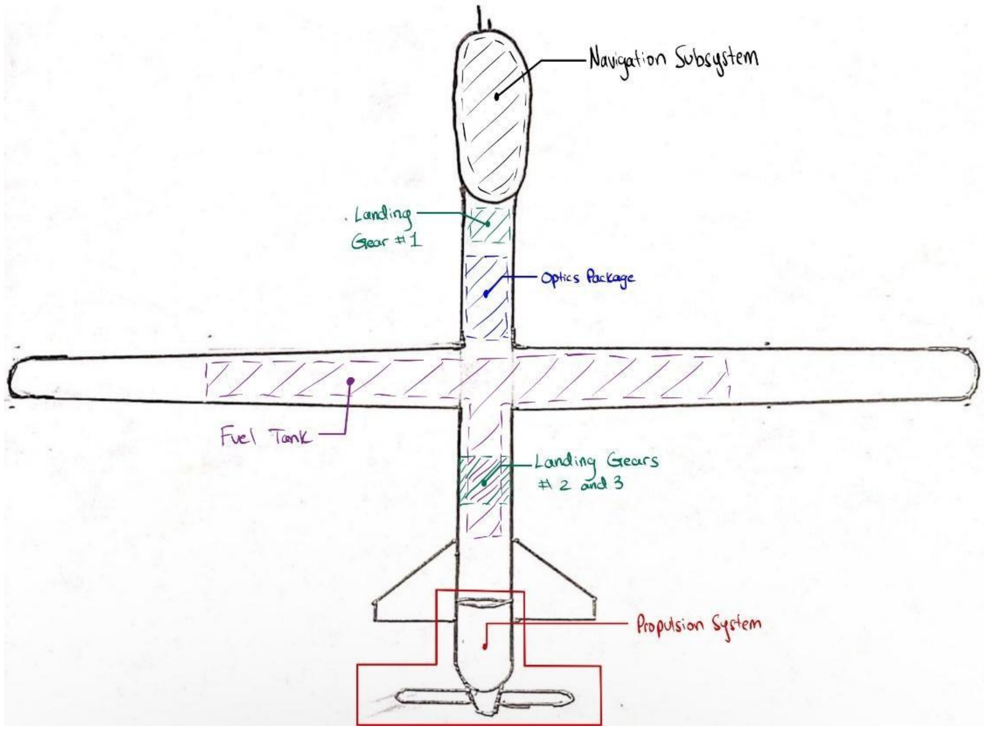

Figure 7. Top View of Conceptual Design 3

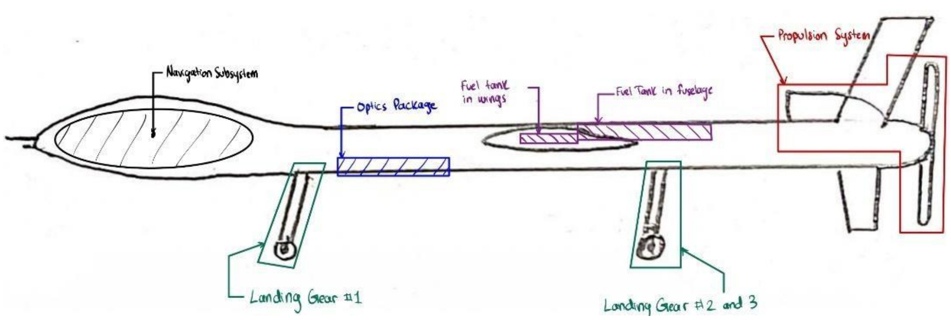

Figure 8. Side View of Conceptual Sketch 3

3.3.1 Overview

Conceptual sketch 3 was influenced by the MQ-9 Reaper. This design is a medium altitude, long endurance (MALE) turboprop UAV optimized for the design requirements [7] specified by Siemens. Conceptual sketch 3 illustrates a high-aspect ratio wing, an efficient propulsion system, and fully integrated subsystems, all designed to maximize mission effectiveness while optimizing overall aerodynamic and operational efficiency.

3.3.2 Geometric Characteristics and Layout

The navigation subsystem is featured in the nose of the plane. The navigation subsystem is located in the nose of the UAV. The navigation system makes the nose bulkier but is a crucial part of the UAV. The landing gear is located right behind the navigation system. Since it only makes sense for the landing gear to be on the belly or underside of the fuselage and for the optics package to also be on the underside of the fuselage as per the Siemens requirements [7], it would be in the best interests for the landing gear to be able to retracted so that it does not interfere with the optics package field of view (FOV). This could make the fuselage larger than calculated to be, which will increase drag but it is important the FOV of the optics package isn't interfered with. The UAV has high-aspect ratio wings that have fuel tanks in the wings and fuselage. The fuel tank of the fuselage will be located above landing gears 2 and 3, so that there isn't any interference between the two. Also, with the fuel tank in the fuselage being closer to the upper surface of the fuselage, this allows for aerial refueling during flight. Lastly, the propulsion system is located at the very end of the fuselage. The propulsion system features a turboprop engine. Reason for the turboprop is because it is the most efficient engine for the specified orbit flight in the mission profile of the UAV.

Table 8: Conceptual Sketch 3 Geometric Sizing

Parameter	Value
Wingspan	57 ft
Length	35 ft
Fuselage Diameter	3.8 ft
Aspect Ratio	13
Wing Mean Chord Length	4.38 ft
Wing Root Chord	5.85 ft
Wing Tip Chord	2.92 ft
Wing Area	249.92 sq ft
Maximum takeoff weight (MTOW)	5,560 lb
Empty Weight	2,860 lb
Fuel Capacity	2,000 lb
Payload (EO/IR)	700 lb

Table 8. shows the calculated geometric sizing of conceptual sketch 3. There can be further modifications to the sizing because of the interference that was talked about earlier between the landing gears and optical package that are both on the belly of the plane.

3.3.3 Weight Breakdown

Table 9: Conceptual Sketch #3 Weight Breakdown Throughout the Mission Profile

Segment	Altitude (ft)	TAS (kt)	Shaft Power (shp)	BSFC (lb/(hp*hr))	Time (hr)	End Weight (lb)
Takeoff	0 – 5,000	140	900	0.534	0.15	5,488
Climb	5,000 – 35,000	160	800	0.534	1.20	4,975
Cruise	39,000 – 41,000	210	450	0.534	8.00	3,055
Loiter	30,000 – 40,000	165	300	0.534	10.00	1,453
Descend	10,000 – 25,000	190	180	0.534	0.75	1,381
Landing	0 – 2,000	120	150	0.534	0.20	1,365

The weight breakdown was based of a typical mission profile of a UAV, there is the takeoff, climb, cruise, loiter descend and landing. The Honeywell TPE331-10 [27] turboprop engine was chosen for this design. It features BSFC of 0.534 lb./(hp*hr.). The weight decreases progressively through each segment, ending the mission at roughly 3,950 lb. This confirms that the mission is feasible within the available fuel load. The time estimations of takeoff, climb, cruise, descend and landing are estimations of what a mission profile could look for the UAV. The equations used to calculate and estimate the weight breakdown of the UAV were pulled from the course textbook [2].

3.3.4 Aerodynamic Characteristics

Table 10: Conceptual Sketch #3 Aerodynamic Characteristics

Parameter	Value
Maximum L/D	39
Maximum Lift Coefficient, $C_{L,max}$	1.85
Minimum Drag Coefficient, $C_{D,min}$	0.009
Pitching Moment Coefficient at Zero, C_{m0}	-0.38
Stall Behavior	Gradual
Wing Shape / Planform	Elliptical
Airfoil Selection	NACA 6412

The NACA 6412 was picked out of the airfoil library that was available on airfoil tools [29]. Then on XFLR5 [28] a plane wing was created, and a batch analysis was used at different altitudes and Reynolds numbers that the UAV could experience. Some of the graphs that the data was pulled from can be seen below.

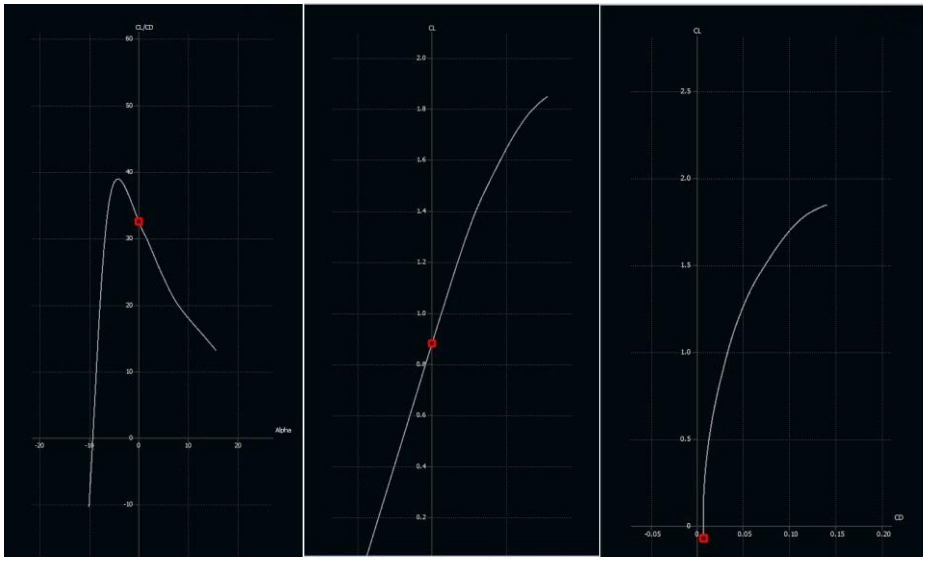

Figure 9. XFLR5 Plots

3.3.5 Propulsion System

The Honeywell TPE331-10 was selected because it provides an optimal balance of power, efficiency for medium-altitude long endurance (MALE) and high-altitude long endurance (HALE). The engine provides 940 Shaft horsepower (shp). This provides a strong climb capability and reliable cruise performance up to the 40,000 ft class while maintaining competitive specific fuel consumption (0.534 lb./shp·hr). Its proven operational history on long-endurance surveillance platforms demonstrates durability and fuel efficiency at loiter power settings, which directly supports the mission requirement for extended endurance. The main reason why the turboprop was picked over the turbofan is that the engine is more provides higher endurance, which is more suitable for the aircraft's weight and mission profile. A turbofan would offer higher top speed but at the cost of increased fuel consumption and reduced endurance, which is unnecessary for surveillance-focused missions.

3.3.6 Subsystems

Just outside the nose of the UAV is the angle of attack sensor, which is how the drone understands airflow and stability. Inside the nose of the UAV there are the GPS modules and batteries. These a responsible for powering and guiding the aircraft. The LYNX SAR radar [30], which is commonly used in the MQ-9 reaper is the UAV's high-powered radar to create an image of what is flying below even in undesirable weather. The bulk of the nose is taken up by SATCOM satellite dish, which is responsible for keeping the UAV connect beyond the operator's line of site. This would mean that a satellite would be used to send the signal back and forth. A series of hydraulic actuators and motors would be responsible for controlling the control surfaces on the horizontal and vertical stabilizers. The land gear would also be controlled by hydraulics to be able to fully conceal the landing gear after takeoff. All the technology that has been stated is at technical readiness level 9.

The technology that is used on conceptual sketch 3 was referenced from the MQ-9 Reaper [31].

3.3.7 Cost

Detailed cost data for individual UAV subsystems and military-grade components are generally not released to the public, making precise cost modeling difficult at the conceptual design stage.

To generate a first-order estimate, cost scaling relationships published in the *DoD Unmanned Aircraft Systems Roadmap* were applied. That source suggests approximate cost factors of $1,500 per pound of empty weight and $8,000 per pound of payload capacity for representative Department of Defense unmanned platforms [3]. As well as the increase in cost for manufacturing more complex shapes, such as the elliptical wing, the cost of conceptual sketch three is around $11 million USD.

3.4 Conceptual Design 4

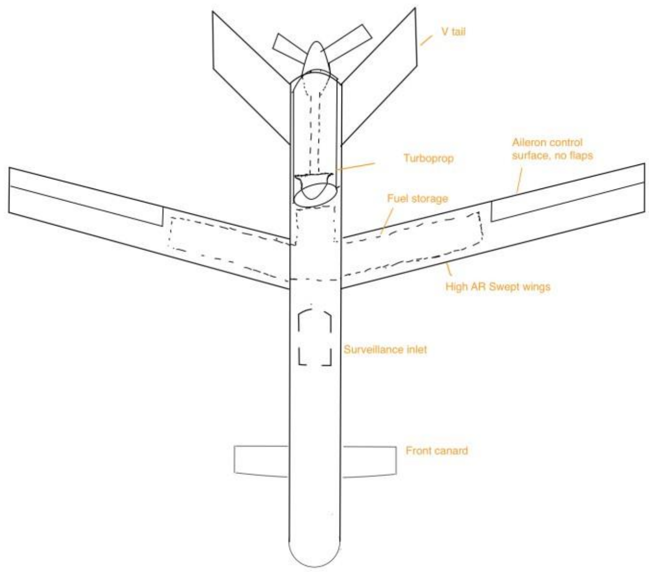

Figure 10. Design 4 Top View

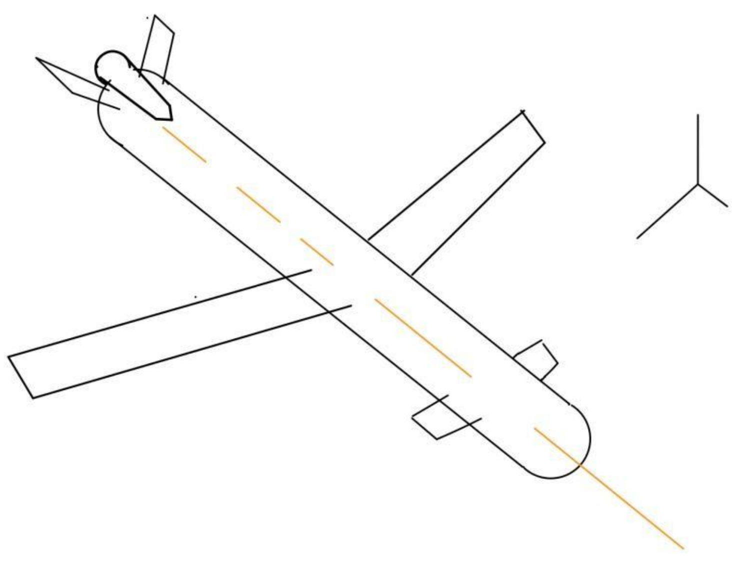

Figure 11. Design 4 Isometric View

3.4.1 Overview

The fourth conceptual design is a long-distance UAV, capable of high speeds at the sacrifice of service ceiling. This design was originally inspired by the Piaggio P.180 due to its high endurance for a private jet along with high speed [5]. Compared to UAVs, jets face greater limitations due to their necessity for human capacity. Due to this lesser constraint a few design elements were altered to decrease weight in hopes of increasing efficiency over the flight duration. Key changes include the removal of twin turboprop engines running along the wings of the aircraft and replacing them with a single turboprop engine at the rear of the aircraft. Additionally, to prevent any interference from the tail control surfaces and the propulsion system, a V tail is used [38].

3.4.2 Geometric Characteristics and Layout

The aerodynamic and structural configuration of the aircraft was derived through a comprehensive multi-variable trade study. The resulting design features a high-aspect-ratio (AR) swept wing integrated with a canard-foreplane and V-tail empennage for optimized longitudinal and directional stability. The primary ISR payload is housed within a ventral fuselage cavity, with the sensor gimbal's longitudinal station situated at approximately the fuselage midsection. To maximize volumetric efficiency, the wing box and the interconnected fuselage carry-through structure are utilized for integrated fuel storage. The propulsion system, a Pratt & Whitney turboprop, is installed in a pusher configuration at the fuselage aft, situated between the V-tail surfaces to minimize interference drag and optimize propulsive efficiency.

3.4.3 Weight Breakdown

Table 11: Design 4 Weight Overview for Flight Duration

Segment	Power (hp)	BSFC	Fuel (lb)	W_{start}	W_{end}
Takeoff	–	–	150.0	5870.0	5720.0
Transit to orbit	98	0.525	131.0	5720.0	5589.0
Orbit loiter (10 hr)	88.5	0.450	682.0	5589.0	4907.0
Transit return	91.9	0.525	117.0	4907.0	4760.0
Landing	–	–	20.0	4760.0	4740.0
		Total fuel used:	**1100.0 lb**	**Fuel remaining:**	**1000.0 lb**

This design is heavier than others, this makes it have a higher fuel consumption. Due to this, specific infrastructure within the design is used to increase the fuel capacity within the aircraft. The aircraft can store up to 2,100lbs of fuel, with 1,100lbs being consumed in a standard flight.

Table 12: Design 4 Geometric Characteristics

Parameter	Value
Wingspan	58.1 ft
Length	47.4 ft
Fuselage Max Width	4 ft
Aspect Ratio	15
Wing Mean Chord Length	3.87 ft
Wing Root Chord	8 ft
Wing Tip Chord	3.1 ft
Wing Area, S	225.04 ft^2
Maximum Takeoff Weight (MTOW)	5,870 lb
Empty Weight	3,760 lb
Fuel Capacity	2,100 lb
Payload (EO/IR)	1,000 lb

3.4.4 Aerodynamic Characteristics

Table 13: Design 4 Aerodynamic Coefficients

Coefficient	Value
Lift coefficient, C_L	0.450
Drag coefficient, C_D	0.031
Lift-to-drag ratio, L/D	14.50
Zero-lift drag coefficient, C_{D0}	0.022
Efficiency Factor, e	0.82
Induced drag factor, k	0.0355
Maximum lift coefficient, $C_{L,max}$	1.9
Pitching moment coefficient, C_M	-0.04
Propulsive efficiency, η_p	0.82

The performance metrics were derived using the Breguet Range and Endurance equations. Given the transition to a configuration reminiscent of the Piaggio P.180, the aerodynamic coefficients were balanced to a target value at 14.5 to reflect a high-speed, high-efficiency turboprop profile rather than a pure glider. The zero-lift drag coefficient $C_{D0}$was estimated at 0.022, accounting for the fuselage design and the pusher-propeller integration. Lift Coefficient was found to be a cruise C_L of 0.450 and a C_L of 1.9 were utilized. All three geometric aspects along the side of the aircraft, being the canard, aft wings and V tail to maintain low stall speeds at the 5,870lb MTOW.

3.4.5 Propulsion System Selection

The Pratt & Whitney PT6A-66X was selected as the primary powerplant because it offers a superior power-to-weight ratio and mission-critical reliability for Medium-Altitude LongEndurance (MALE) operations [39]. Delivering 850 shp, the PT6A-66X provides robust climb performance and stable high-altitude cruise capabilities in the 30,000 to 40,000 ft class [24]. One of the primary strengths of the PT6A-66X is its competitive Specific Fuel Consumption (SFC), ranging between 0.45 and 0.6lb/shp·hr, which directly enables the aircraft to utilize its 2,100lb fuel capacity for extended 10-hour station-keeping intervals. The engine's thermal efficiency at loiter power settings ensures that endurance is maximized without compromising the 1,000lb payload capacity.

3.4.6 Subsystems

The fourth design requires integrated subsystem architecture to optimize its role as a long endurance surveillance unmanned aerial vehicle. Central to the aircraft's operation is the surveillance inlet, located along the center of the aircraft within the fuselage midsection to provide a clear field of regard for the 1,000lb EO/IR payload. Aerodynamic control is managed through a three-surface configuration, featuring a front canard for longitudinal stability and high AR swept wings equipped with aileron control surfaces; Notably the aircraft’s design omits flaps to prioritize cruise efficiency. The aircraft's 2,100lb fuel storage is distributed within the wing box and fuselage carry-through structure to maximize volumetric efficiency. This entire suite is powered by a rear-mounted Pratt & Whitney PT6X turboprop in a pusher configuration, situated between the V-tail to minimize interference and ensure consistency when flying at high-altitudes.

3.4.7 Cost

Utilizing the Piaggio P.180 Avanti as a primary design referent provides am upper-bound baseline for preliminary cost estimation [5]. Given that the P.180 carries a manufacturing cost of approximately $10 million, this figure serves as a conservative fiscal ceiling. The total program expenditure for the current design is expected to be significantly lower, as the transition to a single engine unmanned platform eliminates the high costs associated with redundant twin-engine propulsion systems, pressurized cabin structures, and human-centric life support systems. The specifications provided additionally support this as the project to fall below $10 million

4.0 TRADE - OFF STUDIES

4.1 Trade Study Methodologies

To systematically evaluate and down-select design options, three primary methodologies were considered for the trade studies:

Pugh Matrix (Concept Screening): A qualitative tool that compares concepts against a baseline reference as Better (+), Worse (-), or Same (S). This is best utilized during the initial configuration phase to reduce bias and screen early concepts before detailed simulation data is available [9].

Weighted Decision Matrix (WDM): A quantitative tool where design criteria are assigned percentage weights based on their relative importance, and candidates are scored numerically. It is ideal for subsystem selection where conflicting goals must be prioritized [2].

TOPSIS: A multi-criteria analysis that ranks alternatives based on their geometric distance from both a "Positive Ideal Solution" and a "Negative Ideal Solution". This offers mathematical rigor for handling high-fidelity quantitative data during component optimization [26]

4.2 Trade Study 1: Aerodynamic Configuration

A Weighted Decision Matrix (WDM) was conducted to identify the most effective tail and fuselage configuration. The design criteria, prioritized from highest to lowest weight, were Endurance/Range, Stability/Control, Cost/Complexity, Environmental Resistance, and Surveillance Ability.

Table 14: Trade Study 1 - Aerodynamic Configuration

Criteria	Weight	Conv. Tail	T-Tail	V-Tail	Twin Fuselage: H-Tail	Inverted V-Tail	Inverted Y Tail
Range / Endurance	0.34	3.5	3	5	2.5	3	4
Stability / Control	0.26	4.5	4.5	3	4	4.5	4.5
Cost / Complexity	0.20	5	4	3.5	2.5	2.5	3
Env. Resistance	0.13	4	3	4	4.5	5	4
Surveillance Ability	0.07	2.5	3	3.5	3.5	3.5	2
Total	**1.00**	**4.055**	**3.59**	**3.945**	**3.22**	**3.585**	**3.79**

While alternative concepts like the V-Tail and Inverted Y-Tail showed strong potential for range and endurance, the conventional tail configuration ultimately achieved the highest overall score due to its balanced performance across all required design criteria.

4.3 Trade Study 2: Propulsion System

To research and evaluate the optimal engine configuration, a Multi-Weighted Matrix was utilized.

The propulsion system had to strictly meet requirements of operating on JP-8 fuel, sustaining an 8-hour endurance, and achieving a 1,125 nmi range.

Table 15: Trade Study 2 - Propulsion System

Criterion	Why it matters	Weight
1. Propulsion Performance (Subtotal: 0.45)		
Endurance / Fuel Efficiency	Drives time on station	0.18
Altitude Performance	ISR often needs high altitude	0.10
Power-to-Weight (Installed)	Payload + climb margin	0.07
Loiter Efficiency	Most time spent here at cruise power	0.06
Part-load Efficiency	Real missions do not sit at maximum power	0.04
2. Mission & Signature Requirements (Subtotal: 0.20)		
Vibration Impact on Optics	Image quality / stabilization	0.08
Thermal Signature (IR)	Survivability / detectability	0.05
Acoustic Signature	Community ops / tactically relevant	0.04
Electrical Power Availability	Suitcase optics + compute draw	0.03
3. Maintenance & Reliability (Subtotal: 0.25)		
Reliability / TBO / Durability	Fleet readiness on JP-8 fuel	0.10
Maintenance Complexity	Field serviceability and turnaround time	0.06
Fuel System Robustness	Tolerance for real-world fuel contamination	0.05
Weather Operability	performance in cold/hot environments	0.04
4. Programmatic & Risk (Subtotal: 0.10)		
TRL / Maturity	Risk reduction on JP-8	0.04
Integration Complexity	Impacts schedule (cooling, packaging)	0.03
Cost	Acquisition + operating program feasibility	0.03
TOTAL SCORE		**1.00**

The candidates, Turbojet, Turbofan, Turboprop, and Turboshaft were evaluated across four submatrices: Mission Performance (45%), Payload and Sensing Compatibility (20%), Operability and Sustainment (25%), and Programmatic and Integration Risk (10%). The

Turboprop emerged as the definitive winner, heavily favored for its endurance, part-load efficiency, and maturity on JP-8 fuel.

4.4 Trade Study 3: Wing Shape / Platform

A weighted decision matrix was performed to identify the most effective wing platform configuration. Conventional aft-swept layouts performed adequately but demonstrated compromises in aerodynamic efficiency and payload field-of-view integration. The canard and aftswept configuration successfully mitigated these tradeoffs, achieving the highest overall score and securing its place as the final design choice.

Table 16: Trade Study 3 - Wing Shape

Criteria	Weight	Twin-Fuselage	Forward-Swept	Aft-Swept (Conv.)	Canard + Aft-Swept (Final)
Aerodynamic Efficiency (L/D)	35%	2	4	3	5
Structural Weight	25%	1	2	4	5
Stability & Control	20%	5	2	5	3
Payload Integration (FOV)	20%	5	3	3	4
Total Weighted Score	**100%**	**2.95**	**2.90**	**3.65**	**4.40**

4.5 Trade Study 4: Material Selection

The final trade study also utilized a weighted decision matrix to compare structural materials against the environmental and operational demands of the project. Based on client requirements, the candidates were Aluminum (2024/7075), Carbon Fiber (Graphite-Epoxy), and Titanium (Ti6Al-4V).

Table 17: Trade Study 4 - Material Selection

Criteria	Weight	Aluminum (2024/7075)	Carbon Fiber (Graphite-Epoxy)	Titanium (Ti-6Al-4V)
Environmental Resistance (Salt/Fog)	30%	2	5	5
Structural Weight (Impact on Fuel Burn)	25%	3	5	3
Cost (Material & Processing)	25%	5	2	1
Manufacturability (Production Complexity)	20%	4	3	1
Total Score	**100%**	**3.4**	**3.85**	**2.7**
Rank		**2nd**	**1st (Winner)**	**3rd**

Carbon Fiber (Graphite-Epoxy) was selected as the optimal material, significantly outperforming Aluminum and Titanium in structural weight benefits and environmental resistance (specifically against salt/fog corrosion).

CHAPTER II – INTERIM DEISGN REPORT

1.0 Design & Regulatory Requirements

1.1 Design Requirements

The following requirements define the performance, mission, and operational characteristics of the Angel One Intelligence, Surveillance, and Reconnaissance (ISR) UAV System [7].

Range

- The AO ISR System shall meet a minimum total mission range of 750 miles, including outbound travel, ISR orbit time, and return.
- The aircraft must also meet a baseline system range of 1,125 nmi under standard cruise conditions.

Payload

- Payload consists of the EO/IR sensor package approximately the size of a suitcase along with required mission avionics.
- The electrical system must supply 12 VDC for 8 hours to support the payload and flight controls.

Takeoff & Landing Distances

- Takeoff distance: ≤ 2,345 ft
- Landing distance: ≤ 2,250 ft
- Must operate from runways ≥ 5,000 ft in length at elevations ≤ 6,000 ft MSL and temperatures ≤ 100°F.

Maximum Takeoff Weight (MTOW)

- MTOW shall support the complete mission (fuel, payload, and margins) while remaining within stated performance capabilities.

Cruise Speed

- Maximum cruise speed: 370 kn
- Never-exceed speed: 285 kn IAS, Mmo 0.64M

Climb Speed / Rate of Climb

- Rate of climb: 3,424 ft/min
- System must reach an operational altitude of 30,000 ft MSL prior to entering orbit.

Operational Ceiling

- The aircraft shall have a service ceiling of 41,001 ft.

Table 18: Siemens Performance and Design Requirements

Requirement	Satisfying System / Target	Current Design Performance
Min. Total Range	750 miles (Outbound, Orbit, Return)	8,977.77 miles
System Range	1,125 nmi (Standard Cruise)	7,801.46 nmi
Payload Capacity	EO/IR sensor package (Suitcase size)	1,000 lbs (Lynx Multi-Mode Radar)
Electrical Power	12 VDC for 8 hours	Tattu 6S 16000mAh LiPo Battery
Takeoff Distance	$\leq$ 2,345 ft	2,000 ft
Landing Distance	$\leq$ 2,250 ft	2,250 ft
MTOW	Support fuel, payload, and margins	3,203.75 lb
Max. Cruise Speed	370 knots	301.1 knots
Never-Exceed Speed	285 kn IAS / Mach 0.64	466 knots
Rate of Climb	3,424 ft/min	2,537.7 ft/min
Op. Altitude	30,000 ft MSL (Pre-orbit)	Satisfied
Service Ceiling	41,001 ft	45,000 ft
Runway Length	$\geq$ 5,000 ft length	2,500 ft

The figure above outlines a side-by-side comparison between the initial engineering targets established by the Siemens client, and the calculated capabilities of the Angel One baseline. Each criterion required from the client is satisfied to ensure that the UAV's structural and aerodynamic configuration remains compliant with its intended ISR mission profile. Each performance spec was calculated as listed below

- Range and Endurance: Validates that the 210-gallon JP-8 fuel capacity satisfies the 750 mile mission minimum and the 1,125 nmi baseline cruise requirement. Achieved using the Bruguet Range Formula

$$(R = \ V \cdot \left(\frac{L}{D}\right) \cdot I_{sp} \cdot \ln\left(\frac{W_i}{W_f}\right)[45] \quad (1)$$

- Payload and Power: Confirms the integration of the EO/IO sensor package. This package includes an optics system and radar. The optics system selected is the L3Harris WESCAM MX-20D, and the radar is the Lynx Multi-Mode Radar (General Atomics).

The power system selected is the Tattu 6S LiPo Battery, due to its robustness and ability to well surpass the 12VDC for 8 hours requirement.

- Takeoff and Landing: Ensures the aircraft can take off and land within the constraints of the clients desired runway length of 5000 ft. Take off and ground roll distance were calculated with the following formula:

$$\frac{W}{g}\frac{dV}{dT} = T - D - \mu(W - L)[45] \tag{1}$$

- Flight Envelope: Tracks the critical speed and altitude requirements for the aircraft during flight. This includes the service ceiling, operational altitude, and Rate of Climb (Calculated by the equation:

$$RC = \frac{V(T-D)}{W})[50.] \tag{2}$$

- Safety Limits: Monitors the 285 kn IAS / Mach 0.64 Never-Exceed speed to ensure structural integrity is maintained over the entire flight envelope.

1.2 Applicable Regulatory and Certification Standards

To comply with the widest range of possible regulatory standards, the Angel One UAV will be preliminarily designed to comply with multiple aviation regulatory frameworks, including those outlined by Siemens, civil aviation regulations, military standards, and industry certification guidelines.

1.21 Federal Aviation Administration (FAA)

For aircraft operating in United States airspace, several FAA regulations are relevant

- 14 CFR Part 23 establishes airworthiness standards for normal category aircraft, including requirements related to structural loads, flight performance, stability, and control. For example, the ultimate loads, which are equal to the limit loads multiplied by a 1.5 factor of safety, must be specified [33]. This requirement is still being worked towards, with wing loading data provided by FlightStream, a finite element model will be developed for the final report.
- 14 CFR Part 25 defines certification standards for transport category aircraft and includes detailed requirements regarding structural integrity, system reliability, and operational safety. For example, A 90-degree cross component of wind velocity, demonstrated to be safe for takeoff and landing, must be established for dry runways and must be at least 20 knots or 0.2 V_{SR0}, whichever is greater, except that it need not exceed 25 knots [34]. This requirement is also still being worked towards. Preliminary plans involved using FlightStream to simulate the final design at a side slip angle angles corresponding to cross components of wind velocity.

Operational regulations may also apply depending on the mission scenario. 14 CFR Part 91 provides general operating rules for aircraft operations within civil airspace [35], while 14 CFR Part 107 [8] defines regulations governing small, unmanned aircraft systems and may influence certain mission operations. While this small, unmanned category is likely less applicable for our larger UAV, it is still worth noting in the case of future design changes.

1.22 European Aviation Safety Agency (EASA)

- For potential international certification or operations in European airspace, guidance may also be derived from the EASA Certification Specifications for CS-23 and CS-25 aircraft [36]. These regulations largely mirror FAA standards and define performance, structural, and operational safety requirements. These regulations standardize metrics for takeoff, landing, and structural loading. Landing performance is defined from 50ft above to a full stop, and operational landing distance typically requires a safety margin of about 1.68 times the demonstrated landing distance to ensure runway availability. Structural sizing is guided by maneuver load factors of around +3.8g and –1.5g for normal category aircraft. Certification performance requirements also include minimum climb gradients of around 2.4% to ensure clearance during takeoff [36], [37].
- EASA also provides Special Condition Light UAS (SC-LUAS) regulations for unmanned aircraft systems; however, these are primarily intended for smaller platforms and may be less applicable for the larger UAV considered here. Aircraft of this class are generally expected to achieve safety levels comparable to manned aircraft including catastrophic

failure probabilities on the order of 10^{-9} failures per flight hour. For UAVs in the business, jet size cruise altitudes fall within the range of 25,000-50,000 ft [37].

1.23 Military Standards

Because the UAV is expected to support ISR missions, military certification and operational standards are also relevant, imposing specific structural and environmental thresholds:

- MIL-STD-1797: Provides guidelines for aircraft flying qualities and stability characteristics. To satisfy these control requirements, structural sizing is guided by maneuver load factors of around +3.8g and -1.5g. [38]
- MIL-STD-810: Outlines environmental testing procedures covering temperature, humidity, vibration, and other operational stresses [29], [39]. Under this standard, the aircraft systems must safely withstand:
    - Temperature extremes ranging from -60°F to 140°F.
    - A 200-cycle salt/fog corrosion exposure requirement.
    - Exposure to corrosive and harsh chemicals, including JP-8 fuel, hydraulic fluid, oxidizers, refrigerants, and hot gases.
    - Environmental hazards including lightning strikes, ice, sand, and dust exposure.
- MIL-HDBK-516C: Defines airworthiness certification criteria applicable to both manned and unmanned military aircraft. This ensures system safety and reliability during ISR missions over populated areas and environmentally sensitive regions [40].

1.24 NATO Standards

In addition, NATO interoperability and airworthiness standards may influence system architecture:

- STANAG 4671 [30] establishes airworthiness requirements for unmanned aircraft systems from weights of 150kg to 20,000kg [41]. The UAV falls into a Class 1 specification, requiring rigorous safety procedures during each phase of flight. This document segments failures into four different types, each with their own probabilities and classes. These failure conditions and probabilities are as follows:
    - Catastrophic failures shall occur $\leq 10^{-6}$ per flight hour
    - Hazardous failures shall occur $\leq 10^{-5}$ per flight hour
    - Major failures shall occur $\leq 10^{-4}$ per flight hour
    - Minor failures shall occur $\leq 10^{-3}$ per flight hour

  To achieve these thresholds, the aircraft must limit load maneuvering, getting a load factor less than 3.8. In a single engine UAV, the engine must rotate no less than the stalling speed during take-off configuration and have a landing gear designed for a limiting descent velocity of $4.4\left(\frac{W}{S}\right)^{\frac{1}{6}}$. Additionally, this document outlines the ground control requirements for the aircraft. This system shall consist of the following: a command-and-control data link, a communication system, UAV control station, and additional ancillary elements.
- STANAG 4586 defines standardized communication and control interfaces for UAV ground control systems, enabling interoperability with NATO ISR networks [42]. The

specification classifies levels of interoperability into five levels. These levels of interoperability (LOI) are as follows:

  - Level 2: Direct receipt of ISR.
  - Level 3: Control and monitoring of the UAV payload.
  - Level 4: Control and monitoring of the UAV itself, excluding launch and recovery.
  - Level 5: Full control, including launch and recovery functions.

Because the UAV must respond to changing operating conditions, low-latency control is required. For the 1,000–10,000 kg class, the maximum delay from operator input to aircraft response is 200ms.

1.25 Industry Certification Standards

Commercial aerospace certification guidelines also play a critical role in avionics and equipment qualification. The following standards ensure the reliability and operational safety of onboard avionics and flight control systems.

- RTCA DO-160 [27] defines environmental testing procedures for airborne electronic equipment. The systems that are designed to meet DO-160 environmental categories are:
  - Flight computer
  - Navigation Systems (GPS / INS)
  - Sensors (IMU, pressure sensors, air data systems)
  - Power electronics
  - Optical package
  - Communication equipment

All the listed components above should be tested or designed to survive in varying temperatures, vibrations and electromagnetic conditions. For temperature and altitude tolerance, the avionics should operate across a temperature range of −55 °C ground-survival temperature, to +85 °C operating temperatures, and 55,000 ft altitude under a temperature/altitude test category [43]. This means that the designs should include thermal management, electronics rated for a wide range of temperatures and altitudes and environmental enclosure if the electronics are external. Vibration protection [43] should include vibration isolated avionics mounts, rubber dampers or shock mounts and structural mounts for electronics. These should provide protection for IMUs, flight computers, optical packages and communication equipment. Electrical protection [43] provides protection against voltage spikes, noise and electrical disturbances. The system will include voltage regulation, surge protection, power filtering and proper grounding. This will protect the avionics from generator spikes, motor/engine noise, lighting strikes and electromagnetic interferences. Environmental protection [43] will include protection from moisture, humidity, dust and water exposure that are listed in the client's requirements [7]. Sealed avionics bays, conformal coating on circuit boards and environmental enclosures are affective ways to protect the aircraft's avionics from environmental factors.

- RTCA DO-178C [28] establishes rigorous standards for airborne software certification and safety assurance. DO-178C is the classification of software based on the severity of failure conditions, which determines how rigorous the development and verification processes must be [44]. The 5 design assurance levels are:
    - Level A – Catastrophic failure condition
    - Level B – Hazardous or severe-major failure condition
    - Level C – Major failure condition
    - Level D – Minor failure condition
    - Level E – No safety effect

For higher criticality levels require more extensive verification, documentation and testing. DO-178C does not tell us which hardware to incorporate into the aircraft's design, but it defines how the aircraft's software must be developed and verified. Therefore, the UAV's systems should have reliable flight control software, verified and test software, documented software architecture, fault handling and safety logic.

Table 19: Engineering Standards and Compliance

Standard	Requirement Definition	Current Status / Value
FAA 14 CFR Part 23	Ultimate loads (Limit loads × 1.5 FS)	1.4 g < LF < -0.6
FAA 14 CFR Part 25	Crosswind $\geq$ 20 kts or $0.2V_{SR0}$	$V_{SR0} = 64.4$ kts
EASA CS-23/25	Landing dist. 1.68x; Min. climb gradient 2.4%	Landing: 3,780 ft; Gradient: 26.29%
EASA SC-LUAS	Catastrophic failure probability $\leq 10^{-9}$/hr	Composite airframe (panels/spars)
MIL-STD-1797	Maneuver load factors of +3.8g / -1.5g	Max load factor: 1.4g
MIL-STD-810	Temp range -60°F to 140°F; Salt/fog	Operable at -60°F to 140°F
STANAG 4671	Failures $\leq 10^{-6}$; Descent $V \leq 4.4(W/S)^{1/6}$	$V_y = 2.56$ m/s (< 7.3 m/s limit)
STANAG 4671	C2 link, Comm system, GCS	Honeywell H-764 ACE
STANAG 4586	Level 5 Interoperability (Full control)	Honeywell H-764 ACE
NATO Interop.	Max control delay 200ms	Honeywell H-764 ACE
RTCA DO-160	Survival -55°C to +85°C; Alt: 55,000 ft	44,100 ft Service Ceiling
RTCA DO-160	Isolated mounts, voltage reg, sealed bays	Composite airframe (panels/spars)
RTCA DO-178C	Software verified to Level A/B	Composite airframe (panels/spars)

The Engineering Standards and Compliance table establishes a comprehensive regulatory framework to ensure the Angel One system adheres to modern aviation safety and performance criteria. This matrix maps specific requirements from civil, military, and international governing bodies to the corresponding validated design values and integrated hardware solutions. Fulfillment of these criteria confirms that the aircraft is airworthy and structurally capable of executing its intended mission profile.

- **Civil Airworthiness (FAA/EASA):** Document adherence to structural safety standards, including max loading and crosswind capabilities.
    - **Ultimate Load Formula:** Ensures airframe can withstand 1.5 times the max expected operational pressure without failure. The design utilizes Carbon Fiber (Graphite-Epoxy) composites. This material was selected specifically for its high strength-to-weight ratio, allowing the airframe to meet these 5.7g requirements while minimizing weight.

- **Crosswind Component:** Aircraft must establish a safe 90-degree crosswind component for dry runways of at least 20 knots, or 20% of reference stall speed. Given a reference stall speed of 64.4 knots, the 0.2 V_{SR0} = 12.88 knots. Therefore the 20 knot standard governs the equation
- **Operational Landing Distance (EASA CS-23/25):** Requires a 1.68x safety margin over the demonstrated landing distance. For the required landing distance of less than or equal to 2,250 ft, the operational value is 3,780 ft.
- **Minimum Climb Gradient (EASA CS-23/25):** The standard requires a gradient of at least 2.4%. The current design achieves a gradient of 26.29%.

- **Military and Nato Standards:**
  - **Maneuver Load Factors (MIL-STD-1797):** Requires limits of +3.8g and -1.5g. The current maximum load factor is 1.4g.
  - **Environmental Resilience (MIL-STD-810):** The aircraft is verified to operate in temperatures from -60 to 140°F and withstand 200-cycle salt/fog exposure.
  - **Airworthiness Requirements (STANAG 4671):** Catastrophic failure probability is verified at $\leq 10^{-6}$ flight hour. The descent velocity limit Vy is calculated as 2.56 m/s, which is well below the regulatory limit of 7.3 m/s established by the formula:

$$4.4\left(\frac{W}{S}\right)^{\frac{1}{6}} \tag{3}$$

  - **Interoperability (STANAG 4586):** The system meets Level 5 Interoperability (full control, launch, and recovery) through the Honeywell H-764 ACE.
  - **Control Latency (NATO Interoperability):** For the 1,000–10,000 kg class, the maximum delay is 200ms, which is satisfied by the flight control architecture

- **Industry Certifications**
    - **Environmental Testing (DO-160):** Verified for survival from -55 to 85°C and a maximum altitude of 55,000 ft. The current service ceiling is 45,000 ft
    - **Hardware Protection (DO-160):** Protection is provided via isolated mounts, voltage regulation, and sealed bays within the carbon-fiber composite airframe
    - **Software Assurance (DO-178C):** Software is verified to Level A (Catastrophic) or Level B (Hazardous).

2.0 Technology Availability

To ensure the feasibility of the Angel One concept, all major subsystems were evaluated using Technology Readiness Levels (TRL). Technologies were selected based on demonstrated operational use, integration maturity, and alignment with mission requirements such as endurance, altitude capability, and reliability [10].

2.1 Structure

Carbon Fiber / Graphite-Epoxy Composites (TRL 9)

- Feasibility: Composite airframe structures are fully mature and widely used in modern aircraft and have been validated under cyclic loading, thermal variation, and environmental exposure conditions typical of long-endurance missions [3], [4].
- Implementation: Carbon fiber composites were selected due to their high strength-to-weight ratio and inherent corrosion resistance. This enables compliance with the 200-cycle salt/fog requirement without requiring additional protective coatings, unlike aluminum structures [4]. This reduces both structural weight and long-term maintenance requirements while improving mission endurance.

2.2 Propulsion

Small Turboprop- Honeywell TPE331-10 (TRL 9)

- Feasibility: The Honeywell TPE331-10 turboprop engine is a fully mature propulsion system capable of producing approximately 940-1000 shp and operating up to **45,000 ft,** making it suitable for high-altitude ISR missions [2]. It supports multiple aviation fuels, including JP-8, ensuring compatibility with military logistics [2].

- Implementation: The turboprop configuration provides high propulsive efficiency at low to medium subsonic speeds, which is optimal for long-endurance missions. The engine exhibits a relatively low specific fuel consumption (0.534 ESFC) and lightweight design (385 lb), improving fuel efficiency and payload capability [2]. Additionally, the engine integrates key subsystems such as fuel control, propeller pitch control, lubrication, and anti-ice systems, reducing system complexity and improving reliability [2].

GE Catalyst Turboprop (TRL 7)

- Feasibility: The GE Catalyst turboprop represents a next-generation propulsion system featuring a 16:1 pressure ratio compressor, additive manufacturing components, and integrated FADEC/propeller control. It has undergone extensive testing, including altitude testing up to 41,000 ft, demonstrating operational feasibility [1].
- Implementation: The Catalyst engine incorporates additive manufacturing, reducing part count significantly (12 components replacing hundreds), which improves reliability and reduces maintenance requirements [1]. While not yet as mature as legacy turboprops, it provides a viable future upgrade path for improved efficiency and lifecycle cost.

Table 20: Engine Weight & Cost Estimation [1], [2]

Number	Name	Price	Weight
1	Honeywell TPE331-10N	$1.5M	385 lb
2	Honeywell TPE331-10R	$1.2M	385 lb
3	Honeywell TPE331-10GT	$1.1M	385 lb
4	Honeywell TPE331-GD	$1.4M	385 lb
5	Honeywell TPE331-10T	$1.3M	385 lb
6	GE Catalyst 1300-CS1A	$1.8-2.1M	629.7 lb
7	GE Catalyst Military	$2.2M	650 lb
8	GE Catalyst 850-1000	$1.5M	610 lb
9	GE Catalyst Growth (1600)	2.4M	680 lb

In Table 3 illustrates all the different engine variants that were researched for the propulsion system. The Honeywell TPE331 series offers a relatively low weight (385 lb) across all variants, with moderate cost differences depending on configuration. In contrast, the GE Catalyst engines provide higher power potential but at the expense of increased weight and generally higher cost.

2.3 Flight Controls

Adaptive Flight Control Systems (TRL 7)

- Feasibility: Adaptive control systems have been extensively studied and validated through simulation and experimental flight testing. These systems can handle uncertainties and nonlinear dynamics present in modern UAV configurations [5], [6].
- Implementation: Adaptive control is implemented to improve robustness against disturbances such as turbulence and structural flexibility associated with composite airframes. These systems enable real-time adjustment of control laws, ensuring stable and efficient operation during long-duration missions [5].

2.4 Avionics and Engine Control (Additional Technology)

FADEC/FADEPC Systems (TRL 8-9)

- Feasibility: Full Authority Digital Engine Control (FADEC) systems are widely used in modern aircraft and have been successfully integrated into advanced turboprop systems such as the GE Catalyst [1], [9].
- Implementation: FADEC systems automate engine and propeller control, optimizing performance, fuel efficiency, and safety. This reduces pilot workload and enables

seamless integration with autonomous flight systems, which is critical for ISR UAV operations [9].

Flight computer (TRL 9)

- Feasibility: The H-764 ACE [46] is a mature flight computer system widely used in aerospace applications, providing reliable navigation and guidance capabilities.
- Implementation: This system integrates GPS/INS navigation and supports autonomous flight operations. Its proven reliability and compatibility with UAV systems make it well suited for this design.

Table 21: Flight Computer Weight & Price List [46], [47], [48], [49], [50]

Number	Name	Price	Weight
1	Honeywell H-764 ACE	$150k-200k	18.0 lb
2	Curtiss-Wright Parvus DuraCOR 8043	$25k-$35k	5.5 lb
3	Collins Aerospace Pro Line Fusion (UAV)	$120k-180k	12 lb
4	Mercury Systems Ensemble Series	$40k-$60k	8 lb
5	General Atomics Redundant FCC	Proprietary	15 lb

Table 4 shows a comparison of different flight computers based on their cost and weight. Some options, like the Curtiss-Wright Parvus DuraCOR and Mercury Systems computers, are lighter and cheaper, which helps keep the UAV weight and cost lower. On the other hand, systems like the Honeywell H-764 ACE and Collins Pro Line Fusion are more expensive and heavier, but they offer better performance and reliability.

2.5 Mission Systems (Additional Technology)

Electronic Optical Infrared Sensor – L3Harris WESCAM MX-20D (TLR 9)

- Feasibility: The MX-20D is a widely used ISR sensor system that provides high-resolution electro-optical and infrared imaging capabilities [11], [12], [14].
- Implementation: The system enables day and night ISR operations, supporting surveillance and reconnaissance mission requirements with proven performance in UAV platforms [13], [15].

Table 22: Optics Package Weight & Price List [11], [12], [13], [14], [15]

Number	Name	Price	Weight
1	L3Harris WESCAM MX-20 EO/IR system	\$1.5M - \$2.5M	90 lb - 110 lb
2	L3Harris WESCAM MX-20D	\$2M - \$3M	120 lb
3	FLIR Star SAFIRE HD	\$1M - \$2M	85 lb - 95 lb
4	WESCAM MX-15 EO/IR system	\$800k - \$1.5M	45 lb - 55 lb
5	TrakkaCam TC-300	\$500k - \$1M	35 lb - 45 lb
6	SPECTRUM 500 EO/IR payload	\$250k - \$600k	20 lb - 30 lb
7	INYYO Q355 EO/IR payload	\$150k - \$400k	15 lb - 25 lb

The table above shows several different EO/IR optical systems that are currently available on the market. The list was put together to get an idea of typical weight and cost ranges for these types of payloads. Although none of these specific systems will be used in the final design, since Siemens will provide their own optics package, this comparison helps estimate what kind of payload the UAV is expected to carry.

Radar – Lynx radar (TLR 9)

- Feasibility: The Lynx radar is an operational UAV radar system capable of ground mapping and moving target indication [21].
- Implementation: The radar provides all-weather ISR capability, significantly enhancing mission effectiveness and target detection capability.

Table 23: Radar Weight & Price List [16], [17], [18], [19], [20], [21], [22]

Number	Name	Price	Weight
1	AN/ZPY-3 MP-RTIP (Northrop Grumman)	$10 M - $20M+	$1,000 - $1,500
2	Lynx Multi-Mode Radar (General Atomics	$1M - $3M	120 lb - 200 lb
3	AESA Airborne Radars (Next-Gen UAVs)	$2M - $5M	150 lb - 400 lb
4	MURAD AESA Radar (ASELSAN)	$2M -$4M	200 - 300 lb
5	IMSAR NSP Series (NanoSAR / NSP-3)	$100k - $500k	3 - 10 lb

This figure compares several radar systems currently used on UAVs. The data provides a general understanding of the size and price.

Battery – Tattu 6S LiPo Battery (TLR 9)

- Feasibility: Lithium polymer batteries are commonly used in UAV applications due to their high energy density and reliability [23], [24], [31], [32].
- Implementation: The battery provides power for avionics and onboard electronic systems while maintaining a lightweight configuration.

Table 24: Battery Weight & Price List [23], [24], [25], [26]

Number	Name	Price	Weight
1	Tattu 6S 16000mAh LiPo Battery	$250- $400	3.5 lb - 4.0 lb
2	Turnigy Graphene LiPo Battery	$150 - $300	2 lb - 3 lb
3	DJI TB60 Intelligent Flight Battery	$600 - $900	3.0 lb
4	Concorde RG-390E Aircraft Battery	$1,200 - $2,000	23 lb - 25 lb

This figure compares several batteries that are used on UAVs and other vehicles. The data provides a general understanding of the size and price.

2.6 Integrated Propulsion Subsystems (Additional Technology)

Engine Auxiliary Systems (TRL 9)

- Feasibility: Subsystems such as fuel control, anti-ice systems, lubrication systems, and negative torque sensing are fully mature and standard in modern turboprop engines [2].
- Implementation: These systems enhance safety, reliability, and operational flexibility. For example, anti-ice capability enables operation in adverse weather, while negative torque sensing prevents propeller drag during engine failure. Their integration simplifies system architecture and reduces additional design requirements [2].

3.0 Design Iterations

3.1 Low Fidelity Models

Design iterations began with Conceptual Design 1 from our conceptual design report. This configuration was broadly inspired by the MQ-9 Reaper while differing in several respects, including overall dimensions, wing structure, and geometric arrangement. During model development and analysis, major difficulties were encountered in transferring geometry from OpenVSP into FlightStream. More specifically, the vertical tail and engine casing generated degenerate mesh faces, preventing these components from being imported and analyzed reliably. Several attempts were made to modify and repair the geometry; however, these efforts did not fully resolve the issue.

In addition, it should be noted that the propeller, engine, and landing gear were not included in any of the following design iterations. These components were excluded because their detailed modeling and preparation for simulation would require substantial additional effort beyond the goals established for the present study. Although this simplification reduces model fidelity, the simulations are still considered sufficient for capturing the primary aerodynamic behavior and comparing trends between candidate configurations during intermediate design. As such, the results should be viewed as low to medium fidelity estimates of aerodynamic performance.

3.1.1 Design Iteration 1

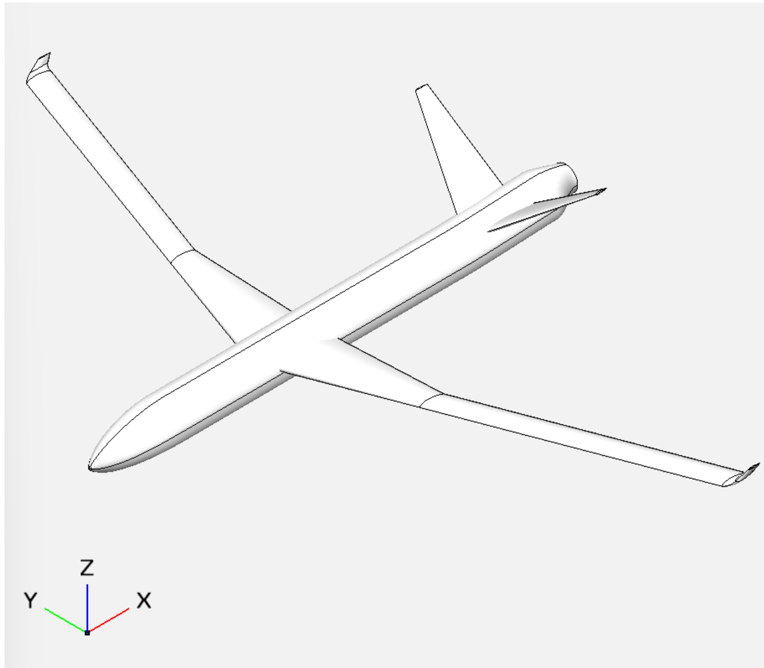

Figure 12. Design Iteration 1 Isometric View

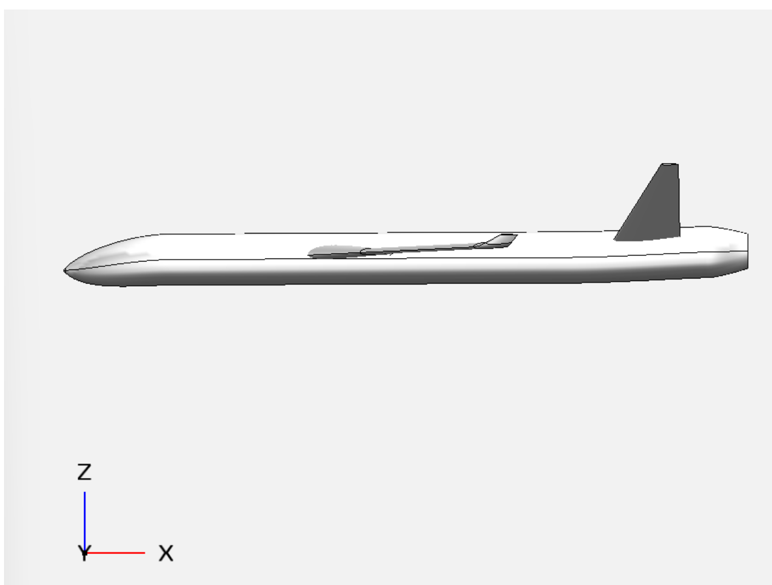

Figure 13. Design Iteration 1 Side View

Table 25: Weight & Cost Estimation 1

UNIT #	EQUIPMENT	NAME	WEIGHT [LB]	COST [$]
1	Propulsion System	Honeywell TPE331-10N	385	$1,500,000
2	Flight computer	Honeywell H-764 ACE	18	$175,000
3	Optics Package	L3Harris WESCAM MX-20D	120	$2,500,000
4	Battery	Tattu 6S 16000mAh LiPo Battery	3.75	$300
5	Radar	Lynx Multi-Mode Radar (General Atomics)	160	$2,000,000
6	Fuel Tanks	Integral wing + fuselage bladder tanks (210 gal usable)	65	$45,000
7	Fuel	JP-8 (amount = 210 gallons)	1407	$1,260
8	Structure (without the fuel, fuel tanks, landing	Carbon-fiber composite airframe with sandwich panels and spars	950	$350,000
9	Landing Gear	Fixed tricycle gear, oleo/composite/aluminum assembly	95	$30,000
	TOTAL ESTIMATED WEIGHT & COST		3203.75	$6,601,560

Table 8 shows the estimated total weight and cost for design iteration 1. The values were calculated using the data provided in Section 2 (Figures 1–4), where the cost and weight of each subsystem were summed and reported in the bottom right of the figure. Since design iterations 1, 2, and 3 use the same materials and systems, they all result in the same overall weight and cost.

As mentioned, the first design iteration was developed directly from Conceptual Design 1 presented in the previous report. All geometry for this configuration was created in OpenVSP, and all aerodynamic simulations were performed in FlightStream. All configurations were initially simulated over an angle of attack range from -10 deg to 10 deg to assess their aerodynamic behavior and longitudinal static stability. Configurations found to be longitudinally stable were subsequently evaluated for lateral directional stability through a sideslip sweep ranging from -10 deg to 10 deg. In these sideslip simulations, each configuration was analyzed at its trim angle of attack to better approximate the expected flight condition. The simulations were performed using standard sea level atmospheric properties, with an air density of $1.225\ kg/m^3$ and a freestream velocity of 51 m/s, chosen to approximate a typical loiter speed. Ideally, the density and altitude should have been adjusted to reflect the intended loiter altitude of 30,000 ft, however, this was overlooked prior to running the simulations. While this assumption affects the absolute values of aerodynamic loads and may shift the Reynolds number relative to the true operating condition, it is not expected to significantly affect the overall aerodynamic and stability trends used for comparative design evaluation. The Reynolds number associated with the simulated condition was approximately $3 \, x \, 10^6$.

The primary geometric parameters for the fuselage, wing, and tail used in this first iteration are summarized in Table 4. Note that the fuselage cross section was non-uniform and constant across all simulations. More details will be discussed on this in the detailed CAD drawings section of the report.

Table 26: Design Iteration 1 Geometric Characteristics

Parameter	Value
Wingspan, b	60 ft
Fuselage length	40 ft
Wing airfoil	NACA 4418
Wing sweep angle	19.5°
Wing dihedral angle	1°
Wing twist (root to tip)	1°
Wing z location	0.25 ft
Wing aspect ratio, AR	22.93
Wing taper ratio, λ	0.333
Wing mean aerodynamic chord, $\bar{c}$	2.77 ft
Wing root chord	6 ft
Wing tip chord	2 ft
Wing area, S_w	162.3 ft^2
Reference chord, $\bar{c}_{ref}$	2.77 ft
Wing incidence angle	0°
Wing aerodynamic center location from nose	17.77 ft
Tail configuration	V-tail
Tail airfoil	NACA 0012
Tail sweep angle	20°
Tail z location	1 ft
V-tail angle	35°
Horizontal tail root chord	4 ft
Horizontal tail tip chord	1 ft
Horizontal tail area, S_t	60 ft^2
Tail incidence angle	0°
Center of gravity location, x_{cg}	19.1 ft

An initial aerodynamic sweep was conducted over an angle of attack range from -10 deg to 10 deg. The resulting aerodynamic characteristics are shown in Figure 3, including lift coefficient, drag polar, lift to drag ratio, pitching moment coefficient, and drag component breakdown. As shown in the lift curve, the lift coefficient varies approximately linearly with angle of attack over the evaluated range, indicating predictable aerodynamic behavior and no clear evidence of stall within the simulated range. The drag polar shows the expected increase in drag with lift, while the drag breakdown indicates that parasite drag remains relatively constant and induced drag increases as the angle of attack and lift coefficient rise. In addition, the lift to drag ratio reaches a peak value of approximately 27 at an angle of attack of 6 deg, suggesting that the configuration is aerodynamically efficient in this operating region.

Despite favorable lift and drag characteristics, the configuration was found to be longitudinally unstable. This can be seen in the pitching moment coefficient versus angle of attack plot, where the slope is positive. For a longitudinally stable aircraft, the pitching moment coefficient should decrease as angle of attack increases, giving a negative slope. Instead, this configuration shows the opposite trend, meaning that as the aircraft experiences an increase in angle of attack, it generates an additional nose-up pitching moment rather than a restoring nose-down moment. As a result, the aircraft would tend to diverge from its trimmed condition instead of naturally returning to equilibrium after a disturbance.

This instability is most likely related to the center of gravity location being too far aft, rather than not aft enough. For a conventional tail-aft configuration, moving the center of gravity too far aft reduces static margin and weakens the restoring pitching moment required for longitudinal stability. In practical terms, the aircraft center of gravity was likely positioned too close to, or behind, the neutral point, causing the positive slope observed in the pitching moment curve.

Due to this first design iteration was longitudinally unstable, no further detailed analysis was performed for this configuration. Instead, subsequent design iterations focused on improving stability through geometric modifications such as shifting the center of gravity forward, increasing tail effectiveness, and adjusting the relative placement and sizing of the lifting surfaces.

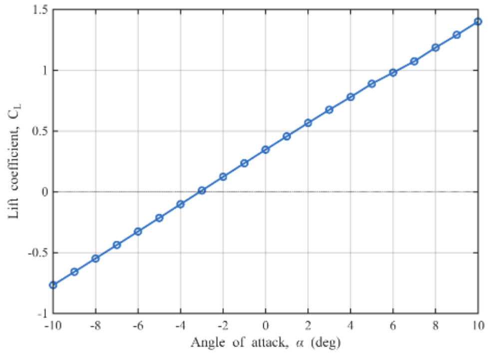

(a) Lift coefficient as a function of angle of attack.

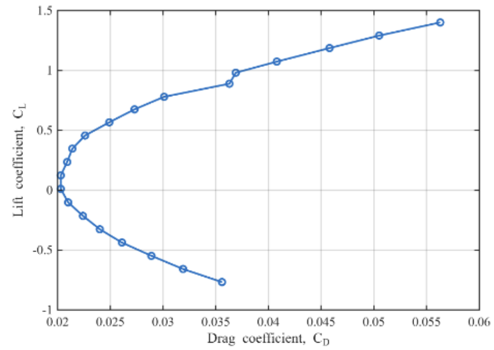

(b) Drag polar for the configuration.

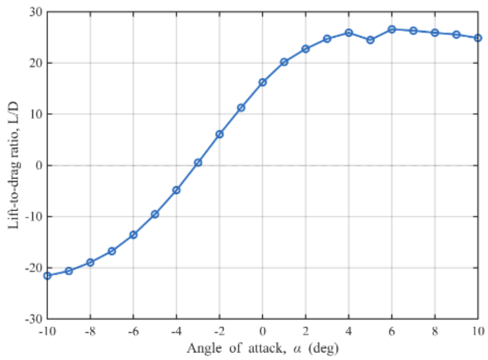

(c) Lift-to-drag ratio as a function of angle of attack.

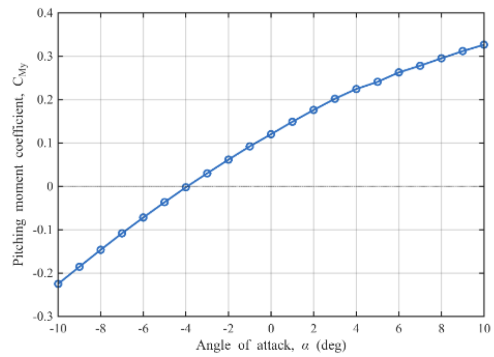

(d) Pitching moment coefficient as a function of angle of attack.

Figure 14. Design Iteration 1 Aerodynamic Performance Plots

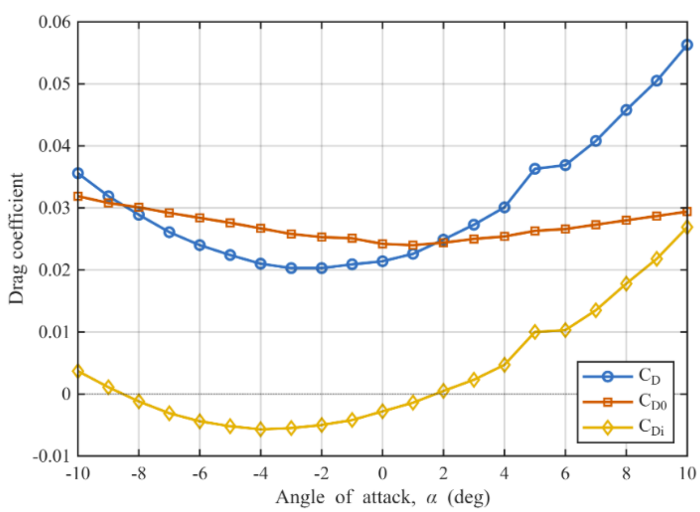

Figure 15. Design Iteration 1 Drag Breakdown

3.1.2 Design Iteration 2

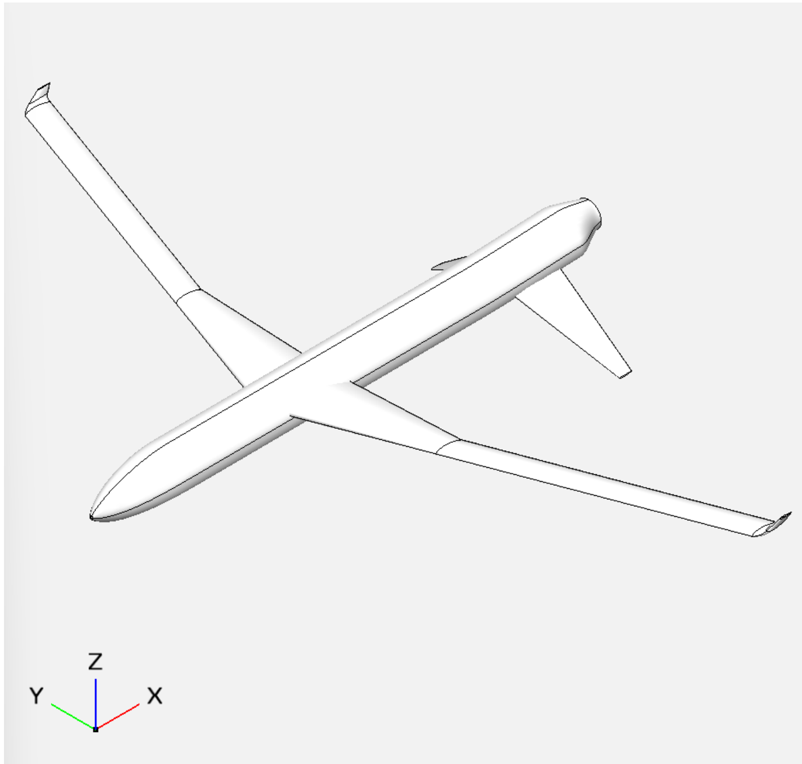

Figure 16. Design Iteration 2 Isometric View

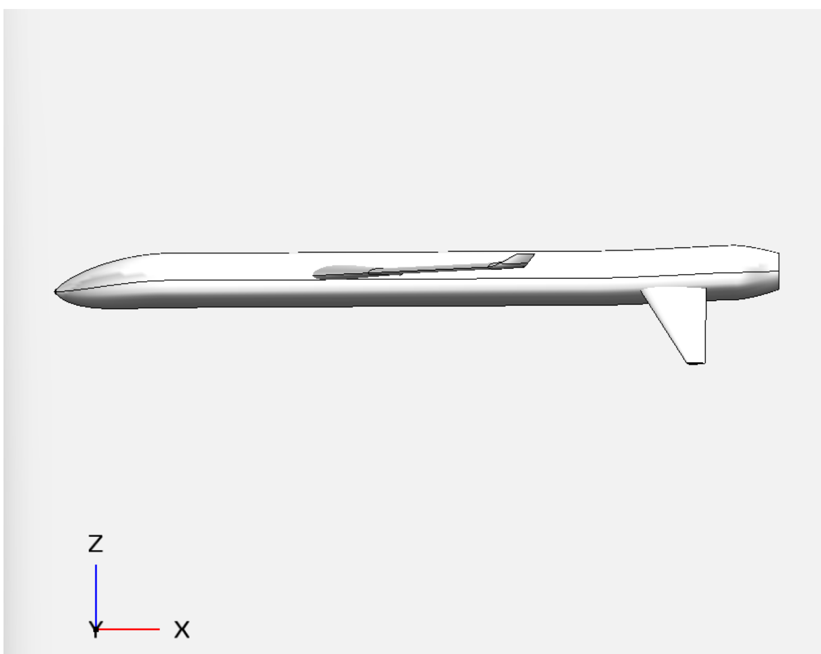

Figure 17. Design Iteration 2 Side View

Next, using the same general wing and fuselage configuration, the tail geometry was modified by inverting the V-tail to evaluate its impact on longitudinal stability. This change was intended to alter the vertical and horizontal force components generated by the tail and potentially improve the overall pitching moment characteristics. However, it was found that this modification produced no significant improvement in longitudinal stability, and the configuration remained unstable in pitch.

This behavior is evident in Figure 7(d), where the pitching moment coefficient continues to increase with angle of attack, resulting in a positive slope. As with the previous upright V-tail configuration, this indicates that the aircraft produces a nose-up pitching moment as angle of attack increases, rather than a restoring nose-down moment. Therefore, the inverted V-tail configuration also exhibits longitudinal instability, and the change in tail orientation alone is insufficient to correct the issue.

From an aerodynamic performance standpoint, the inverted configuration shows very similar trends to the previous design. The lift curve in Figure 7(a) remains highly linear across the full angle of attack range, indicating consistent lift behavior and no major changes in lift-curve slope. The drag polar in Figure 7(b) retains its expected parabolic shape, and the drag breakdown indicates that parasite drag remains relatively constant while induced drag increases with lift. The minimum drag coefficient still occurs near small negative angles of attack, and the overall drag levels are comparable to the upright V-tail configuration.

The lift to drag ratio, shown in Figure 7(c), again reaches a maximum value of approximately 26 at an angle of attack of 10 deg, which is close to the previous configuration. This suggests that inverting the V-tail has minimal impact on overall aerodynamic efficiency.

The drag component plot further confirms that the aerodynamic characteristics of the configuration remain largely unchanged. Parasite drag follows a similar trend to the previous case, while induced drag increases with angle of attack as expected. The total drag curve maintains a similar minimum and curvature, reinforcing the conclusion that the primary aerodynamic behavior is dominated by the wing rather than the tail orientation.

Based on these results, it was concluded that the lack of longitudinal stability is not primarily caused by the orientation of the V-tail, but rather by the relative placement of the center of gravity and aerodynamic center. The center of gravity is likely positioned too far aft relative to the wing, resulting in a reduced or negative static margin. As a result, further design efforts were directed toward modifying the overall geometry rather than the tail orientation alone. It was determined that shortening the overall fuselage length and shifting the center of gravity forward relative to the wing aerodynamic center would be necessary to achieve a stable configuration. Like the last configuration, no further analysis was carried out because of the lack of longitudinal stability.

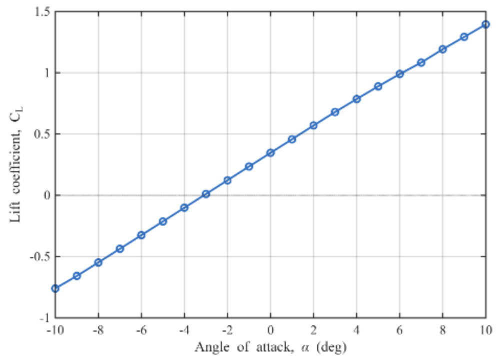

(a) Lift coefficient as a function of angle of attack.

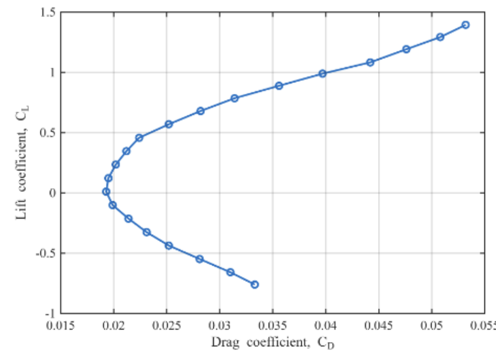

(b) Drag polar for the configuration.

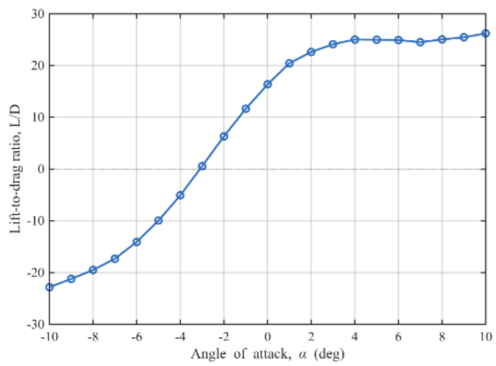

(c) Lift-to-drag ratio as a function of angle of attack.

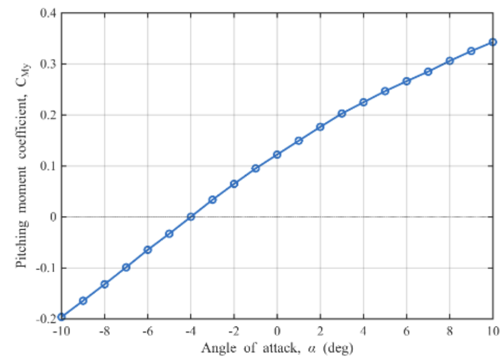

(d) Pitching moment coefficient as a function of angle of attack.

Figure 18. Design Iteration 2 Aerodynamic Performance

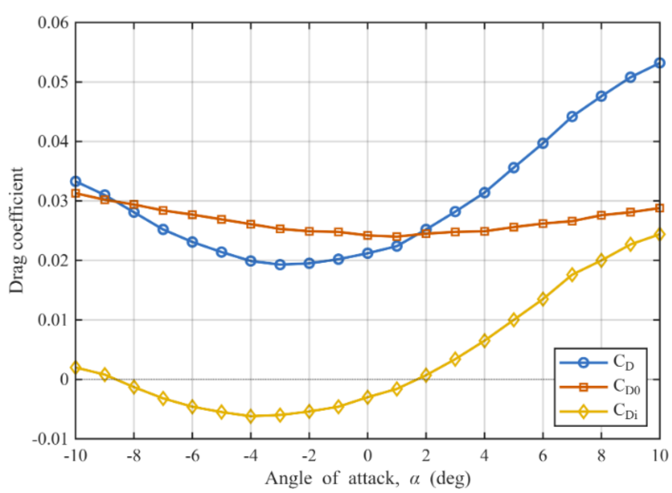

Figure 19. Design Iteration 2 Drag Breakdown

3.1.3 Design Iteration 3

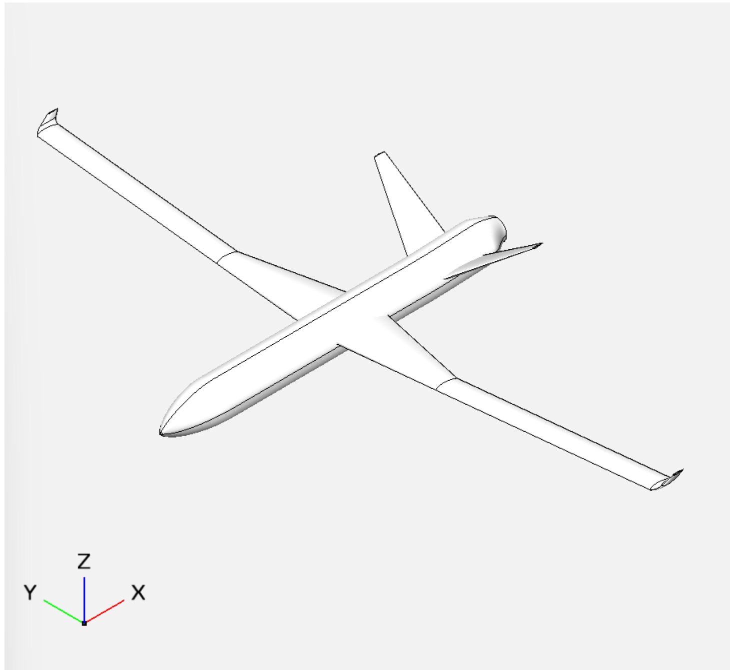

Figure 20. Design Iteration 4 Isometric View

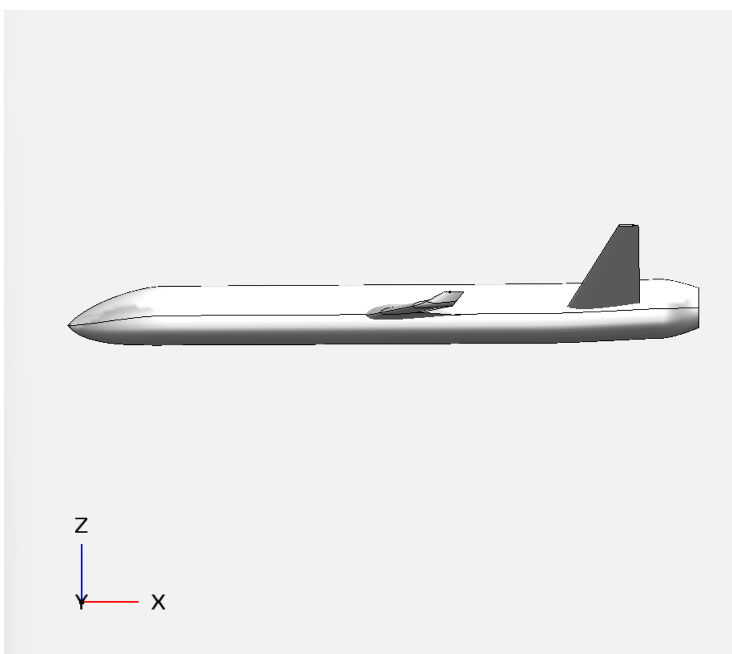

Figure 21. Design Iteration 3 Side View

Based on the results of the previous two configurations, several key geometric modifications were implemented to improve longitudinal stability and overall aerodynamic performance. The fuselage length was reduced from 40 ft to 32 ft to bring the center of gravity and aerodynamic center into closer alignment, thereby increasing the static margin. In addition, the wing sweep angle was reduced from 19.5 deg to 5 deg to better reflect the low-speed operating regime of the UAV, where high sweep is likely unnecessary.

Further modifications included introducing a positive tail incidence angle of 2 deg to increase tail downforce and improve trim characteristics, targeting a desired operating angle of attack in the range of 2 to 5 deg. The wing leading edge was also shifted aft from 14 ft to 15 ft and lowered in the vertical direction from 0.25 ft to 0 ft. These adjustments were made to better align the center of gravity with the wing aerodynamic center and to improve the overall pitching moment behavior of the configuration.

These changes resulted in a significant improvement in longitudinal stability, as shown in Figure 11(d). Unlike the previous configurations, which exhibited a positive slope in the pitching moment curve, this iteration shows a clear negative slope of pitching moment coefficient with respect to angle of attack. This indicates that the aircraft now produces a restoring pitching moment in response to disturbances, confirming that the configuration is longitudinally stable. In addition, the pitching moment curve crosses near zero within the desired operating range, indicating that the aircraft can be trimmed at a practical angle of attack suitable for loiter conditions.

From an aerodynamic performance standpoint, the lift characteristics remain largely unchanged, as shown in Figure 11(a). The lift coefficient continues to vary linearly with angle of attack, indicating consistent lift-curve behavior and no degradation in lift performance due to the geometric modifications. The drag polar in Figure 11(b) maintains its expected parabolic shape, with only minor changes in magnitude. The minimum drag coefficient appears slightly reduced compared to previous configurations, suggesting a modest improvement in aerodynamic efficiency, likely due to the reduced sweep and improved alignment of the aircraft components.

The drag breakdown further supports this observation. Parasite drag remains relatively consistent across the angle of attack range, while induced drag increases with lift as expected. The lift to drag ratio, shown in Figure 11(c), remains high, with a peak value around 26 occurring near an angle of attack of 10 deg. This is comparable to, or slightly improved from, the previous configurations, indicating that the improvements in stability were achieved without sacrificing aerodynamic efficiency.

Overall, this iteration represents a substantial improvement over the previous designs. While earlier configurations were aerodynamically efficient but longitudinally unstable, the current configuration achieves both stable pitching behavior and strong aerodynamic performance. These results confirm that proper alignment of the center of gravity relative to the aerodynamic center, along with appropriate tail incidence and reduced wing sweep, are important factors in achieving a viable and well balanced UAV design.

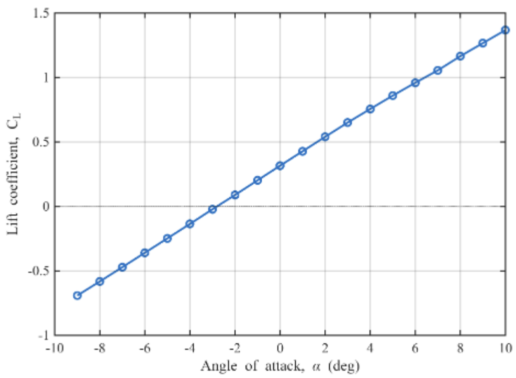

(a) Lift coefficient as a function of angle of attack.

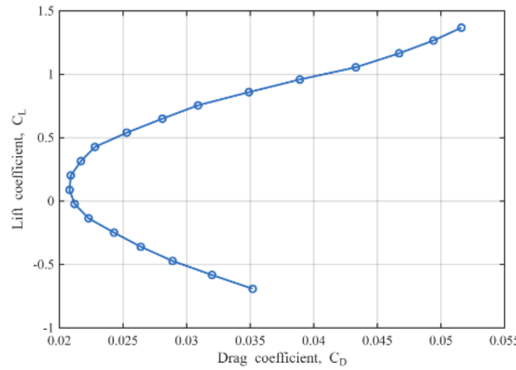

(b) Drag polar for the configuration.

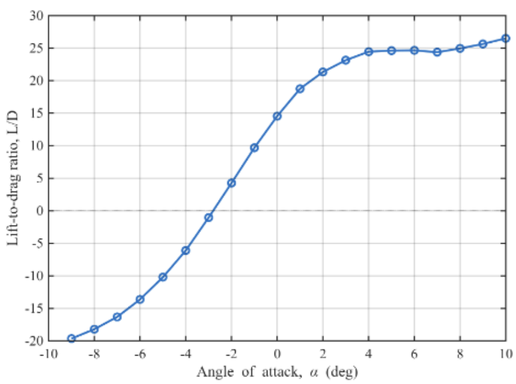

(c) Lift-to-drag ratio as a function of angle of attack.

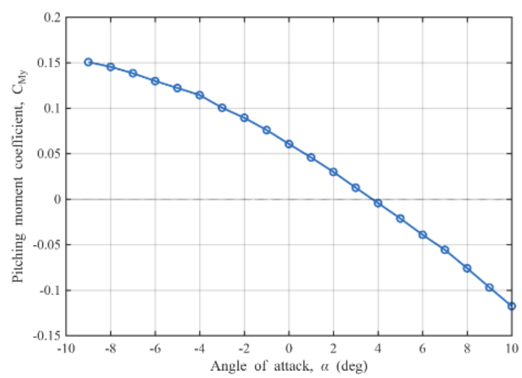

(d) Pitching moment coefficient as a function of angle of attack.

Figure 22. Design Iteration 3 Aerodynamic Performance

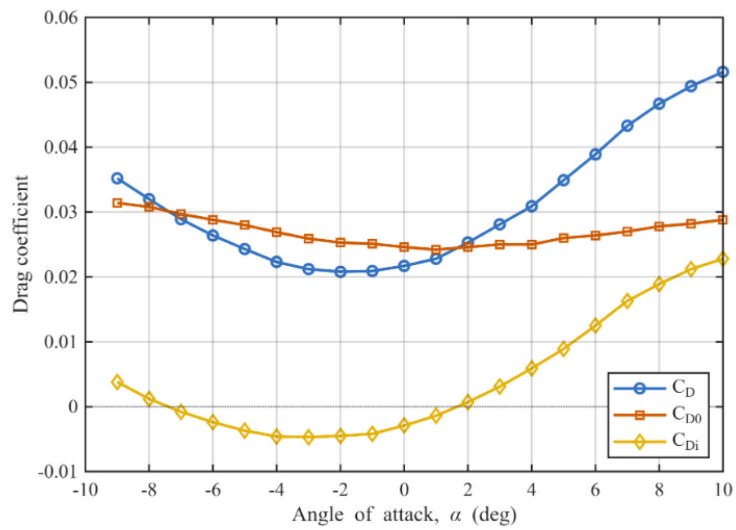

Figure 23. Design Iteration 3 Drag Breakdown

Given that this iteration demonstrated acceptable longitudinal stability, a lateral-directional stability analysis was subsequently performed by sweeping the sideslip angle, beta, from -10 deg to 10 deg, as described previously. The sweep over sideslip angle was performed at the trim angle of attack of 3.5 deg. The resulting yawing moment, rolling moment, and side-force coefficients are shown in Figure 14. Interpretation of these results must be made using FlightStream's sign convention rather than a standard textbook convention. In FlightStream, positive beta corresponds to the aircraft nose turning to the left when viewed from above, while negative beta corresponds to the nose turning to the right. In addition, FlightStream reports CMx, CMy, and CMz as the rolling, pitching, and yawing moment coefficients about the x, y, and z axes, respectively, using its own positive rotation convention.

As shown in Figure 14(a), the yawing moment coefficient, CMz, decreases as beta increases, giving a negative slope. Under a standard aircraft stability sign convention, this might initially appear destabilizing, however, under the FlightStream convention it corresponds to a restoring yaw response. Physically, a positive beta means the nose has been displaced to the left. For the aircraft to be directionally stable, the aerodynamic yawing moment must act in the opposite direction to rotate the nose back to the right and realign the vehicle with the freestream. In FlightStream, this restoring behavior appears as a negative CMz at positive beta, which is exactly the trend observed in the plot. Therefore, the negative slope of CMz with respect to beta indicates positive directional stability for this configuration.

A similar interpretation applies to the rolling moment coefficient shown in Figure 14(b). The rolling moment coefficient, CMx, increases with beta, producing a positive slope. Again, this sign must be interpreted using FlightStream's convention. For a stable lateral response, a sideslip disturbance should generate a corrective rolling moment that opposes the disturbance and tends to restore the aircraft toward equilibrium. In FlightStream's sign system, that restoring rolling tendency appears as a positive CMx for positive beta. Therefore, the positive slope of CMx with respect to beta indicates that the aircraft is laterally stable in roll.

The side force coefficient shown in Figure 14(c) varies approximately linearly with sideslip angle, indicating that the configuration generates a consistent and predictable lateral aerodynamic response over the tested range. This is desirable because it suggests that the lateral-directional characteristics remain well behaved between -10 deg and 10 deg sideslip. Figure 20(d), which presents CMx and CMz together, further demonstrates that both the roll and yaw responses vary smoothly and almost linearly with beta, reinforcing the conclusion that the aircraft produces restoring moments in response to sideslip disturbances.

Overall, when interpreted using FlightStream's sign convention, the results indicate that this configuration is statically stable in both yaw and roll. This means that a sideslip disturbance causes the aircraft to generate corrective yawing and rolling moments that tend to return it toward its trimmed condition, indicating lateral directional static stability.

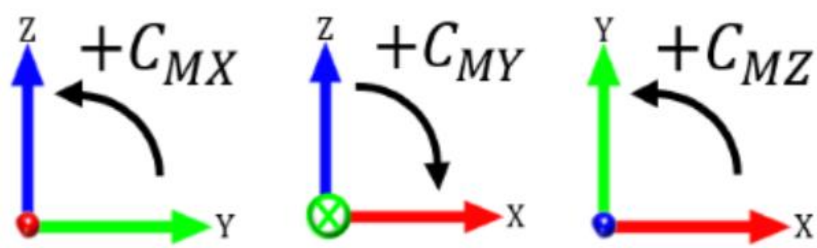

Figure 24. FlightStream Stability Coefficient Sign Convention

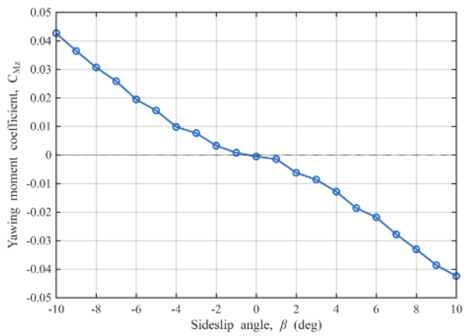

(a) Yawing moment coefficient as a function of sideslip angle.

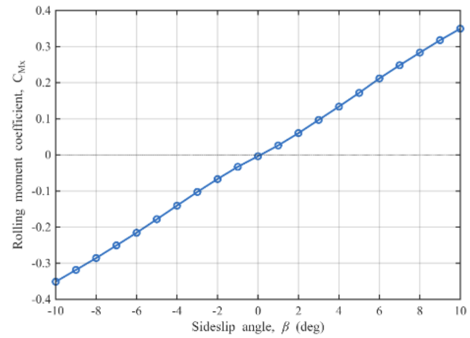

(b) Rolling moment coefficient as a function of sideslip angle.

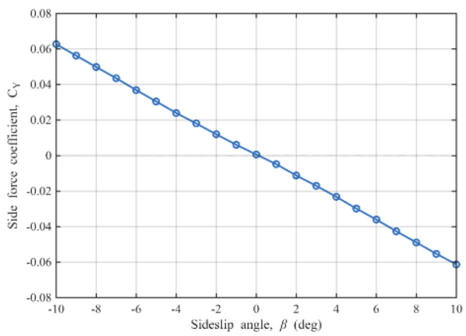

(c) Side-force coefficient as a function of sideslip angle.

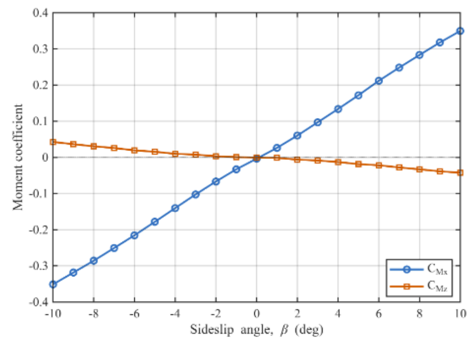

(d) Rolling and yawing moment coefficients as functions of sideslip angle.

Figure 25. Design Iteration 3 Lateral Stability Characteristics

Finally, Figures 15 and 16 show isometric and front view flow images at a 10 deg angle of attack and no sideslip, which provides an additional visualization of the computed flow field. The residual history is also shown and confirms the solver convergence. The wing loading, shear, and bending moment diagrams are shown in Figure 17.

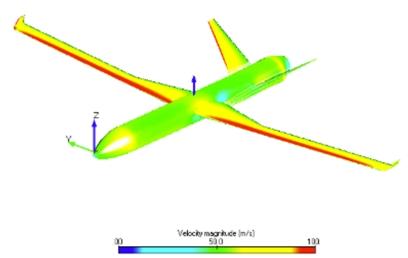

(a) Velocity contour for the baseline 15 ft V-tail configuration.

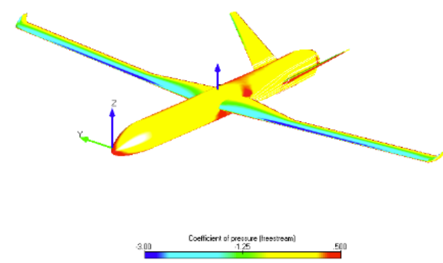

(b) Pressure coefficient contour for the baseline 15 ft V-tail configuration.

Figure 26. Design Iteration 3 Velocity and Pressure Contour Plots

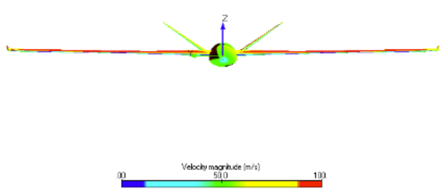

(a) Front-view flow image for the baseline 15 ft V-tail configuration.

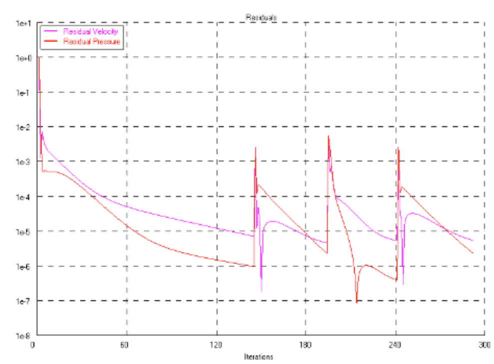

(b) Solver residual history for the baseline 15 ft V-tail configuration.

Figure 27. Design Iteration 3 Front View Flow Field and Solver Residual History

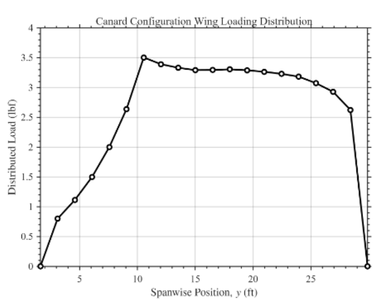

(a) Wing loading distribution.

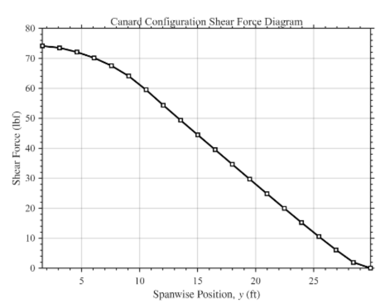

(b) Shear force diagram.

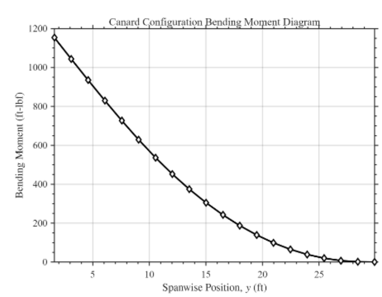

(c) Bending moment diagram.

Figure 28. Design Iteration 3 Wing Loading, Shear, and Bending Moment Diagrams

3.1.4 Design Iteration 4

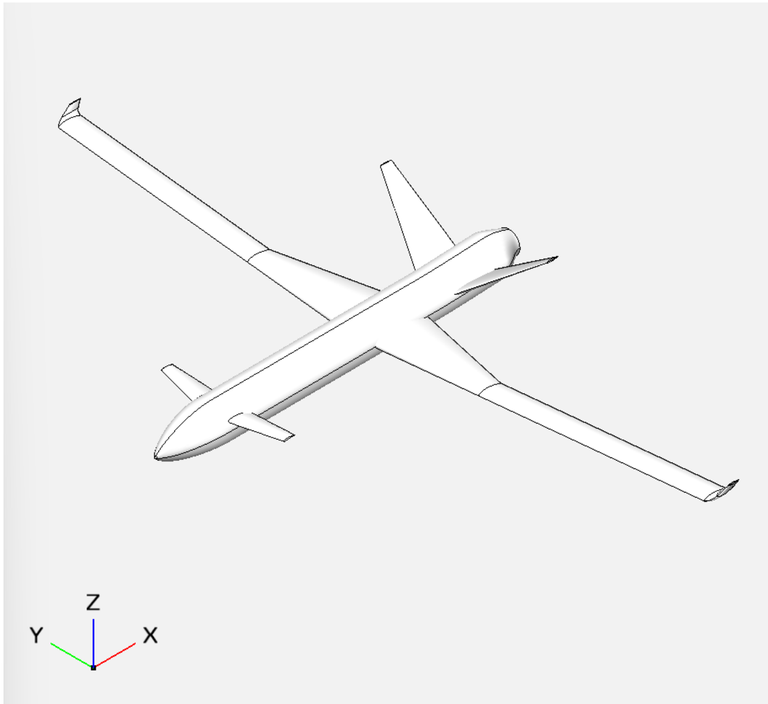

Figure 29. Design Iteration 4 Isometric View

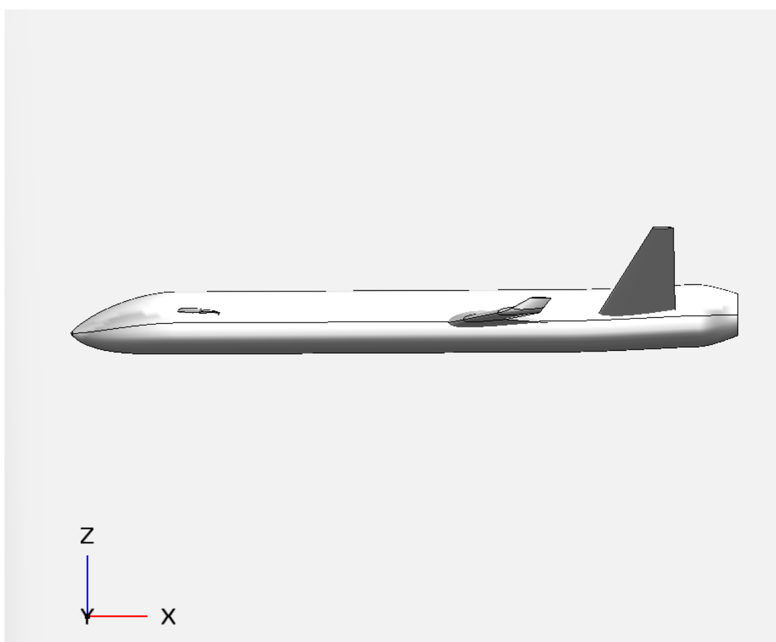

Figure 30. Design Iteration 4 Side View

Table 27: Weight & Cost Estimation 2

UNIT #	EQUIPMENT	NAME	WEIGHT [LB]	COST [$]
1	Propulsion System	Honeywell TPE331-10N	385	$1,500,000
2	Flight computer	Honeywell H-764 ACE	18	$175,000
3	Optics Package	L3Harris WESCAM MX-20D	120	$2,500,000
4	Battery	Tattu 6S 16000mAh LiPo Battery	3.75	$300
5	Radar	Lynx Multi-Mode Radar (General Atomics)	160	$2,000,000
6	Fuel Tanks	Integral wing + fuselage bladder tanks (210 gal usable)	65	$45,000
7	Fuel	JP-8 (amount = 210 gallons)	1407	$1,260
8	Structure (without the fuel, fuel tanks, landing	Carbon-fiber composite airframe with sandwich panels and spars	1100	$420,000
9	Landing Gear	Fixed tricycle gear, oleo/composite/aluminum assembly	95	$30,000
	TOTAL ESTIMATED WEIGHT & COST		3353.75	$6,671,560

Table 5 shows the estimated total weight and cost for design iteration 4. The values were calculated using the data provided in Section 2 (Figures 1–4), where the cost and weight of each subsystem were summed and reported in the bottom right of the figure. Since iteration 4 has a canard in the design, which means more material, which leads to more cost and weight. The expected cost and weight of iteration 4 is higher than iterations 1, 2, and 3.

Next, a canard configuration was investigated to explore alternative approaches to improving longitudinal stability and stall behavior. Canard configurations offer several advantages when properly designed, particularly by ensuring that the forward lifting surface stalls prior to the main wing. This characteristic improves stall safety by preventing deep stall conditions and promoting natural recovery. Additionally, the forward wing contributes to the overall lift distribution and pitching moment balance of the aircraft.

The canard geometry was initially sized using a first-pass analytical method based on established design procedures outlined in canard design literature [51]. A MATLAB script was developed to implement this methodology, allowing for rapid estimation of the canard and main wing areas, lift distribution, aerodynamic center locations, and static margin. The script also evaluates stall sequencing to ensure that the canard stalls before the main wing, which is a critical requirement for stable canard configurations.

Based on this approach, a canard with a span of 4 ft, root chord of 2 ft, and tip chord of 1 ft was selected, resulting in a moderately tapered planform. The canard was given a leading-edge sweep of 15 deg and utilized the Wortmann FX 63-137 airfoil. This airfoil was selected due to its relatively high camber, which promotes higher lift coefficients at lower angles of attack and improves the ability of the canard to carry the required load. This selection was further supported by recommendations from canard design discussions in [52]. The canard was mounted with a root incidence angle of 5 deg to ensure that it operates at a higher effective angle of attack than the main wing, thereby promoting the desired stall sequencing.

In terms of placement, the canard leading edge was positioned 5 ft from the nose of the UAV and 1.55 ft above the fuselage centerline. The main wing geometry was also adjusted in conjunction with the canard addition. Specifically, the wing leading edge was shifted aft to 18 ft from the nose of the UAV to ensure that it remained aft of the center of gravity. This adjustment was critical in achieving a favorable moment balance and improving the overall static margin of the configuration.

The aerodynamic performance of the canard configuration is shown in Figure 20. The lift-curve remains approximately linear across the analyzed angle of attack range, indicating consistent lift behavior and no degradation in lift-curve slope due to the addition of the canard. The drag polar maintains a typical parabolic shape, and the drag breakdown shows expected trends, with parasite drag remaining relatively constant and induced drag increasing with lift.

In terms of efficiency, the lift to drag ratio reaches a maximum value of 25 at an angle of attack of 10 deg. This represents a slight reduction compared to previous tail-aft configurations, which achieved peak values closer to 26 to 27. This decrease is partially expected, as the addition of a forward lifting surface introduces additional induced drag and interference effects.

The most significant improvement observed in this configuration is in longitudinal stability. As shown in Figure 20(d), the pitching moment coefficient now exhibits a clear negative slope with respect to angle of attack, indicating a statically stable configuration. Additionally, the pitching moment curve crosses near zero within a practical operating range, indicating that the aircraft can be trimmed at a desirable angle of attack suitable for loiter conditions.

Compared to the previous tail-aft configurations, the canard design achieves stability through a fundamentally different mechanism. Rather than relying on a rear tail to generate a restoring moment, the forward lifting surface contributes directly to the overall pitching moment balance. Proper sizing, placement, and incidence of the canard ensure that it carries sufficient lift while maintaining favorable stall behavior and stability characteristics.

Overall, the canard configuration represents a successful design iteration. While it introduces a modest reduction in aerodynamic efficiency, it provides valuable insight into canard effect on longitudinal stability and trim behavior. These results demonstrate that proper geometric alignment, particularly ensuring that the wing aerodynamic center is aft of the center of gravity combined with an appropriately sized and positioned canard, is critical in achieving a stable and well-balanced UAV design.

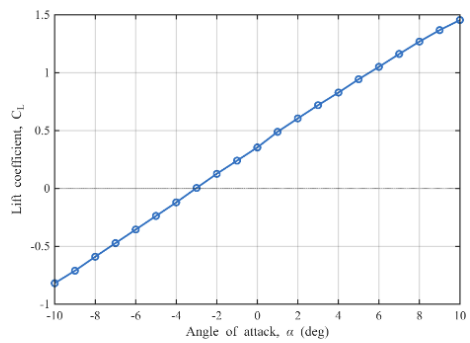

(a) Lift coefficient as a function of angle of attack.

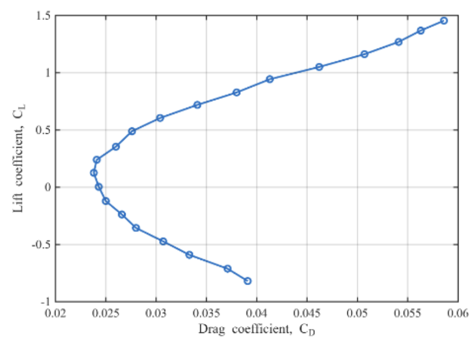

(b) Drag polar for the configuration.

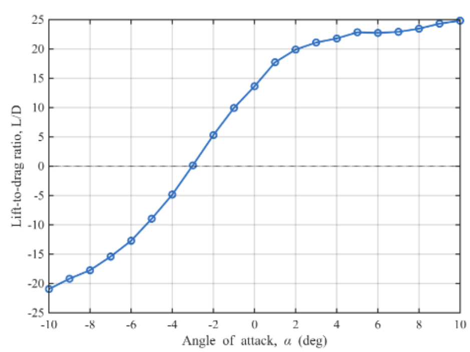

(c) Lift-to-drag ratio as a function of angle of attack.

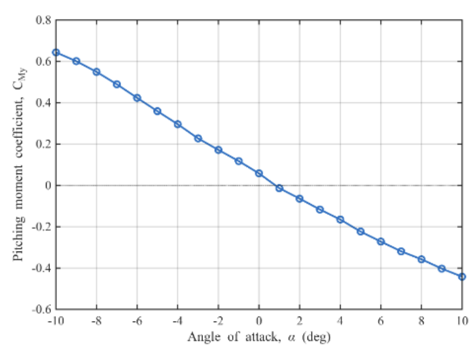

(d) Pitching moment coefficient as a function of angle of attack.

Figure 31. Design Iteration 4 Aerodynamic Performance

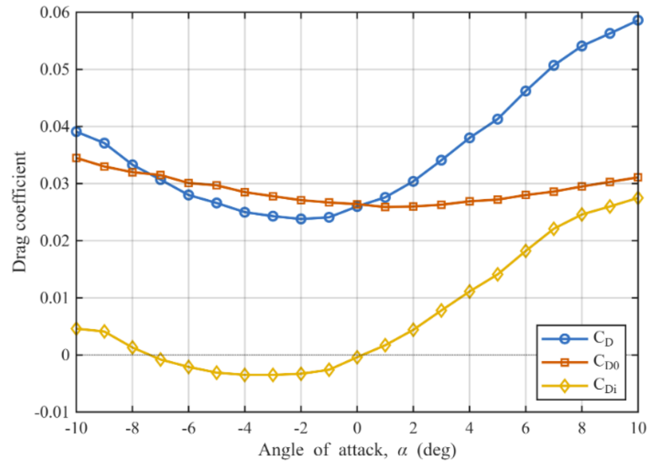

Figure 32. Design Iteration 4 Drag Breakdown

Like the design iteration 3, given that the canard configuration also demonstrated acceptable longitudinal stability, a lateral-directional stability analysis was performed by sweeping the sideslip angle, beta, from -10 deg to 10 deg. As with the previous design iteration, the sweep across sideslip angles was performed at the trim angle of attack of 1 deg. The resulting yawing moment, rolling moment, and side-force coefficient trends are shown in Figure 20. As with the previous lateral stability analysis, these results must be interpreted using FlightStream's sign convention, in which positive beta corresponds to the nose turning to the left when viewed from above, and CMx and CMz represent the rolling and yawing moment coefficients, respectively.

Overall, the canard configuration exhibits the same general stability trends observed in the previous configuration, indicating favorable lateral-directional static stability. The yawing moment coefficient decreases with increasing beta, while the rolling moment coefficient increases with beta, which under FlightStream's convention corresponds to restoring yawing and rolling responses to a sideslip disturbance. The side-force coefficient also varies nearly linearly across the tested range, indicating a consistent lateral aerodynamic response.

Compared to the previous configuration, the canard design appears to produce a somewhat stronger lateral-directional response. In particular, the magnitudes of both the rolling moment and side-force coefficients are larger across the sideslip range, suggesting that the canard configuration is more sensitive to sideslip disturbances and generates stronger corrective aerodynamic forces and moments. The yawing moment response is also slightly stronger, particularly at larger values of beta, although the overall trend remains similar to the previous design. Additionally, the canard configuration shows a small amount of nonlinearity in the yawing moment response at higher sideslip angles, whereas the previous configuration was somewhat more linear over the full range. However, this deviation is not severe and does not appear to indicate a loss of lateral-directional stability.

In summary, the canard configuration maintains favorable lateral-directional stability while producing somewhat stronger rolling, yawing, and side-force responses than the previous tail-aft configuration. This suggests that, in addition to improving longitudinal stability, the canard design also preserves acceptable lateral-directional stability characteristics and may provide a more responsive overall aerodynamic behavior.

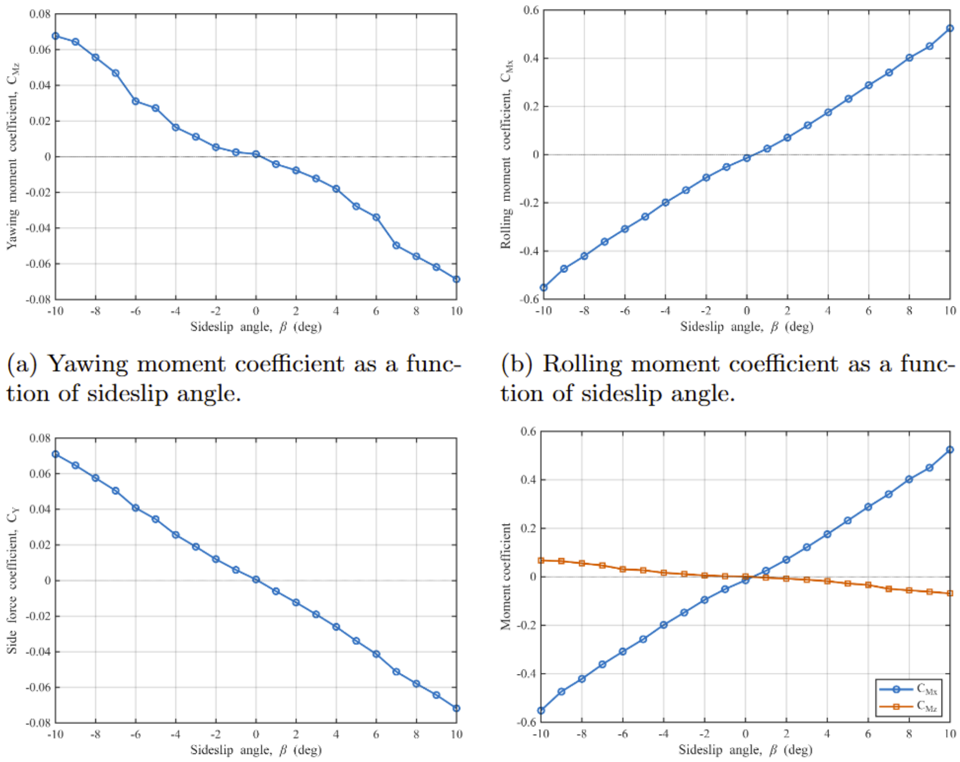

(a) Yawing moment coefficient as a function of sideslip angle.

(b) Rolling moment coefficient as a function of sideslip angle.

(c) Side-force coefficient as a function of sideslip angle.

(d) Rolling and yawing moment coefficients as functions of sideslip angle.

Figure 33. Design Iteration 4 Lateral Stability Characteristics

As previously, Figures 23 and 24 show isometric and front view flow images at a 10 deg angle of attack and no sideslip, which provides an additional visualization of the computed flow field. The residual history is also shown and confirms the solver convergence. Finally, the wing loading, shear, and bending moment diagrams are shown in Figure 24.

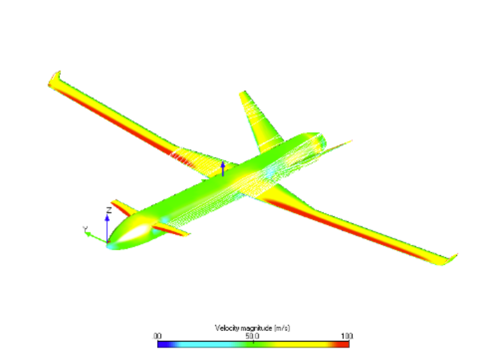

(a) Velocity contour for the 15 ft V-tail configuration with canard.

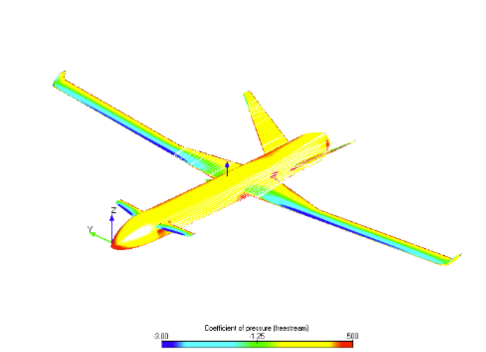

(b) Pressure coefficient contour for the 15 ft V-tail configuration with canard.

Figure 34. Design Iteration 4 Velocity and Pressure Contour Plots

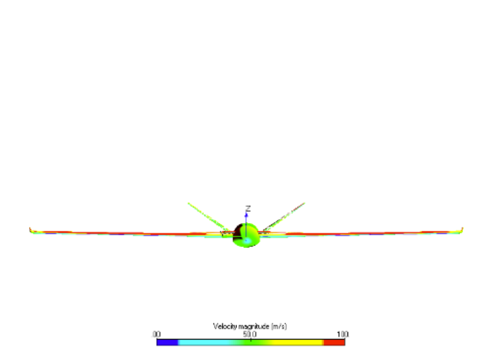

(a) Front-view flow image for the 15 ft V-tail configuration with canard.

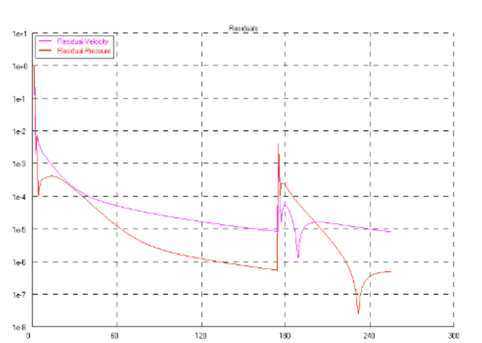

(b) Solver residual history for the 15 ft V-tail configuration with canard.

Figure 35. Design Iteration 4 Front View Flow Field and Solver Residual History

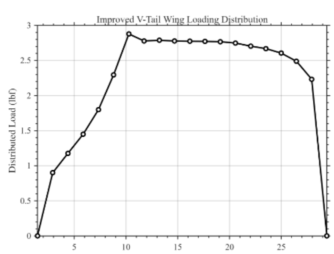

(a) Wing loading distribution.

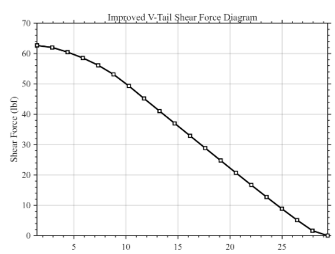

(b) Shear force diagram.

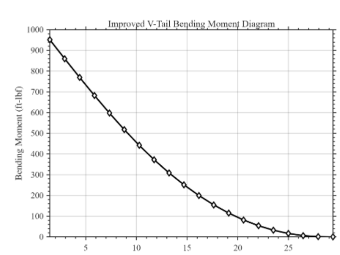

(c) Bending moment diagram.

Figure 36. Design Iteration 4 Wing Loading, Shear, and Bending Moment Diagrams

3.1.5 Design Iteration 5

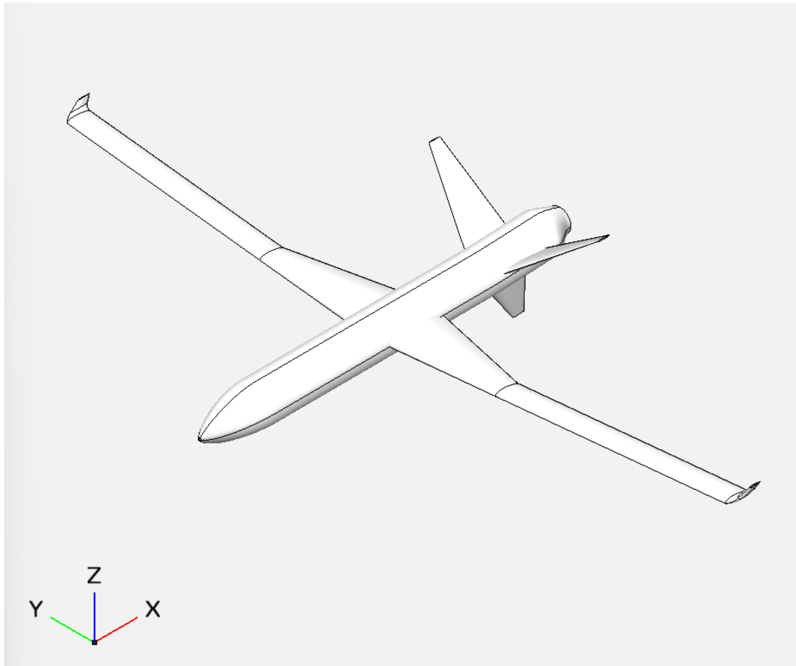

Figure 37. Design Iteration 5 Isometric View

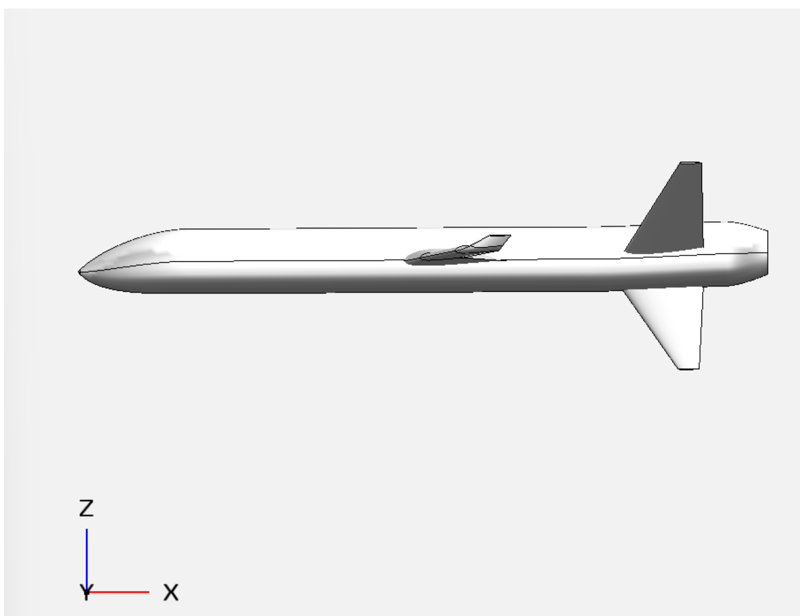

Figure 38. Design Iteration 5 Side View

Table 28: Weight & Cost Estimation 3

UNIT #	EQUIPMENT	NAME	WEIGHT [LB]	COST [$]
1	Propulsion System	Honeywell TPE331-10N	385	$1,500,000
2	Flight computer	Honeywell H-764 ACE	18	$175,000
3	Optics Package	L3Harris WESCAM MX-20D	120	$2,500,000
4	Battery	Tattu 6S 16000mAh LiPo Battery	3.75	$300
5	Radar	Lynx Multi-Mode Radar (General Atomics)	160	$2,000,000
6	Fuel Tanks	Integral wing + fuselage bladder tanks (210 gal usable)	65	$45,000
7	Fuel	JP-8 (amount = 210 gallons)	1407	$1,260
8	Structure (without the fuel, fuel tanks, landing	Carbon-fiber composite airframe with sandwich panels and spars	1055	$435,000
9	Landing Gear	Fixed tricycle gear, oleo/composite/aluminum assembly	95	$30,000
TOTAL ESTIMATED WEIGHT & COST			3308.75	$6,686,560

Table 6 shows the estimated total weight and cost for design iteration 5. The values were calculated using the data provided in Section 2 (Figures 1–4), where the cost and weight of each subsystem were summed and reported in the bottom right of the figure. Since iteration 5 has a vertical tail, it has more material than iterations 1, 2, and 3. This led to an increase in cost and weight, but iteration 5 was not heavier than iteration 4.

The fifth and final design iteration considered for this report adds a vertical tail to design iteration 3, making a Y-tail configuration. It uses the same NACA 0012 airfoil, has a 4ft span, 4ft root chord, 1ft tip chord, and 35 deg sweep. As with the previous designs, an angle of attack sweep from -10 deg to 10 deg was performed to evaluate lift, drag, aerodynamic efficiency, and longitudinal stability. The lift curve remained approximately linear over the full range, indicating predictable lift behavior, while the drag polar and drag breakdown followed the expected trends. The lift-to-drag ratio reached a maximum value of approximately 26 near a 7 deg angle of attack, showing that the Y-tail configuration remained competitive from an aerodynamic efficiency standpoint and performed similarly to the better previous iterations in terms of lift and drag.

The primary difference appeared in the pitching moment response. Unlike the improved conventional tail and canard configurations, which showed a clear negative slope of pitching moment coefficient with respect to angle of attack, the Y-tail configuration exhibited a pitching moment curve that remained positive and increasing over much of the analyzed range. This indicates that the aircraft did not develop a strong restoring pitching moment and was therefore less longitudinally stable than the previous successful configurations. One possible reason is that adding the vertical tail altered the aft-body flow and the interaction between the tail surfaces, reducing the stabilizing contribution that had been present in the earlier layout. As a result, although the Y-tail remained aerodynamically efficient, it did not provide the same favorable pitch stability and trim behavior as the earlier stable designs.

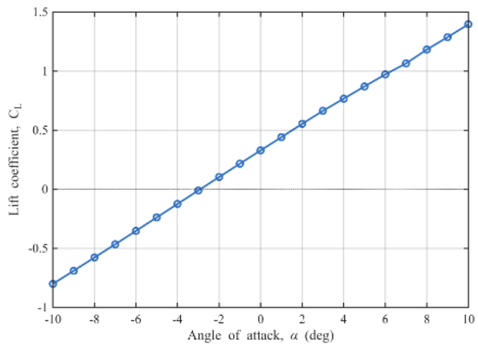

(a) Lift coefficient as a function of angle of attack.

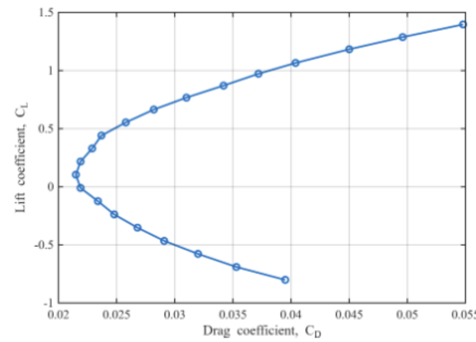

(b) Drag polar for the configuration.

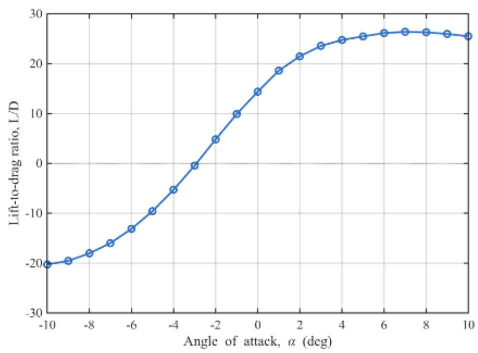

(c) Lift-to-drag ratio as a function of angle of attack.

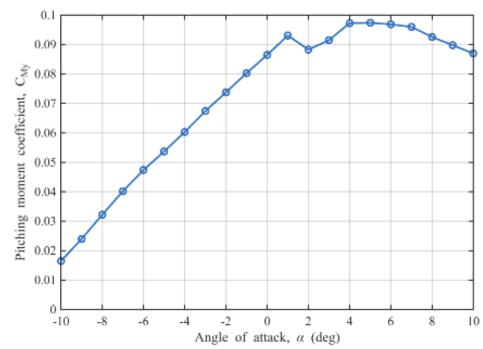

(d) Pitching moment coefficient as a function of angle of attack.

Figure 39. Design Iteration 5 Aerodynamic Performance

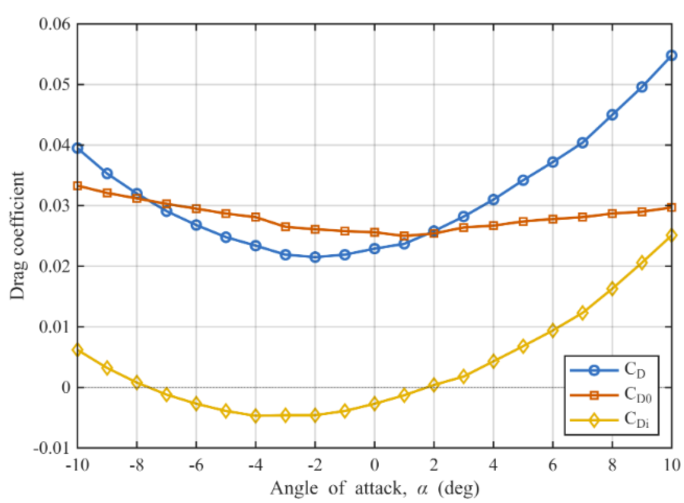

Figure 40. Design Iteration 5 Drag Breakdown

A lateral-directional stability analysis was also performed for the Y-tail configuration, where the sideslip angle was swept from -10 deg to 10 deg at 0 deg angle of attack. This angle of attack was chosen because it is simple in a case where the configuration does not have a well-defined trim angle of attack. The resulting yawing moment, rolling moment, and side-force coefficients are shown in Figure 30. As with the previous cases, these results are interpreted using FlightStream's sign convention. The Y-tail configuration continues to show favorable lateral directional stability trends, with the yawing moment coefficient decreasing linearly with increasing beta and the rolling moment coefficient increasing linearly with beta. Under FlightStream's convention, these trends correspond to restoring yawing and rolling responses, indicating that the configuration remains statically stable in both yaw and roll.

Compared to the previous stable tail-aft and canard configurations, the Y-tail produces noticeably stronger lateral-directional responses. The magnitudes of both the yawing and rolling moment coefficients are significantly larger across the full sideslip range, and the side-force coefficient also shows a stronger response to beta. This suggests that the Y-tail provides greater sensitivity to sideslip disturbances and generates stronger corrective moments than the earlier configurations. In addition, the trends are highly linear throughout the full range of beta, which indicates a smooth and predictable response. Therefore, although the Y-tail configuration was less favorable in longitudinal stability, it appears to provide the strongest lateral directional stability of the configurations considered.

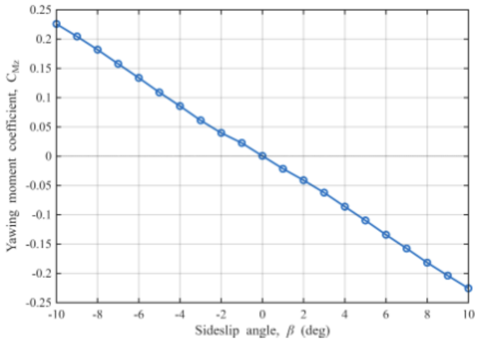

(a) Yawing moment coefficient as a function of sideslip angle.

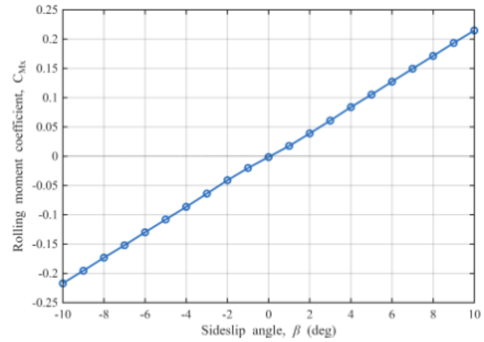

(b) Rolling moment coefficient as a function of sideslip angle.

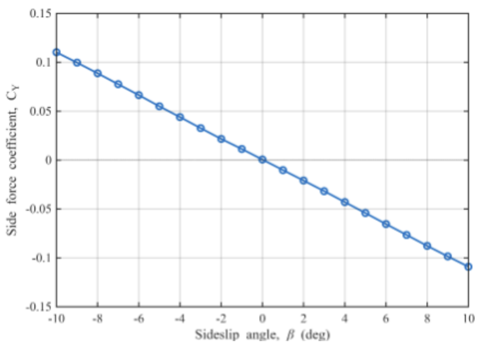

(c) Side-force coefficient as a function of sideslip angle.

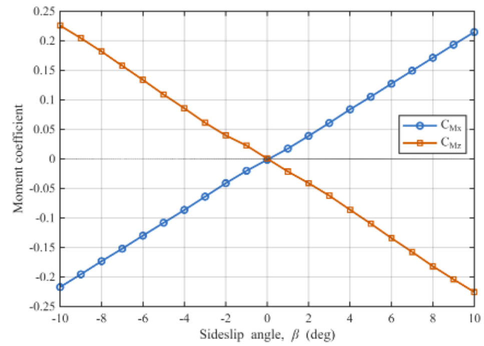

(d) Rolling and yawing moment coefficients as functions of sideslip angle.

Figure 41. Design Iteration 5 Lateral Stability Characteristics

Lastly, Figures 31 and 32 show isometric and front view flow images at a 10 deg angle of attack and no sideslip, which provides an additional visualization of the computed flow field. The residual history is also shown and confirms the solver convergence. The wing loading, shear, and bending moment diagrams are shown in Figure 33.

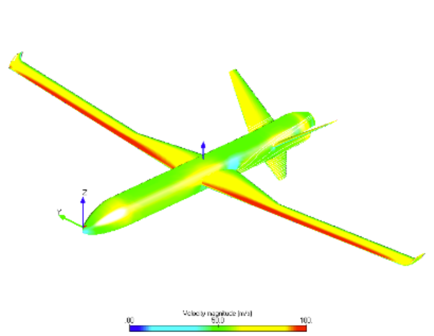

(a) Velocity contour for the 15 ft Y-tail configuration.

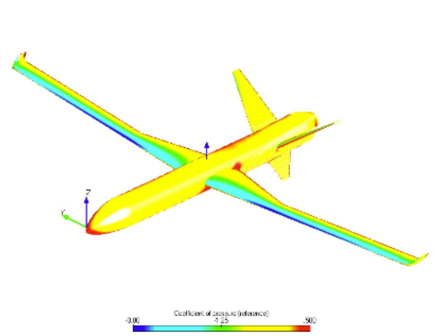

(b) Pressure coefficient contour for the 15 ft Y-tail configuration.

Figure 42. Design Iteration 5 Velocity and Pressure Contour Plots

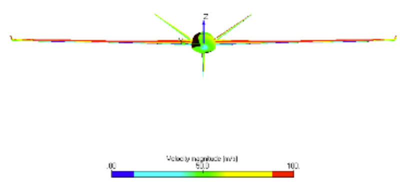

(a) Front-view flow image for the 15 ft Y-tail configuration.

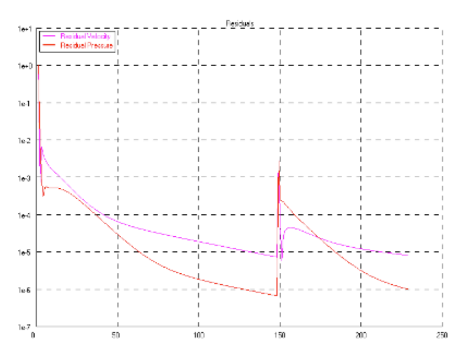

(b) Solver residual history for the 15 ft Y-tail configuration.

Figure 43. Design Iteration 5 Front View Flow Field and Solver Residual History

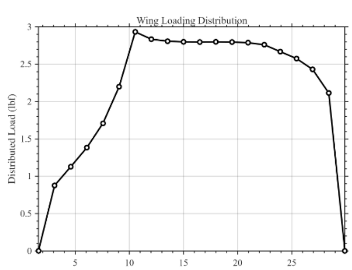

(a) Wing loading distribution.

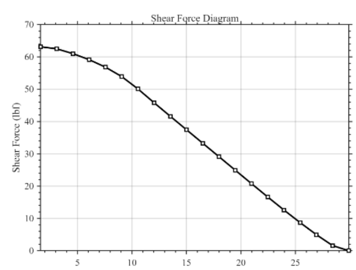

(b) Shear force diagram.

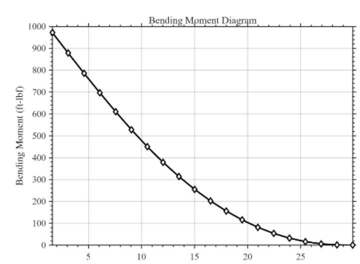

(c) Bending moment diagram.

Figure 44. Design Iteration 5 Wing Loading, Shear and Bending Moment Diagrams

A MATLAB script was developed to evaluate the performance trade-offs of the five design iterations using aerodynamic coefficients from the FlightStream models. Key sizing and performance metrics were estimated using the following mathematical formulations:

Loiter Thrust Estimation: Minimum thrust for level flight during orbit, assuming peak aerodynamic efficiency:

$$T_{loiter} = \frac{W}{\frac{L}{D}_{Max}} \tag{4}$$

where W is the takeoff weight and $\left(\frac{L}{D}\right)_{Max}$ is the maximum lift-to-drag ratio.

Takeoff Thrust Sizing: Sized to overcome inertial acceleration, aerodynamic drag, and rolling friction $\mu_{roll} \approx .04$to meet the 2,000 ft runway constraint. Stall speed V_{Stall} and liftoff speed V_{Lof} are defined as:

$$V_{Stall} = \sqrt{\frac{2W}{\rho S C_{L,max}}} \tag{5}$$

$$V_{Lof} = 1.2\, V_{stall} \tag{6}$$

The required average acceleration a_{req} over the target distance S_{req} is:

$$a_{req} = \frac{V_{Lof}^2}{2S_{req}} \tag{7}$$

Rate of Climb (ROC): Evaluated at a target climb speed V_{CLimb}) of 120 knots using the specific excess power method:

$$ROC = \frac{(T_{avail} - D)V_{CLimb}}{W} \tag{8}$$

where T_{avail} is the available sea-level thrust (Honeywell TPE331-10) and D is the aerodynamic drag.

Landing Distance Estimation: The total distance is the sum of the airborne approach (assuming a 3-degree glideslope to clear a 50 ft obstacle) and the ground roll. Ground deceleration integrates aerodynamic drag $C_D \approx .05$with deployed surfaces) and mechanical braking friction $\mu_{break} \approx .4$

Maximum Cruise Speed V_{max}: Estimated at 30,000 ft by scaling the sea-level engine thrust with the atmospheric density ratio σ:

$$\sigma = \frac{\rho_{30k}}{\rho_{SL}} \tag{9}$$

Total drag (D) is calculated using the standard drag polar:

$$D = qS(C_{D0} + KC_L^2) \tag{10}$$

V_{Max} is identified as the velocity where the required thrust D intersects the scaled available engine thrust.

Table 29: Extracted Aerodynamic & Weight Data (Inputs)

Parameter	Baseline V-Tail	Inverted V-Tail	Improved V-Tail	Canard Config	Y-Tail Config
Weight (lbs)	3203.75	3203.75	3203.75	3353.75	3308.75
Max L/D	26	26	26	24.5	26
CD0 (Parasite Drag)	0.024	0.024	0.023	0.026	0.025

The Baseline, Inverted, and Improved V-Tail configurations are the lightest (3,203.75 lbs) and most aerodynamically efficient (max L/D = 26.0). Adding extra lifting surfaces increased the structural weight of the Canard and Y-Tail configurations by 150 lbs and 105 lbs, respectively. The Canard's forward wing also introduced interference drag, dropping its max L/D to 24.5 and raising its parasite drag C_{D0} to 0.026. Conversely, the Improved V-Tail's optimized sweep and fuselage alignment resulted in the lowest overall parasite drag C_{D0} = 0.023.

Table 30: Performance Estimations

Performance Metric	Baseline V-Tail	Inverted V-Tail	Improved V-Tail	Canard Config	Y-Tail Config
Min Loiter Thrust (lbs)	123.2	123.2	123.2	136.9	127.3
Takeoff Thrust Req (lbs)	572.9	572.9	572.9	602.1	606
Rate of Climb (ft/min)	4223	4223	4223	3984	4074
Total Landing Dist (ft)	1785	1785	1785	1796	1812
Max Cruise Spd (knots)	303	303	310	291	297

Because the Baseline, Inverted, and Improved V-Tails share the same weight and maximum L/D, they require identical minimum loiter (123.2 lbs, Eq. 1) and takeoff thrusts (572.9 lbs), while achieving the highest rate of climb (4,223 ft/min, Eq. 5). The Canard and Y-Tail configurations degrade these metrics due to their added weight and drag; the Canard requires the highest loiter thrust (136.9 lbs) and yields the lowest climb rate (3,984 ft/min). The defining differentiator among the stable configurations is maximum cruise speed V_{Max}: the Improved V-Tail's minimized parasite drag allows it to reach a top speed of 310 knots, significantly outperforming both the Baseline (303 knots) and Canard (291 knots) for the same available engine thrust.

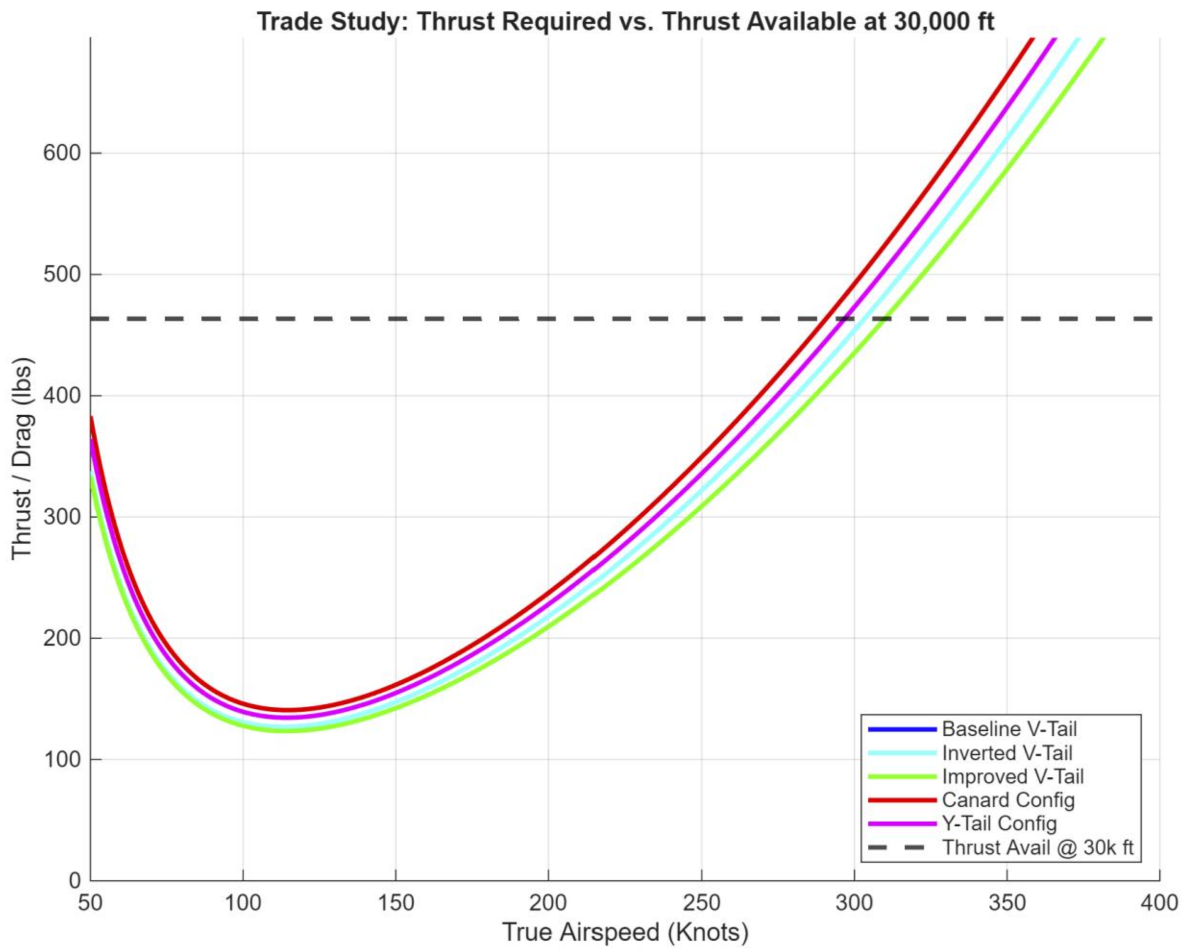

Figure 45. Thrust visualization at 30,000 ft

3.2 Trade-Off Study

A weighted decision matrix was used to compare the five candidate configurations and support final design selection. Since static stability is a critical requirement, longitudinal and lateral-directional stability were assigned the highest combined weight of 0.50, while aerodynamic efficiency, mission performance, takeoff/landing suitability, weight/cost impact, and configuration simplicity were assigned lower secondary weights. Using the aerodynamic and performance data extracted from FlightStream and the trade-study estimates, the improved V-tail configuration achieved the highest weighted total score of 4.75/5.00. This result is driven by its favorable longitudinal and lateral-directional stability, low parasite drag, highest estimated cruise speed, and lack of weight penalty relative to the early V-tail concepts. The canard configuration ranked second because it provided good stability and acceptable performance, but it was penalized for added weight, drag, and integration complexity. The Y-tail ranked third, primarily because of its strong lateral-directional response but weaker longitudinal behavior. The baseline and inverted V-tail configurations ranked last because both remained longitudinally unstable and were therefore unsuitable despite otherwise competitive aerodynamic efficiency.

Table 31: Weighted decision matrix for UAV configuration trade study

Criterion	Weight	Baseline	Inverted V	Improved V	Canard	Y-Tail
Longitudinal static stability	0.30	1	1	5	5	2
Lateral-directional stability	0.20	1	1	4	4	5
Aerodynamic efficiency	0.15	4	4	5	3	4
Mission performance	0.10	4	4	5	3	4
Takeoff/landing characteristics	0.10	5	5	5	4	3
Weight/cost impact	0.10	5	5	5	2	3
Complexity/integration risk	0.05	4	3	4	2	3
Weighted total	**1.00**	**2.70**	**2.65**	**4.75**	**3.75**	**3.35**
Rank	–	**4**	**5**	**1**	**2**	**3**

Table 32: Trade-off Study Criteria Definitions

Criterion	Weight	Basis for scoring
Longitudinal static stability	0.30	Pitching moment slope, trim behavior, and overall acceptability of longitudinal response.
Lateral-directional stability	0.20	Restoring yaw and roll response including smoothness and strength of sideslip response.
Aerodynamic efficiency	0.15	Maximum lift to drag ratio and parasite drag trends.
Mission performance	0.10	Maximum cruise speed, rate of climb, and loiter performance.
Takeoff/landing suitability	0.10	Required takeoff thrust and estimated landing distance.
Weight/cost impact	0.10	Relative mass and cost penalties introduced by additional surfaces or geometry.
Complexity/integration risk	0.05	Geometric complexity, likely manufacturing burden, and integration risk for tail or canard arrangement.

Based on the results of the trade study, the team will most likely move forward with the improved V-tail configuration for further analysis and development. This configuration provided the best overall balance of stability, aerodynamic performance, and estimated mission capability among the concepts considered. It should be noted, however, that some challenges were encountered near the deadline of this report when attempting to reliably simulate vertical tail geometries in FlightStream. As a result, additional work will be required to further validate the selected configuration. Future efforts will include expanded aerodynamic analysis in FlightStream, as well as higher-fidelity CFD and structural analysis using Star-CCM+ and NX Nastran/FEMAP.

4.0 Engineering Drawings

4.1 Drawing #1

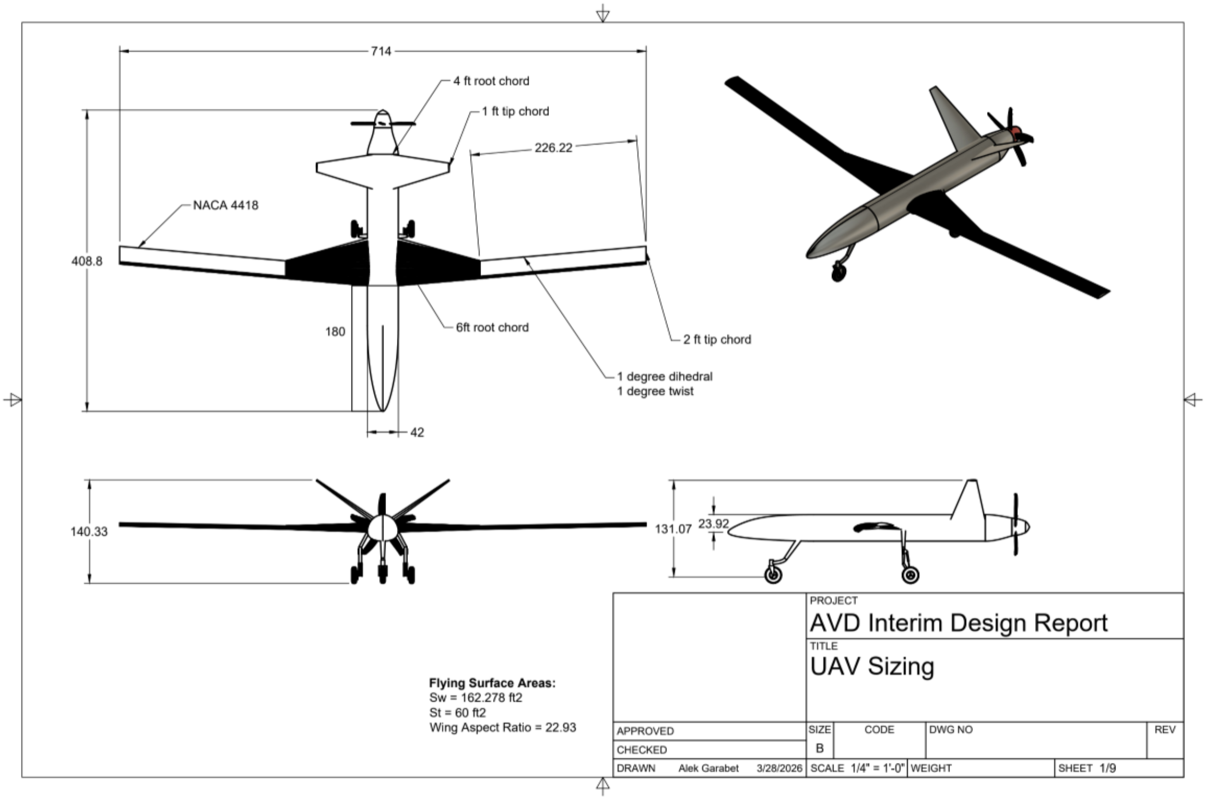

Figure 46. Isometric, Front, and Side CAD Drawings

4.2 Drawing #2

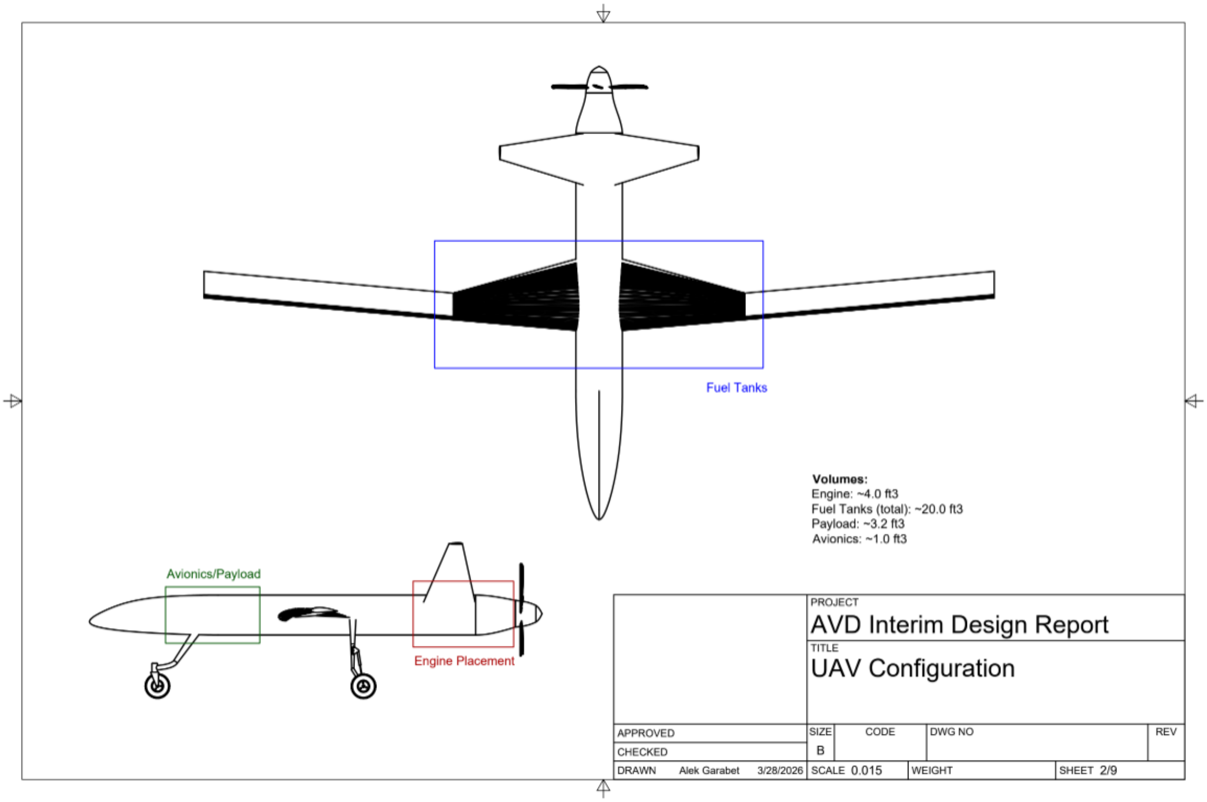

Figure 47. Volume Reference CAD Drawing

4.3 Drawing #3

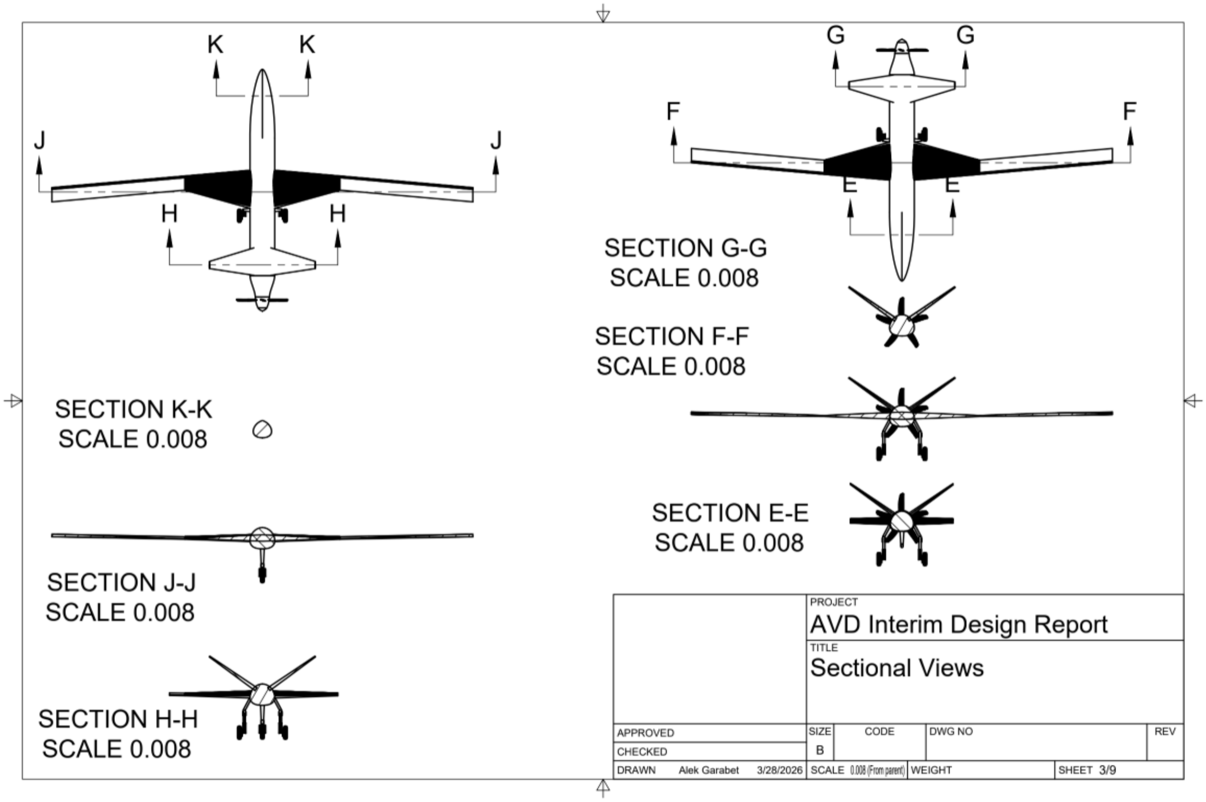

Figure 48. CAD Sectional Views CAD Drawing

4.4 Drawing #4

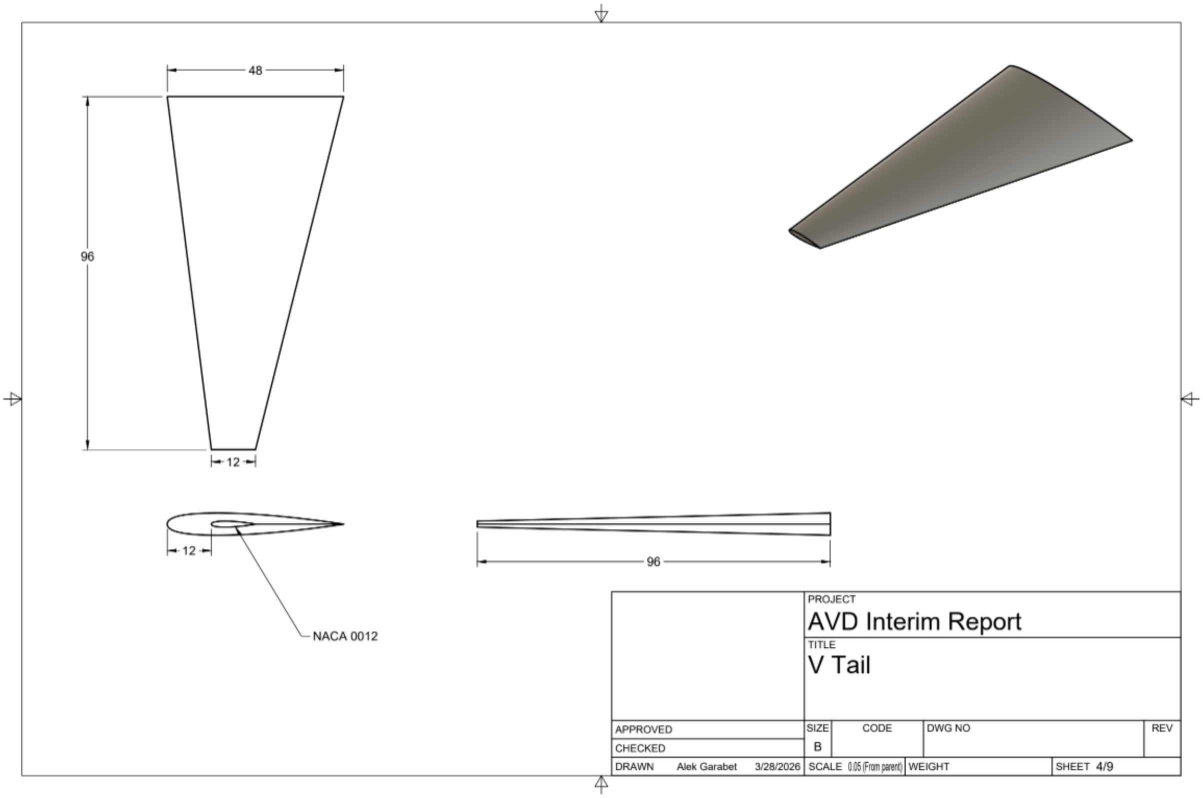

Figure 49. V Tail CAD Drawing

4.5 Drawing #5

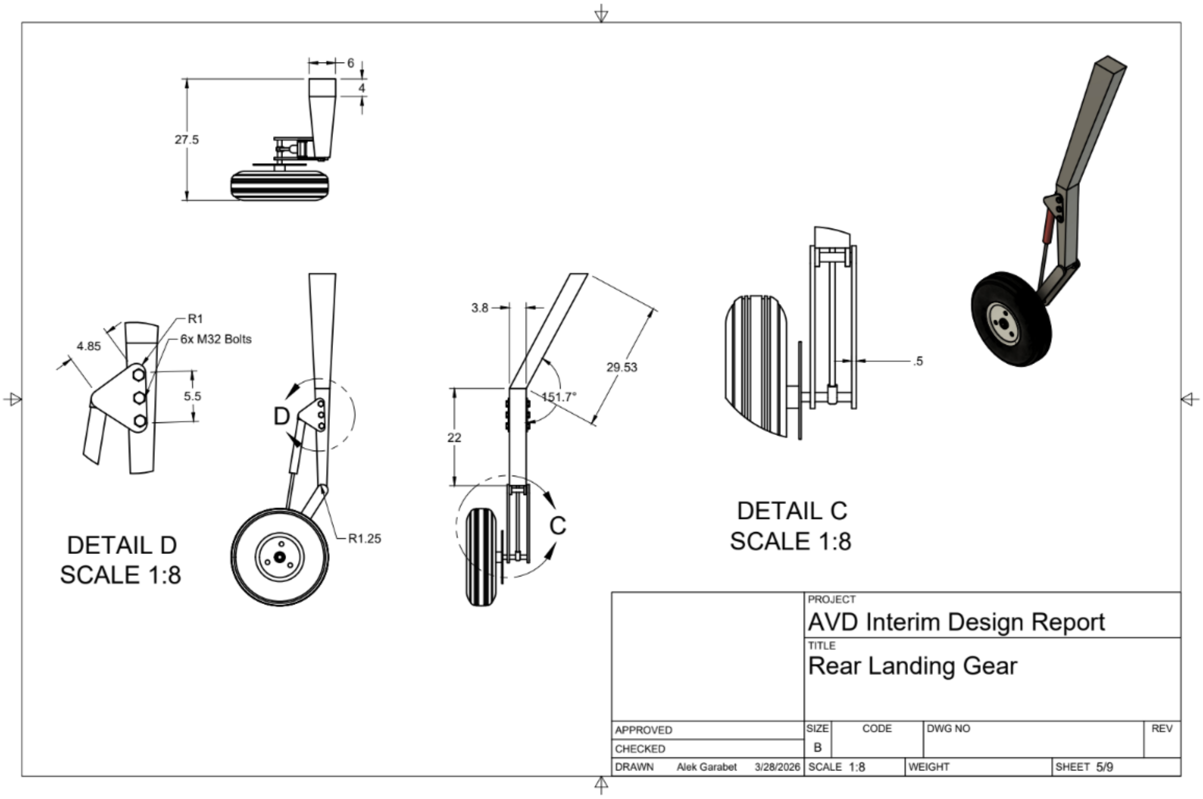

Figure 50. Rear Landing Gear CAD Drawing

4.6 Drawing #6

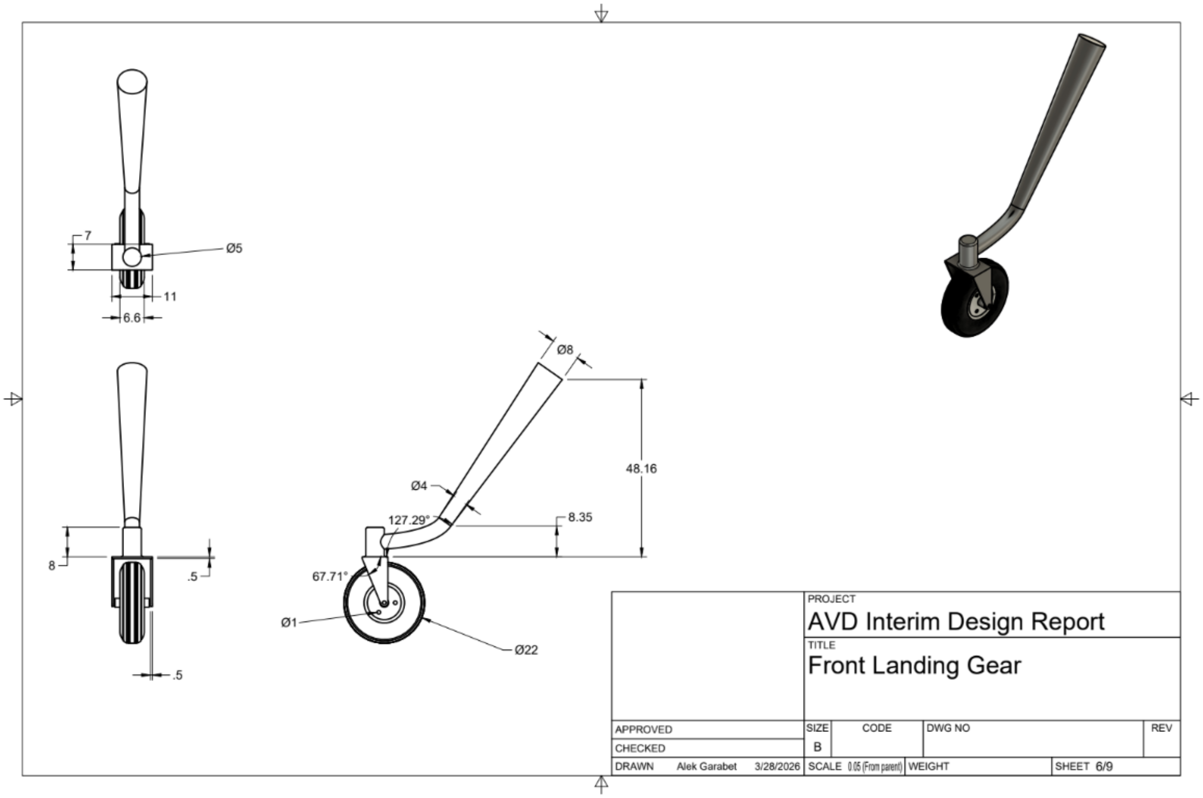

Figure 51. Rear Landing Gear CAD Drawing

4.7 Drawing #7

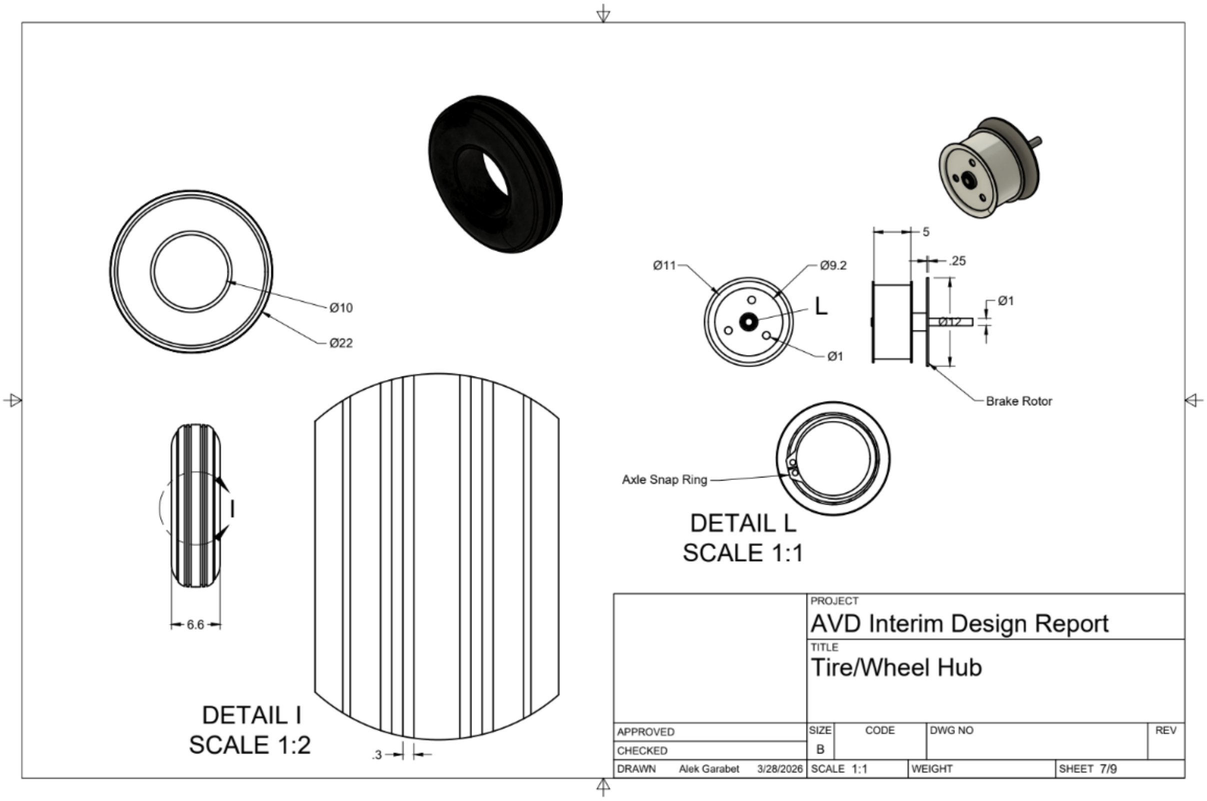

Figure 52. Landing Gear Tire/Hub CAD Drawing

4.8 Drawing #8

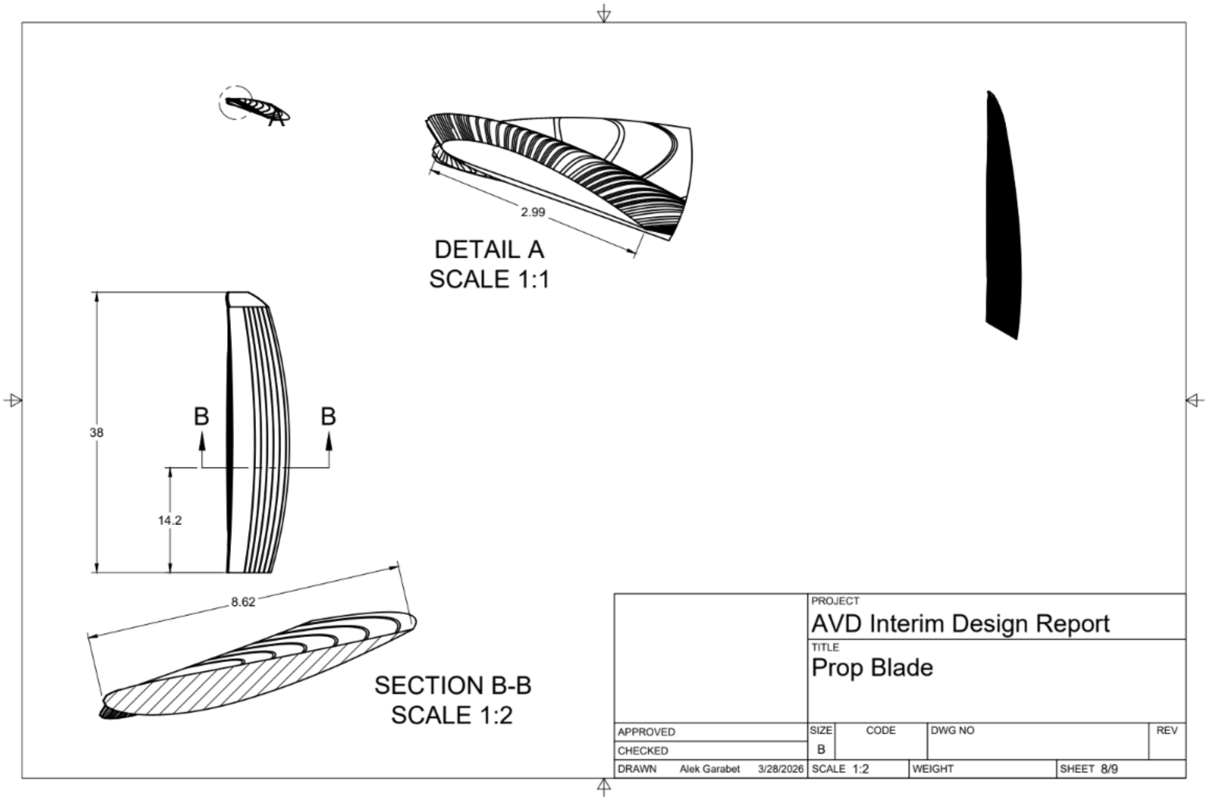

Figure 53. Propeller Blade CAD Drawing

4.9 Drawing #9

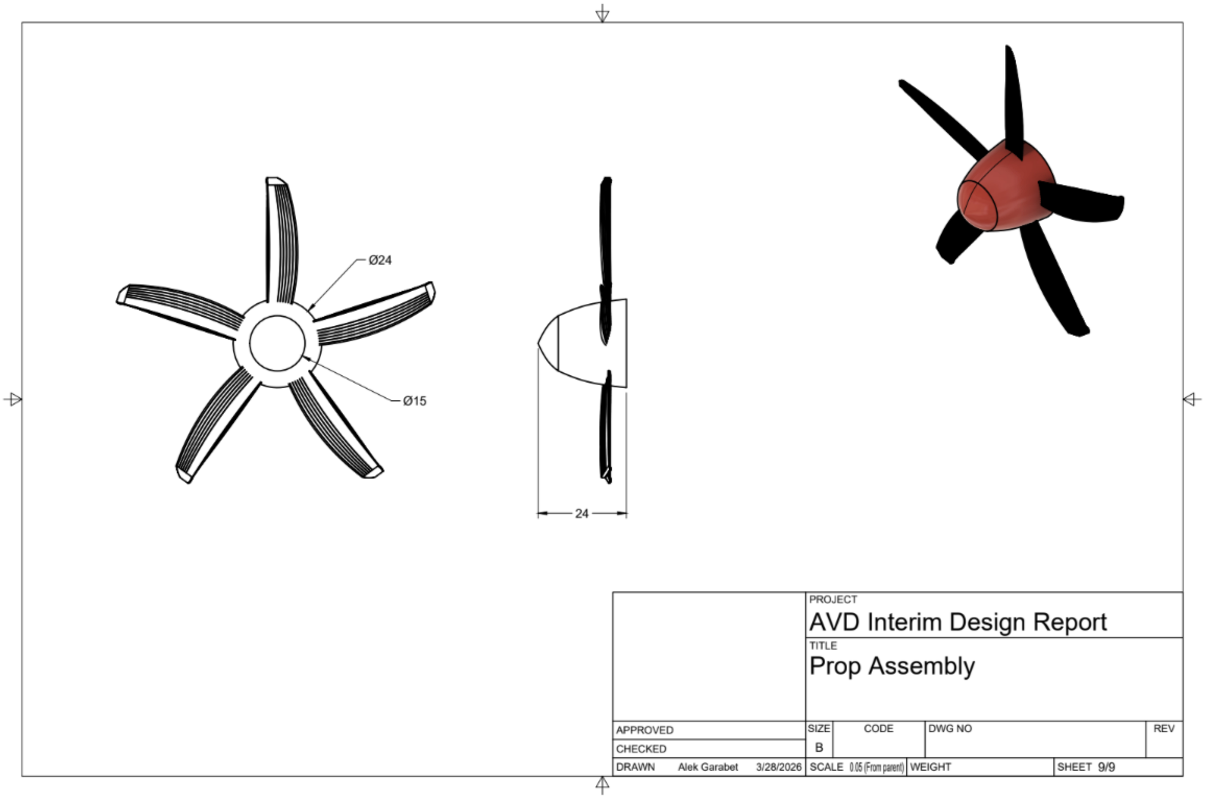

Figure 54. Propeller Assembly CAD Drawing

4.10 Performance estimation MATLAB

```
% ========================================================================
% Interim Design: Trade-Off Study & Sizing Script (5 Iterations)
% ========================================================================
clear; clc; close all;

%% 1. Input Parameters (Data extracted from FlightStream & OpenVSP)
config_names = {'Baseline V-Tail', 'Inverted V-Tail', 'Improved V-Tail', 'Canard Config', 'Y-Tail Config'};

% --- Aerodynamic & Weight Specs ---
W       = [3203.75, 3203.75, 3203.75, 3353.75, 3308.75]; % Takeoff Weight (lbs)
S       = [162.3, 162.3, 162.3, 162.3, 162.3];           % Main Wing Area (sq ft)
LD_max  = [26.0, 26.0, 26.0, 24.5, 26.0];                % Max Lift-to-Drag ratio
CL_max  = [1.4, 1.4, 1.4, 1.45, 1.4];                    % Max Lift Coefficient
AR      = [22.93, 22.93, 22.93, 22.93, 22.93];           % Aspect Ratio
e       = [0.85, 0.85, 0.86, 0.82, 0.84];                % Oswald Efficiency (Est)
CD0     = [0.024, 0.024, 0.023, 0.026, 0.025];           % Zero-lift drag (Parasite)

% --- Environmental & Regulatory Requirements ---
rho_SL  = 0.002377;                 % Air density at sea level (slugs/ft^3)
rho_30k = 0.000891;                 % Density at 30,000 ft (slugs/ft^3)
sigma   = rho_30k / rho_SL;         % Density ratio
g       = 32.17;                    % Gravity (ft/s^2)
S_to_req = 2000;                    % Required takeoff distance (ft)
V_climb_knots = 120;                % Target climb speed (knots)
mu_roll  = 0.04;                    % Rolling friction coefficient (tarmac)
mu_brake = 0.4;                     % Braking friction (dry tarmac)

% --- Engine Specs (Honeywell TPE331-10) ---
T_avail_SL_lbs = 5500 * 0.224809;   % Convert 5500 N to lbs (~1236.4 lbs)
T_avail_30k    = T_avail_SL_lbs * sigma; % Scaled available thrust at 30k ft

%% 2. Pre-allocate Output Arrays for the Table
num_configs = length(config_names);
T_loiter = zeros(1, num_configs);
T_takeoff = zeros(1, num_configs);
ROC_fpm  = zeros(1, num_configs);
S_land_total = zeros(1, num_configs);
V_max_knots = zeros(1, num_configs);

%% 3. Master Loop: Calculate Performance for Each Iteration
figure('Name', 'Trade Study: Thrust Req vs. Avail', 'Color', 'w', 'Position', [100, 100, 800, 600]);
hold on; grid on;
colors = {'b', 'c', 'g', 'r', 'm'};

for i = 1:num_configs
    % --- Loiter / Level Flight Minimum Thrust ---
    T_loiter(i) = W(i) / LD_max(i);

    % --- Takeoff Thrust Estimation ---
    V_stall = sqrt((2 * W(i)) / (rho_SL * S(i) * CL_max(i)));
    V_lof = 1.2 * V_stall;
    a_req = (V_lof^2) / (2 * S_to_req);
    F_accel = (W(i) / g) * a_req;
    V_avg = 0.7 * V_lof;
    q_avg = 0.5 * rho_SL * V_avg^2;
    CD_to = 0.04; % Parasite + gear/flap drag during roll
    D_avg = q_avg * S(i) * CD_to;
    L_avg = q_avg * S(i) * (CL_max(i) / 2);
    F_friction = mu_roll * (W(i) - L_avg);
```

```
    T_takeoff(i) = F_accel + D_avg + F_friction;

    % --- Rate of Climb (ROC) Estimation ---
    V_climb_fts = V_climb_knots * 1.68781;
    D_climb = W(i) / LD_max(i);
    ROC_fts = ((T_avail_SL_lbs - D_climb) * V_climb_fts) / W(i);
    ROC_fpm(i) = ROC_fts * 60;

    % --- Landing Distance Estimation ---
    V_td = 1.15 * V_stall;
    theta_app = deg2rad(3);
    S_air = 50 / tan(theta_app); % 50ft obstacle clearance
    V_avg_land = 0.7 * V_td;
    q_avg_land = 0.5 * rho_SL * V_avg_land^2;
    CD_land = 0.05; % Drag with deployed flaps/spoilers
    D_avg_land = q_avg_land * S(i) * CD_land;
    CL_land_roll = CL_max(i) / 2;
    L_avg_land = q_avg_land * S(i) * CL_land_roll;
    F_frict_land = mu_brake * (W(i) - L_avg_land);
    F_retard = D_avg_land + F_frict_land;
    a_land = (F_retard * g) / W(i);
    S_ground = (V_td^2) / (2 * a_land);
    S_land_total(i) = S_air + S_ground;

    % --- Maximum Cruise Speed (V_max) at 30,000 ft ---
    K = 1 / (pi * e(i) * AR(i));
    V_test_knots = 50:1:400;
    V_test_fts = V_test_knots * 1.68781;
    Drag_curve = zeros(size(V_test_fts));

    for j = 1:length(V_test_fts)
        V = V_test_fts(j);
        q = 0.5 * rho_30k * V^2;
        CL_req = W(i) / (q * S(i));
        CD_total = CD0(i) + K * CL_req^2;
        Drag_curve(j) = q * S(i) * CD_total;
    end

    [~, idx_vmax] = min(abs(Drag_curve - T_avail_30k));
    V_max_knots(i) = V_test_knots(idx_vmax);

    % Plot Drag Curve for this iteration
    plot(V_test_knots, Drag_curve, 'Color', colors{i}, 'LineWidth', 2, ...
         'DisplayName', sprintf('%s', config_names{i}));
end

% --- Finalize Plot ---
yline(T_avail_30k, 'k--', 'LineWidth', 2, 'DisplayName', 'Thrust Avail @ 30k ft');
title('Trade Study: Thrust Required vs. Thrust Available at 30,000 ft');
xlabel('True Airspeed (Knots)');
ylabel('Thrust / Drag (lbs)');
legend('Location', 'SouthEast');
ylim([0, max(T_avail_30k)*1.5]);

%% 4. Generate the Rubric-Required Output Table
fprintf('\n=========================================================================================================\n');
fprintf('                           SECTION 3.3 SIZING & PERFORMANCE ESTIMATION TABLE \n');
fprintf('=========================================================================================================\n');
```

```
fprintf('%-25s | %-12s | %-12s | %-12s | %-12s | %-12s\n', 'Parameter', config_names{1}, config_names{2}, config_names{3}, config_names{4}, config_names{5});
fprintf('-----------------------------------------------------------------------------------------------------------\n');
fprintf('%-25s | %-12.2f | %-12.2f | %-12.2f | %-12.2f | %-12.2f\n', 'Weight (lbs)', W(1), W(2), W(3), W(4), W(5));
fprintf('%-25s | %-12.2f | %-12.2f | %-12.2f | %-12.2f | %-12.2f\n', 'Max L/D', LD_max(1), LD_max(2), LD_max(3), LD_max(4), LD_max(5));
fprintf('%-25s | %-12.3f | %-12.3f | %-12.3f | %-12.3f | %-12.3f\n', 'CD0 (Parasite Drag)', CD0(1), CD0(2), CD0(3), CD0(4), CD0(5));
fprintf('%-25s | %-12.1f | %-12.1f | %-12.1f | %-12.1f | %-12.1f\n', 'Min Loiter Thrust (lbs)', T_loiter(1), T_loiter(2), T_loiter(3), T_loiter(4), T_loiter(5));
fprintf('%-25s | %-12.1f | %-12.1f | %-12.1f | %-12.1f | %-12.1f\n', 'Takeoff Thrust Req (lbs)', T_takeoff(1), T_takeoff(2), T_takeoff(3), T_takeoff(4), T_takeoff(5));
fprintf('%-25s | %-12.0f | %-12.0f | %-12.0f | %-12.0f | %-12.0f\n', 'Rate of Climb (ft/min)', ROC_fpm(1), ROC_fpm(2), ROC_fpm(3), ROC_fpm(4), ROC_fpm(5));
fprintf('%-25s | %-12.0f | %-12.0f | %-12.0f | %-12.0f | %-12.0f\n', 'Total Landing Dist (ft)', S_land_total(1), S_land_total(2), S_land_total(3), S_land_total(4), S_land_total(5));
fprintf('%-25s | %-12.0f | %-12.0f | %-12.0f | %-12.0f | %-12.0f\n', 'Max Cruise Spd (knots)', V_max_knots(1), V_max_knots(2), V_max_knots(3), V_max_knots(4), V_max_knots(5));
fprintf('===========================================================================================================\n');
```

CHAPTER III – FINAL DESIGN REPORT

1.0 Design and Regulatory Requirements

Table 33: Design Requirements Table

Design Standard / Parameter	Target Constraint	Current Value (Improved V-Tail)	Status
Total Mission Range	≥750 miles	8,977 miles	Pass
System Range	≥1,125 nmi	7,801 nmi	Pass
Payload Capacity	Suitcase-sized EO/IR	1,000 lbs (Lynx Radar + WESCAM)	Pass
Electrical Power	12 VDC for 8 hours	Tattu 6S 16000mAh LiPo Battery	Pass
Takeoff Distance	≤2,345 ft	≤2,000 ft	Pass
Landing Distance	≤2,250 ft	1,934.1 ft	Pass
MTOW	Support fuel, payload, margins	6,017 lb	Pass
Max Cruise Speed	≤370 knots	305 knots	Pass
Never-Exceed Speed	285 kn IAS / Mach 0.64	466 knots (Structural Limit)	Pass
Rate of Climb (ROC)	≥3,424 ft/min	3920.2 ft/min	Pass
Operational Ceiling	41,001 ft service ceiling	45,000 ft (Operates at 30,000 ft)	Pass

1.1 Calculation Methodologies

The performance capabilities demonstrating that these standards are reached were evaluated using the following mathematical formulations:

Range and Endurance

Mission ranges heavily exceed the minimums, validated using the Breguet Range Formula:

(11)

Given the Improved V-Tail's maximum aerodynamic efficiency $\left(\frac{L}{D_{max}} = 26\right)$ and the 210 gallon JP-8 fuel capacity , the aircraft easily satisfies the 1,125 nmi baseline.

Minimum Loiter Thrust

The minimum thrust required to sustain level flight during the 30,000 ft ISR orbit assumes peak aerodynamic efficiency is depicted in the equation below

(12)

Using the thrust required for loiter becomes 123.2 lbs. confirming the Honeywell TPE331-10 turboprop can comfortably sustain the 8-hour orbit at part-load efficiency.

Takeoff Distance Sizing

Takeoff thrust was explicitly sized to overcome inertial acceleration and aerodynamic drag while satisfying a strict 2,000 ft runway constraint (which inherently satisfies the 2,345 ft client requirement).

Rate of Climb

The climbing capability was evaluated at a target climb speed (V_{climb}) of 120 knots utilizing the specific excess power method:

(13)

Where T_{avail} is the sea-level thrust of the engine and D is aerodynamic drag.

Landing Distance

The landing total integrates the airborne approach (a 3-degree glideslope to clear a 50 ft obstacle) and the ground roll. Ground deceleration factored in mechanical braking friction. Deploying aerodynamic drag, yielding at 1,934.1ft. Much less than the 2,250 ft threshold.

Maximum Cruise Speed

To verify the aircraft remains under the 370-knot maximum cruise limit , the sea-level engine thrust was scaled to 30,000 ft using the atmospheric density ratio $\left(\sigma = \frac{\rho_{30k}}{\rho_{SL}}\right)$. The total drag was modeled using the standard polar:

(14)

V_{max} is identified as the 305-knot intersection where thrust (D) meets the scaled available engine thrust.

Table 34: Standards Table

Standard Name	Requirement Definition	Current Value (Angel One)	Status
FAA 14 CFR Part 23	Ultimate loads (Limit loads × 1.5 FS) for structural safety.	Fails at 5.7g ultimate load (exceeds yield strength & high deformation in FEA).	Fail
FAA 14 CFR Part 25	Crosswind ≥20 kts or 0.2VSR0 (whichever is greater).	20 kts governs (0.2×64.4 kts stall speed = 12.88 kts).	Pass
EASA CS-23/25	Landing distance ≤1.68× demonstrated; Min. climb gradient 2.4%.	Landing margin: 3,780 ft; Climb gradient: 26.29%.	Pass
EASA SC-LUAS	Catastrophic failure probability ≤10−9/hr.	Mitigated via composite structural redundancy.	Pass
MIL-STD-1797	Maneuver limit load factors of +3.8g / -1.5g.	Max load factor 1.4g (FEA shows high local stress/failure at 3.8g).	Fail
MIL-STD-810	Temp range −60∘F to 140∘F; 200-cycle salt/fog exposure.	Operable at temp range; Carbon fiber resists salt/fog corrosion.	Pass
STANAG 4671	Failures ≤10−6/hr; Descent Vy <4.4(W/S)1/6.	Vy =2.56 m/s (Well below 7.3 m/s limit).	Pass
STANAG 4671	C2 link, Comm system, Ground Control Station (GCS).	Honeywell H-764 ACE & L3Harris SATCOM.	Pass
STANAG 4586	Level 5 Interoperability (Full	Honeywell H-764 ACE.	Pass

	control, launch & recovery).		
NATO Interop.	Max control delay (latency) ≤200 ms.	Honeywell H-764 ACE architecture.	Pass
RTCA DO-160	Survival −55∘C to +85∘C; Max Altitude: 55,000 ft.	Avionics rated for 55,000 ft (Aircraft ceiling is 45,000 ft).	Pass
RTCA DO-160	Isolated mounts, voltage regulation, sealed bays.	Composite airframe with sealed avionics bays.	Pass
RTCA DO-178C	Software verified to Level A (Catastrophic) or Level B (Hazardous).	Honeywell adaptive flight control software protocols.	Pass

Evaluation and Calculation Explanations

Structural Load Limits (FAA 14 CFR Part 23 & MIL-STD-1797)

The structural standards require the aircraft to withstand a limit load of +3.8g and an ultimate load of +5.7g (1.5 * limit load factor). To verify this, a Finite Element Analysis (FEA) was performed in Simcenter Nastran. Assuming a 6,000 lbf MTOW, a 1g half-wing lift load equates to 3,000 lbf, scaling up to 17,100 lbf for the 5.7g ultimate case.

- Result: Both the Aluminum 7075-T6 and the higher-modulus MJ40 Carbon Fiber spar cap configurations suffered from excessive deflection and localized stresses near the root and chord-transition regions that exceeded material yield strengths. The wing structure does not currently provide efficient bending stiffness for the maneuver loads and requires a geometry and reinforcement redesign.
- Potential Improvements: Several potential fixes have been considered, however limited in the name of time. These potential improvements include altered spar geometry on the wings could reduce load, adding additional local paths or reinforcements, and improved skin participation.

Crosswind Takeoff / Landing (FAA 14 CFR Part 25)

The standard dictates the aircraft must establish a safe 90-degree crosswind takeoff and landing parameter for dry runways of at least 20 knots, or 20% of the reference stall speed $(0.2V_{SR0})$.

- Calculation: The reference stall speed (V_{SR0}) is 64.4 knots. $0.2 \cdot 64.4 = 12.88$ knots. Because 20 knots is greater than 12.88 knots, the strict 20-knot standard governs the metric, which the aircraft safely targets.

Landing Margins and Climb Gradient (EASA CS-23/25)

EASA requires the operational landing distance to possess a 1.68x safety multiplier over the physically demonstrated landing distance, alongside a minimum climb gradient of 2.4% for obstacle clearance.

- Calculation: For a required 2,250 ft distance constraint, multiplying by EASA's 1.68 factor demands a runway availability footprint of 3,780 ft (safely under the 5,000 ft client-provided runway minimum). The +4,000 ft/min rate of climb easily clears the 2.4% gradient baseline, hitting 26.29%.

Descent Velocity Limit (STANAG 4671)

NATO limits the maximum descent velocity during the landing gear drop phase using the wing loading formula:

$$V_{Limit} = 4.4 \cdot \left(\frac{W}{S}\right)^{\frac{1}{6}} \tag{14}$$

- Calculation: Utilizing the aircraft's specified wing loading, the regulatory maximum allowable descent speed evaluates to 7.3 m/s. The UAV's actual controlled descent speed (V_y) is tracked at 2.56 m/s, successfully passing the standard.

2.0 Technology Availability

All technologies selected for the final aerial system design were evaluated based on their Technology Readiness Level (TRL) to ensure that the system is both feasible and realistically implementable. The goal of this assessment was to avoid conceptual or experimental components and instead rely on proven, flight-tested systems that reduce development risk and improve overall system reliability. Apart from the optics package provided by Siemens, all major subsystems are classified at TRL 9.

The propulsion system selected is the Honeywell TPE331-10 turboprop engine, which is a widely used and well-documented engine in UAV and small aircraft applications. This engine is classified as TRL 9 because it has extensive operational history, proven reliability, and established maintenance practices. Its performance characteristics support compliance with FAA Part 23/25 and EASA CS-23/25 requirements by enabling safe takeoff and landing performance, sufficient climb capability, and efficient cruise operation. These characteristics directly contribute to meeting safety margins and overall flight performance requirements.

The flight control system is based on the Honeywell H-764 ACE flight computer, which is also a TRL 9 system. This system provides reliable navigation, guidance, and control capabilities and enables autonomous and semi-autonomous operation. It plays a key role in satisfying NATO STANAG 4671 requirements for UAV control systems and contributes to compliance with DO-178C standards for software safety and reliability. The system ensures stable flight behavior and proper handling under various flight conditions.

The radar system selected is the Lynx Multi-Mode Radar developed by General Atomics. This system is also classified as TRL 9 due to its operational use on platforms such as the MQ-9 Reaper. It supports mission requirements for sensing and surveillance while operating within environmental conditions defined by MIL-STD-810. Its proven use in harsh environments demonstrates compliance with durability and operational reliability standards.

The communication system utilizes an L3Harris Ku-band SATCOM antenna, which enables beyond line-of-sight communication. This technology is also at TRL 9 and ensures continuous connectivity between the UAV and ground control. It directly supports NATO STANAG 4586 requirements for UAV communication and interoperability, allowing reliable command, control, and data transmission during mission operations.

The onboard power system includes a Tattu 6S 16000mAh LiPo battery, which is classified as TRL 9 due to its widespread use in UAV systems. This system provides consistent and reliable electrical power to avionics and mission systems. It supports compliance with DO-160 standards by ensuring stable operation under varying environmental and electrical conditions, including vibration and temperature effects.

The landing gear system consists of a fixed tricycle configuration using aluminum, composite materials, and oleo struts. This design is also TRL 9 and aligns with FAA and EASA structural safety requirements. It is designed to handle operational loads within the limits defined by MIL-STD-1797, including load factors of +3.8g and -1.5g. The simplicity of the fixed gear also improves reliability and reduces maintenance complexity.

The optics package provided by Siemens is assumed to be a mature subsystem and serves as the primary mission payload. It fulfills core mission requirements related to sensing and data acquisition and is expected to meet environmental and operational standards similar to MIL-STD-810 and DO-160 for durability and performance.

All selected technologies work together as a fully integrated system. The propulsion system enables long duration flight, while the flight computer coordinates all control and mission operations. The radar and optics systems collect mission-critical data, which is processed onboard and transmitted through the SATCOM system in real time. The power system ensures uninterrupted operation of all subsystems, and the structural components provide a stable platform for accurate sensing and control.

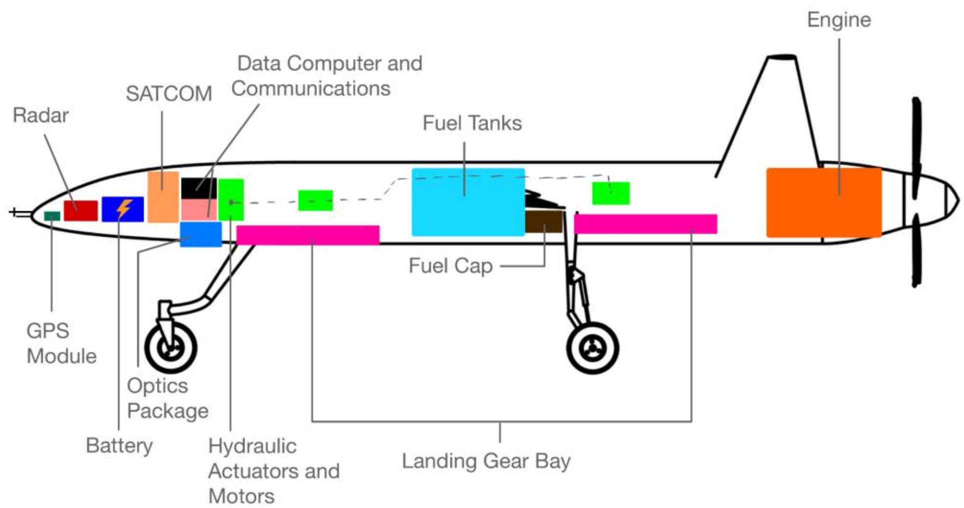

Figure 55. Technology & System Assembly Layout

Figure 55 illustrates the layout of important subsystems and where they are in relation to each other. At the nose of the UAV, most of the avionics and flight computers are tightly packed. Moving down the fuselage of the UAV, the more mechanical subsystems are neatly integrated into the design. At the end of the UAV, right before the propeller, the engine is seated at the rear. This location was optimal for maintenance access.

Overall, the selected technologies not only meet performance-based Siemens requirements such as endurance, autonomy, sensing capability, and communication, but also align with major regulatory and industry standards including FAA Part 23/25, EASA CS-23/25, MIL-STD-1797/810, NATO STANAG 4671/4586, and DO-160/178C. The use of high TRL components ensures that these requirements can be met with minimal technical risk, resulting in a design that is both feasible and compliant with real-world aerospace standards.

3.0 Design Iterations and Refinement

3.1 High Fidelity Analysis

3.11 Aerodynamic Performance Analysis (CFD)

The aerodynamic performance of our final configuration was evaluated using a steady state CFD simulation conducted at a freestream velocity of 130 m/s. The solution ran 1000 iterations to ensure convergence of the flow field and force coefficients.

The pressure contour plots (Figures 55, 56, 57, 58) illustrate the distribution of static pressure on the aircraft surface. As expected, a clear pressure differential is seen between the upper and lower surfaces of the wing. The lower surface shows higher pressure, while the upper surface has lower pressure, showing the generation of lift. Inspection of the wing in Figure 56 shows a smooth pressure gradient from the leading to trailing edges indicating the flow stays attached with no major separation. The V tail configuration also has a relatively uniform pressure distribution, with no large pressure concentrations meaning the geometry does not add any major adverse effects.

The force plots (Figures 59, 60) show the forces over the simulation time. At the beginning both force and drag both have transient oscillations while the solver stabilizes from the initial conditions. These oscillations quickly decay, and the solutions converge to steady values within the first 300 iterations. The drag force stabilizes around –1859N, and the lift stabilizes around 53402N.

At a velocity of 130 m/s, the flow stays attached to the lifting surfaces as seen by the smooth gradients. This suggests that the aircraft is operating well below the stall condition. The magnitude of the lift force is much greater than the drag, which is expected for this highly efficient aircraft. The lift to drag ratio from these results shows favorable aerodynamic performance.

The use of 1000 iterations allowed for convergence as seen when the forces stabilize, however some improvements could include mesh independence study to ensure solution accuracy, sensitive analysis on turbulence models, and validation against analytical or experimental data.

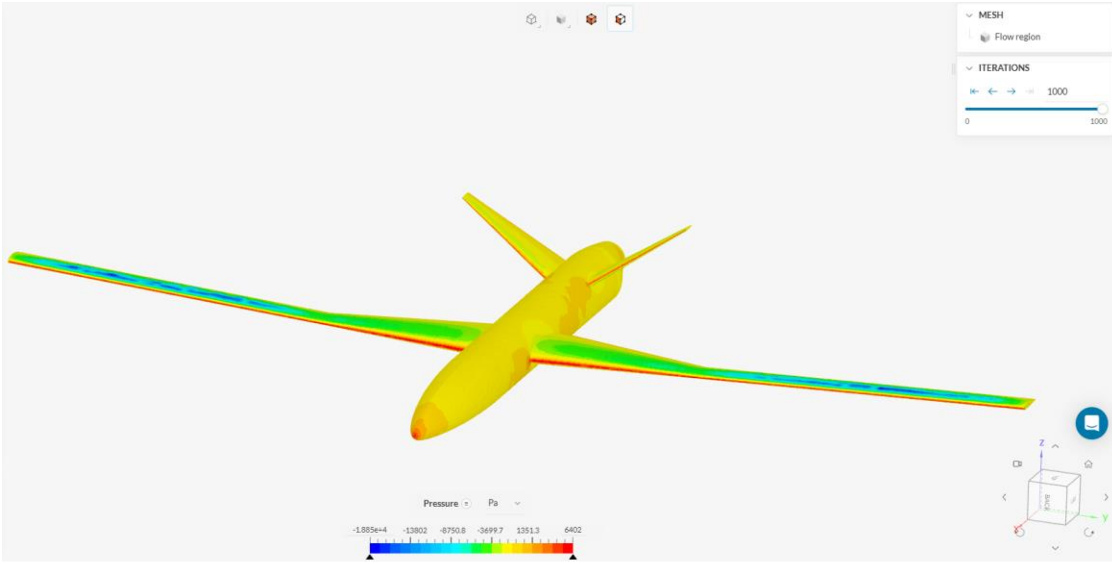

Figure 55. Regular V-Tail Pressure Contour

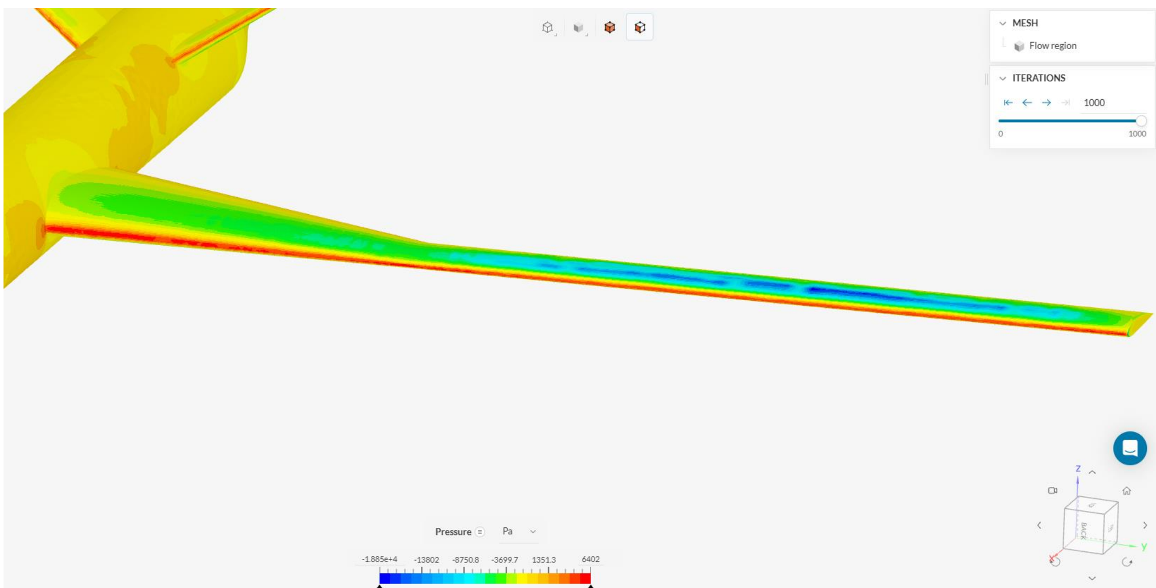

Figure 56. Regular V-Tail Close-up Wing Pressure Contour

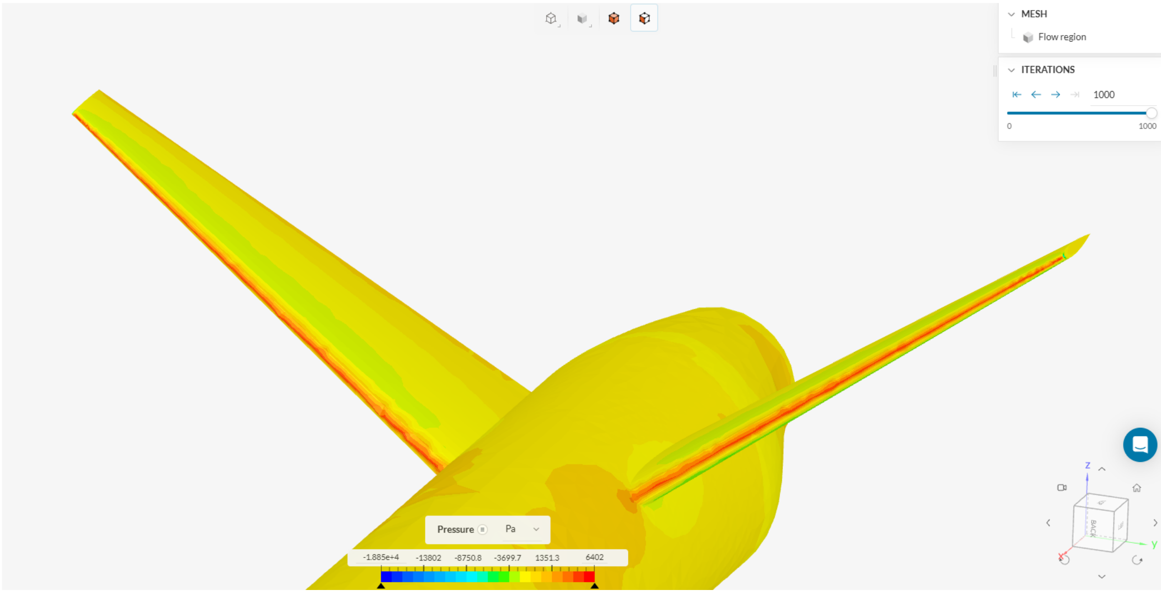

Figure 57. Regular V-Tail Close-up Tail Pressure Contour

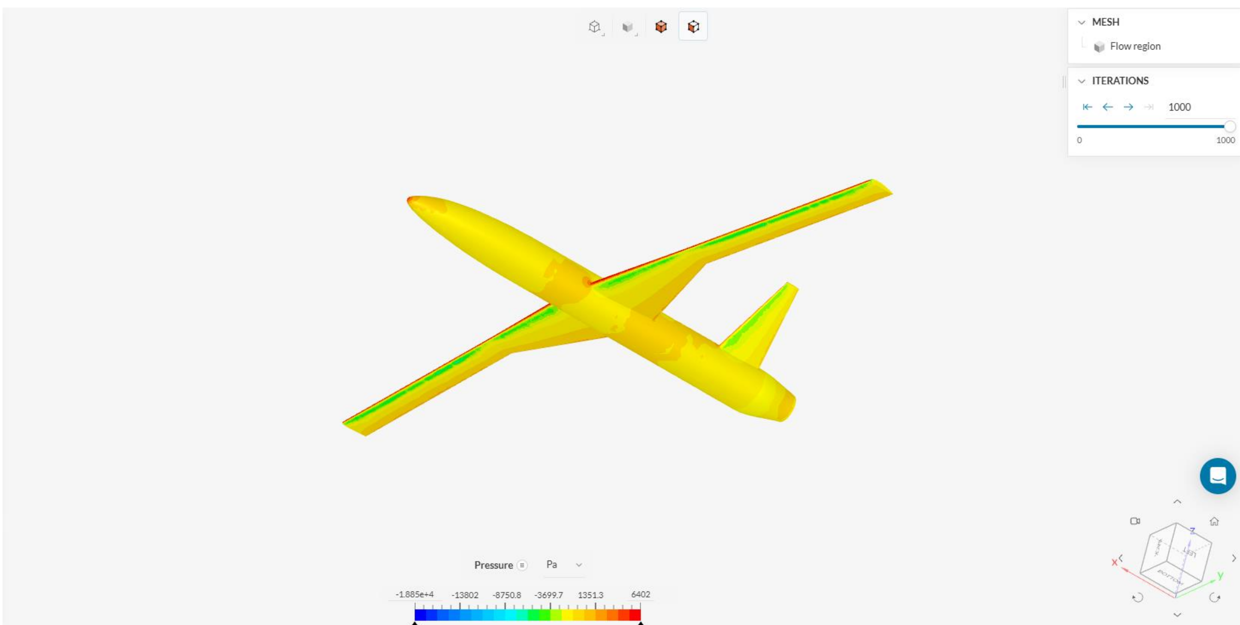

Figure 58. Underside of Aircraft Pressure Contour

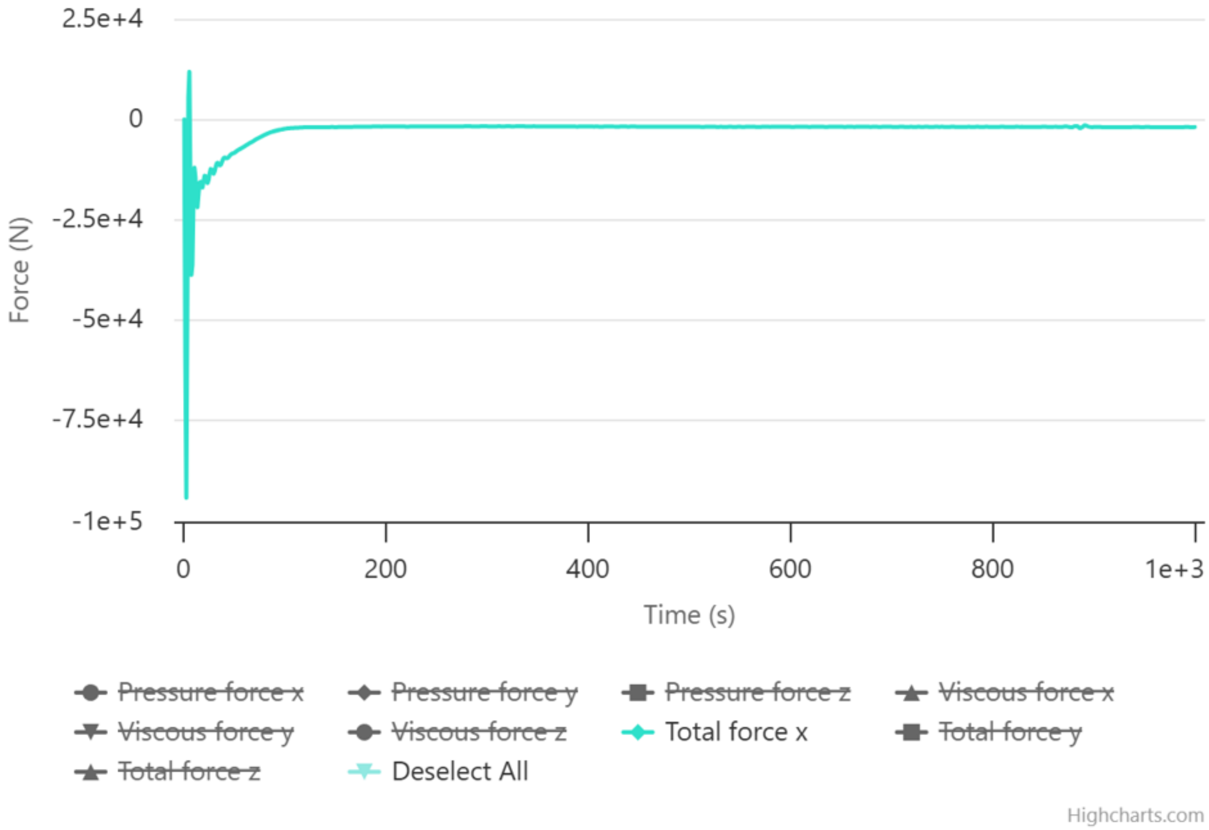

Figure 59. Drag Plot Stabilizes at Approximately 1859 N

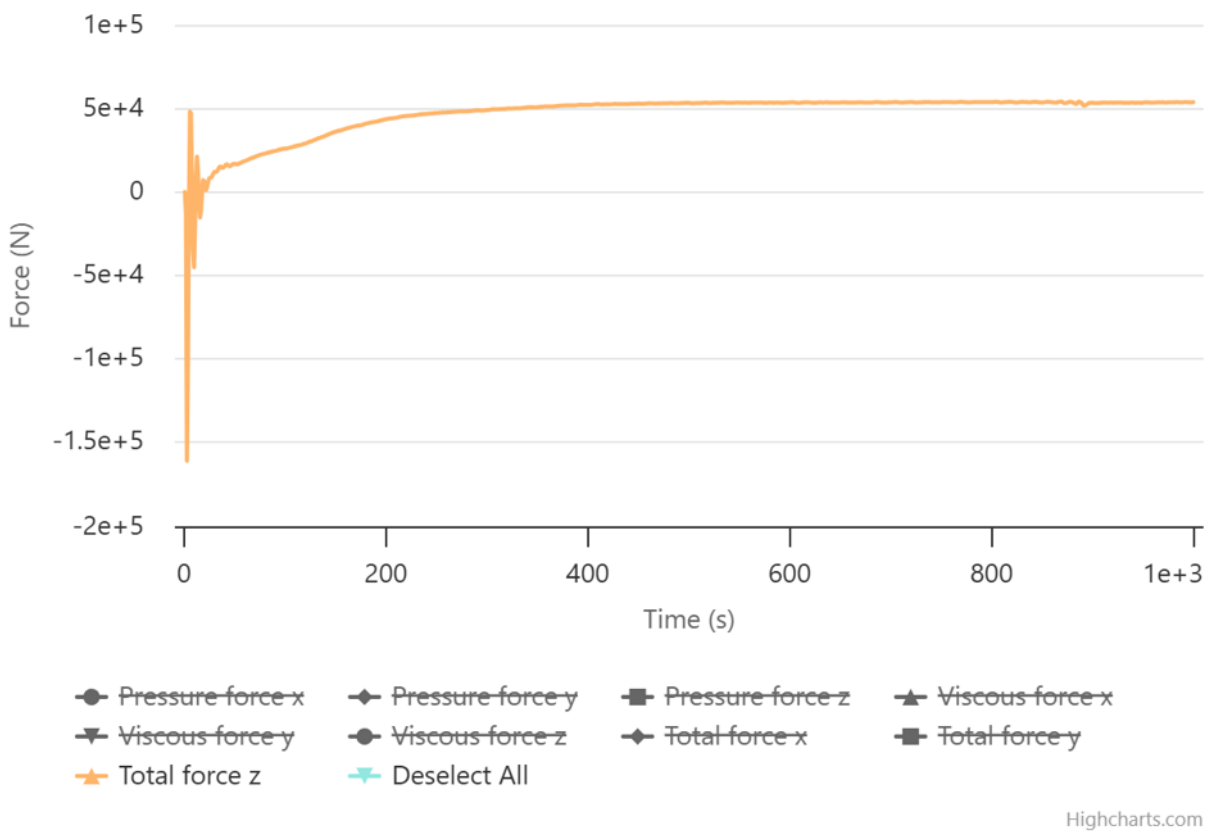

Figure 60. Lift Plot Stabilizes at Approximately 53402 N

3.12 Structures Analysis (FEA)

A structural analysis was performed to evaluate whether the UAV wing design could satisfy the required maneuver load cases for a Medium-Altitude Long-Endurance UAV. The analysis focused on the 3.8g limit-load case and the 5.7g ultimate-load case. The 5.7g case was taken as 1.5 times the 3.8g limit load, which is consistent with the typical relationship between limit load and ultimate load used in airworthiness structural design. MIL-HDBK-516 identifies airworthiness certification criteria for both manned and unmanned fixed-wing air systems, and states that the handbook is used by the service airworthiness authority to define an airworthiness certification basis. STANAG 4671 is also relevant because it provides UAV airworthiness requirements for NATO military UAV systems, especially fixed-wing UAVs in the 150 kg to 20,000 kg maximum takeoff weight class.

For this project, the wing was modeled in FEMAP and solved using Simcenter Nastran. The finite element model included the external skin, ribs, spars, spar webs, and spar caps. A four-noded quadrilateral-dominated shell mesh was used because the wing is primarily a thin-walled aerospace structure. The ribs, spar webs, and spar caps were meshed with an average element size of 0.25 in, while the skin was meshed with an average element size of 0.5 in to reduce computational cost. The spar webs were modeled with a thickness of 0.063 in, the spar caps with a thickness of 0.5 in, the ribs with a thickness of 0.125 in, and the skin with a thickness of 0.08 in. These values were selected to create a relatively stiff preliminary wing structure while remaining practical for a course-level shell model.

Two material configurations were evaluated. The baseline configuration used Aluminum 7075-T6 throughout the structure, including the spar caps. This material was selected because it is a common high-strength aerospace aluminum alloy. A second configuration replaced the aluminum spar caps with an equivalent high-modulus carbon-fiber material. The carbon-fiber case was not intended to represent a final composite laminate design. Instead, it was used as a simplified stiffness comparison to determine whether increasing spar cap stiffness could reduce wing deflection and improve the structural response.

Table 35: Material Properties for Finite Element Analysis

Property	Symbol	Aluminum 7075-T6	Equivalent Carbon Spar Cap
Young's modulus	E	10.4 Msi	42.7 Msi
Poisson's ratio	ν	0.33	0.25
Shear modulus	G	3.91 Msi	16 Msi
Density	ρ	0.101 lb/in^3	0.060 lb/in^3
Yield strength	σ_y	73 ksi	N/A
Ultimate tensile strength	σ_u	83 ksi	Laminate-dependent

The applied loads were based on an aircraft with a maximum takeoff weight of 6000 lbf. Since the model represented one half of a symmetric aircraft, each half-wing was assumed to carry half of the total lift. This resulted in a 1g half-wing load of 3000 lbf, a 3.8g limit load of 11,400 lbf, and a 5.7g ultimate load of 17,100 lbf. These cases were treated as structural maneuver load cases rather than literal takeoff or cruise conditions. This is important because the purpose of the 3.8g and 5.7g cases was to check structural strength and stiffness against airworthiness-style load requirements, not to represent a specific aerodynamic condition at one angle of attack.

Finite Element Results: Aluminum 7075-T6 Spar Cap Case

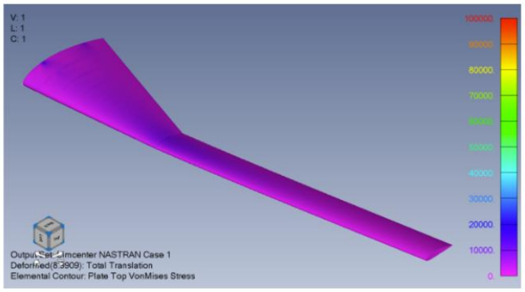

(a) Isometric view.

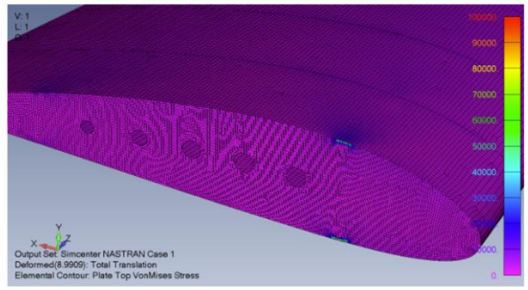

(b) Root and chord-transition view.

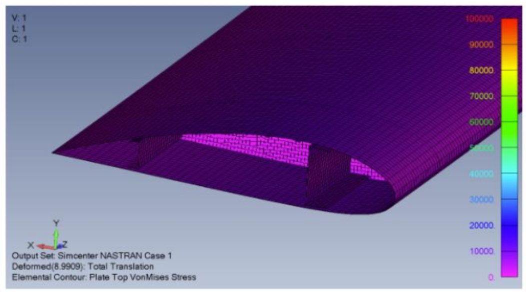

(c) Section view near the chord-transition region.

Figure 61. Aluminum 7075-T6 1g Loading Case

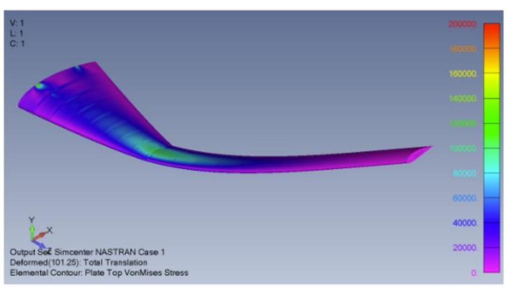

(a) Isometric view.

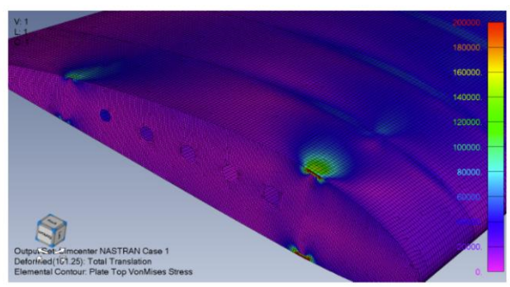

(b) Root and chord-transition view.

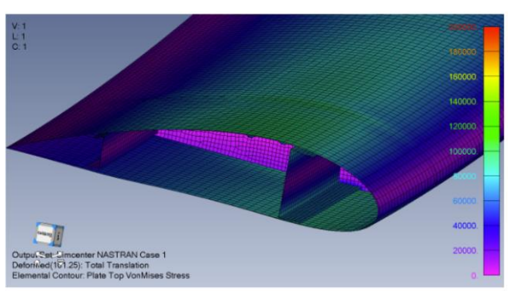

(c) Section view near the chord-transition region.

Figure 62. Aluminum 7075-T6 3.8g Loading Case

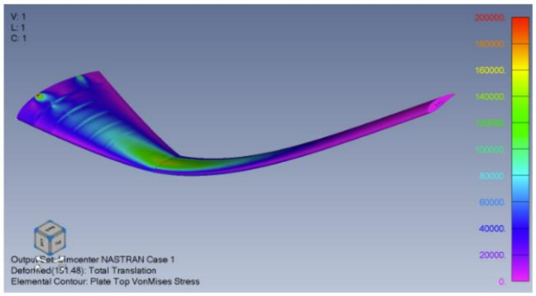

(a) Isometric view.

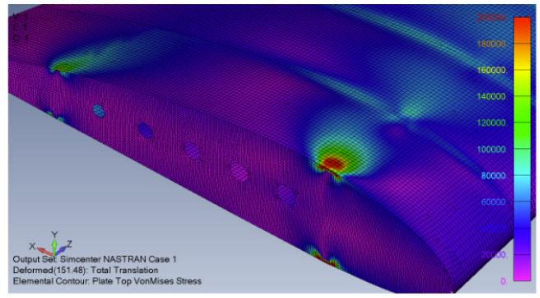

(b) Root and chord-transition view.

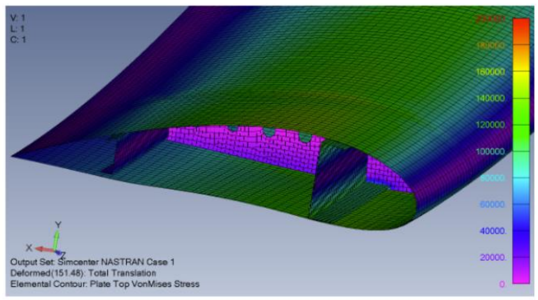

(c) Section view near the chord-transition region.

Figure 63**. Aluminum 7075-T6 5.7g Loading Case**

The aluminum spar cap configuration did not meet the expected structural requirements for higher load cases. In the 3.8 g limit-load case, the model predicted large wing deflection and stresses above the yield strength of Aluminum 7075-T6 in critical regions near the root, spar caps, and chord-transition area. For a metallic structure, the limit-load condition should be sustained without significant permanent deformation. Since the aluminum stress results exceeded the approximate 73 ksi yield strength in several areas, the structure would likely experience yielding and would not be acceptable without redesigning. In the 5.7g ultimate-load case, the stress increased further and exceeded acceptable levels by an even larger margin. This indicates that the current aluminum configuration would not satisfy the intended strength requirements for either the 3.8g limit case or the 5.7g ultimate case.

Finite Element Results: MJ40 Carbon Fiber Spar Cap Case

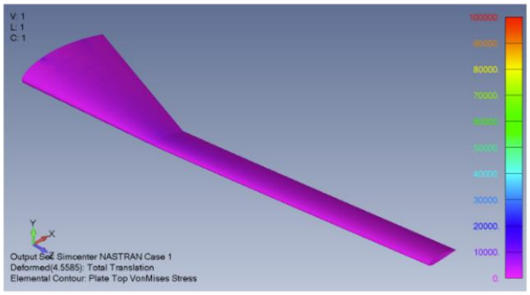

(a) Isometric view.

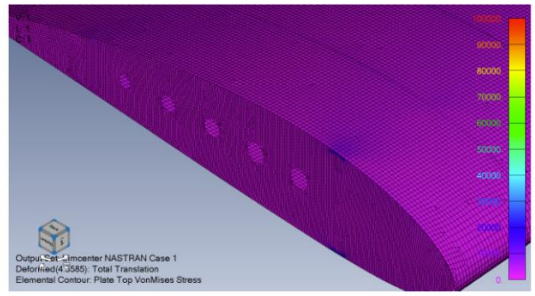

(b) Root and chord-transition view.

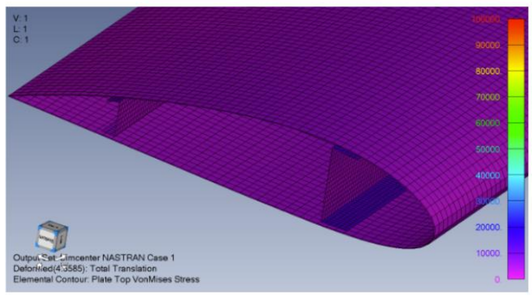

(c) Section view near the chord-transition region.

Figure 64. MJ40 Carbon Fiber 1g Loading Case

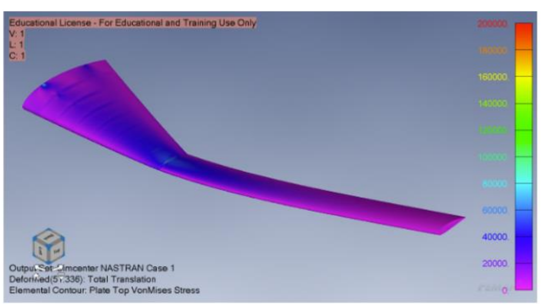

(a) Isometric view.

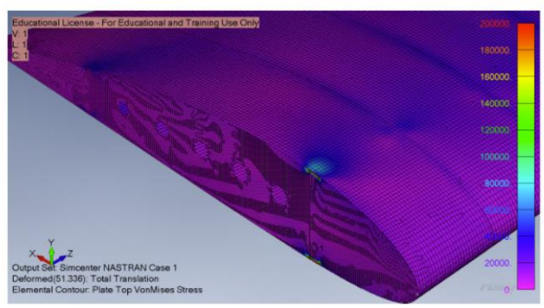

(b) Root and chord-transition view.

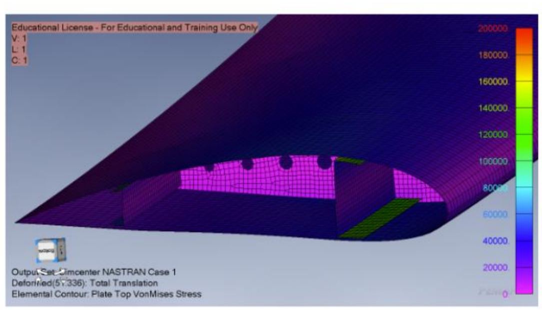

(c) Section view near the chord-transition region.

Figure 65. MJ40 Carbon Fiber 3.8g Loading Case

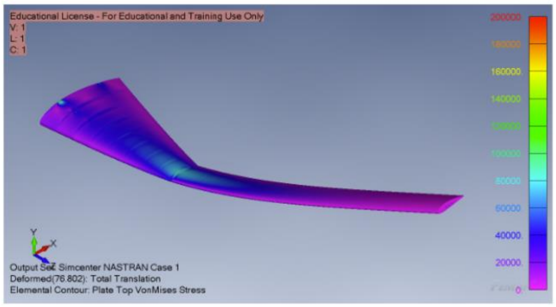

(a) Isometric view.

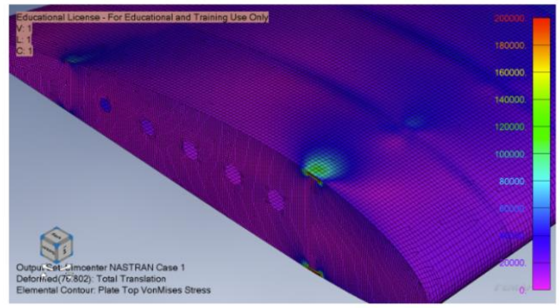

(b) Root and chord-transition view.

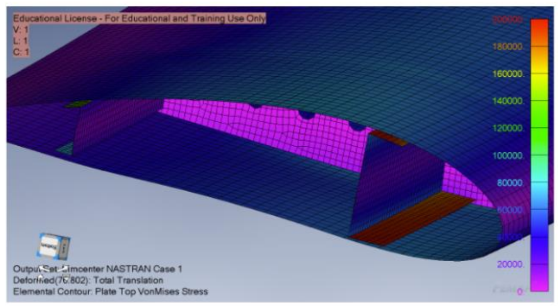

(c) Section view near the chord-transition region.

Figure 66. MJ40 Carbon Fiber 5.7g Loading Case

The carbon-fiber spar cap configuration improved the stiffness of the wing and reduced the predicted deflection compared with the aluminum spar cap case. This confirmed that the spar caps are a major contributor to the global bending stiffness of the wing. However, even with the higher-modulus carbon-fiber spar caps, the model still showed large deformation and high local stresses near the root and chord-transition region. The 3.8g case showed possible local failure or unacceptable stress concentrations, and the 5.7g case showed even more severe deformation and likely failure regions. Because the carbon-fiber material was modeled as an equivalent isotropic stiffness material rather than as a true composite laminate, the stress results cannot be treated as final composite failure predictions. A real composite design would require ply level properties, fiber directions, stacking sequence, compression, tension, and shear allowables, and a composite failure criterion.

The main reason the standards were not met is that the current wing structure does not provide enough efficient bending stiffness or strength for the required maneuver loads. The wing has a high aspect ratio and a long semispan, which creates a large bending moment at the root. The chord transition also creates a sudden change in local stiffness and load path, causing stresses to concentrate near that region. Although the spar caps were made relatively thick, simply increasing thickness is not an efficient solution once the overall wing-box layout is not carrying load effectively. The results suggest that the wing needs a more refined structural arrangement, not just heavier components.

Another reason for the poor compliance result is that the model used a preliminary structural layout. The skin, ribs, spars, spar webs, and spar caps were connected using practical modeling assumptions suitable for the time available, but these assumptions introduce uncertainty in the load transfer between components. Glued shell connections are useful for assembling a model quickly, but they may not accurately represent the behavior of a fully integrated wing box under large deflection. The model also did not include a full nonlinear material response. For aluminum, stresses above yield were reported as linear elastic stresses, meaning the model did not simulate plastic deformation or stress redistribution. For the carbon fiber case, the model did not include laminate failure. Therefore, the results are best interpreted as a preliminary indication that the structure is overstressed, rather than a final certification-level failure prediction.

Additional refinement would be needed before the wing could be considered compliant with MIL-HDBK-516 or STANAG 4671-style structural expectations. Future work should include a mesh convergence study, improved structural connectivity between the skin and internal wing-box members, a better stiffness transition near the chord break, refined aerodynamic pressure loading, and a more realistic composite spar cap definition if carbon fiber is used. The spar cap geometry and placement should also be redesigned to increase bending stiffness more efficiently. Additional load paths, local reinforcement near the root and chord-transition region, and improved skin participation in bending would likely be required.

Overall, the analysis showed that the current wing concept is not yet structurally compliant under the 3.8g limit-load and 5.7g ultimate-load cases. The aluminum configuration exceeded yield limits and produced excessive deflection, while the carbon-fiber spar cap configuration improved stiffness but still showed unacceptable deformation and local stress concerns. These results do not mean the UAV concept is infeasible, but they do show that the wing structure is still preliminary and would require further optimization, higher-fidelity modeling, and additional design refinement before it could satisfy MIL/STANAG airworthiness-style structural requirements.

Finally, a simplified analytical model was also developed to provide a basic check against the finite element results. The wing was idealized as a cantilever beam fixed at the root and loaded by an upward distributed lift load. This approach follows the general tapered wing beam analysis described by Megson, where changes in spar depth and spar cap spacing strongly affect the bending stiffness of a tapered wing structure. The model did not attempt to capture every detail of the FEMAP model, such as rib flexibility, skin deformation, glued shell connections, torsion, local stress concentrations, or the chord-transition geometry. Instead, it was used to estimate whether the finite element deflections were within a reasonable order of magnitude.

The analytical model treated the wing as a piecewise tapered beam. The inboard section tapered from the 6 ft root chord to the 2 ft outboard chord, while the outboard section remained constant at the 2 ft chord. The spar cap separation was therefore largest near the root and much smaller in the outboard section. Since wing bending stiffness depends strongly on spar cap separation, this reduction in wing-box depth had a large effect on the predicted deflection. This is consistent with tapered beam theory, where the spanwise variation in section geometry changes the local area moment of inertia and therefore the bending response.

The analytical results showed the same overall trend as the finite element model. The aluminum spar cap case produced much larger deflections than the carbon-fiber spar cap case because Aluminum 7075-T6 has a much lower elastic modulus than the equivalent carbon-fiber material. For the aluminum configuration, the analytical model predicted approximately 68.7 in of tip deflection at 3.8g and 103.1 in at 5.7g. For the carbon-fiber spar cap configuration, the analytical model predicted approximately 16.7 in at 3.8g and 25.1 in at 5.7g.

Table 36: Analytical and Finite Element Analysis Deflection Comparison

Load Case	Aluminum Analytical	Aluminum FEM	Carbon-Fiber Analytical	Carbon-Fiber FEM
1g reference	18.1 in	8.99 in	4.4 in	4.59 in
3.8g limit	68.7 in	101.25 in	16.7 in	57.34 in
5.7g ultimate	103.1 in	151.48 in	25.1 in	76.80 in

The finite element model predicted larger deflections than the analytical model for the higher load cases, especially for the carbon-fiber spar cap configuration. This difference is expected because the analytical beam model assumes an idealized load path and simplified bending stiffness, while the FEMAP model captures additional flexibility from the shell structure, skin and rib deformation, glued interfaces, and the chord-transition region. Therefore, the analytical model was not used as a final compliance tool. Instead, it served as a useful check showing that the finite element results were reasonable in trend and that spar cap stiffness and wing-box depth were the dominant factors controlling the wing deflection.

3.3 Sizing and Performance Estimations

3.3.1 Aerodynamic Performance

An aerodynamic performance comparison was evaluated between the previous interim design winner, a standard V-tail configuration, against a similar design with a airfoil sectioned main wing. The wing used a NACA4418 airfoil inboard and a NACA4412 outboard to reduce drag, create an elliptical load distribution, and enhance efficiency. The first comparison was done using lift coefficient, drag coefficient, and lift to drag ratio across angles of attack ranging from -10 degrees to 20 degrees. The lift coefficient curves show how each aircraft configuration generates lift across the angle-of-attack sweep. The drag coefficient curves show the aerodynamic penalty associated with increasing angle of attack, while the lift-to-drag ratio was used as the primary efficiency metric. A higher lift-to-drag ratio indicates a more efficient configuration, which is especially important for a MALE UAV because endurance and range are strongly affected by aerodynamic efficiency.

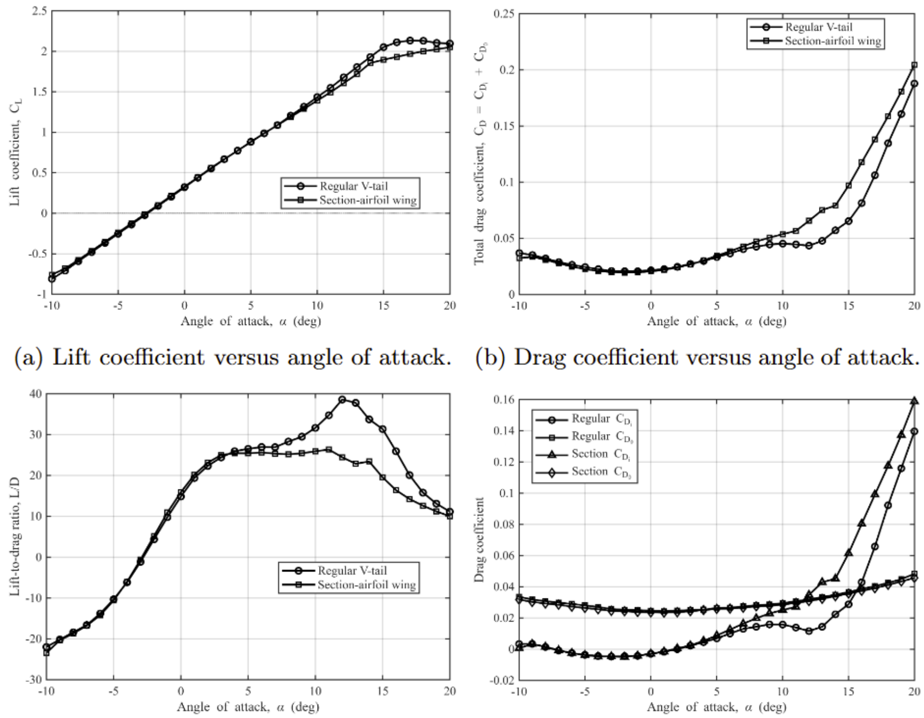

(a) Lift coefficient versus angle of attack. (b) Drag coefficient versus angle of attack.

(c) L/D versus angle of attack. (d) Induced and profile drag comparison.

Figure 67. Aerodynamic performance comparison between the regular V-tail and section-airfoil wing configurations across the angle-of-attack sweep.

Figure 49 compares the aerodynamic performance of the regular V-tail and section-airfoil wing configurations across the angle-of-attack sweep. Both configurations show nearly identical lift behavior through the linear range, indicating that the section-airfoil modification did not significantly change the overall lift curve slope at low to moderate angles of attack. Differences become more noticeable at higher angles of attack, where the regular V-tail reaches a slightly higher maximum lift coefficient before leveling off, while the section airfoil wing produces slightly lower lift. The drag trends show that both configurations have similar drag at low angles of attack, but the section airfoil wing develops higher total drag at larger angles of attack, mainly due to the increase in induced drag. This is also reflected in the lift to drag ratio, where the regular V-tail achieves a higher peak efficiency and maintains better aerodynamic efficiency over the higher angle of attack range. Overall, the regular V-tail provides better aerodynamic performance for the final configuration because it offers comparable lift generation with lower drag and a higher maximum lift-to-drag ratio.

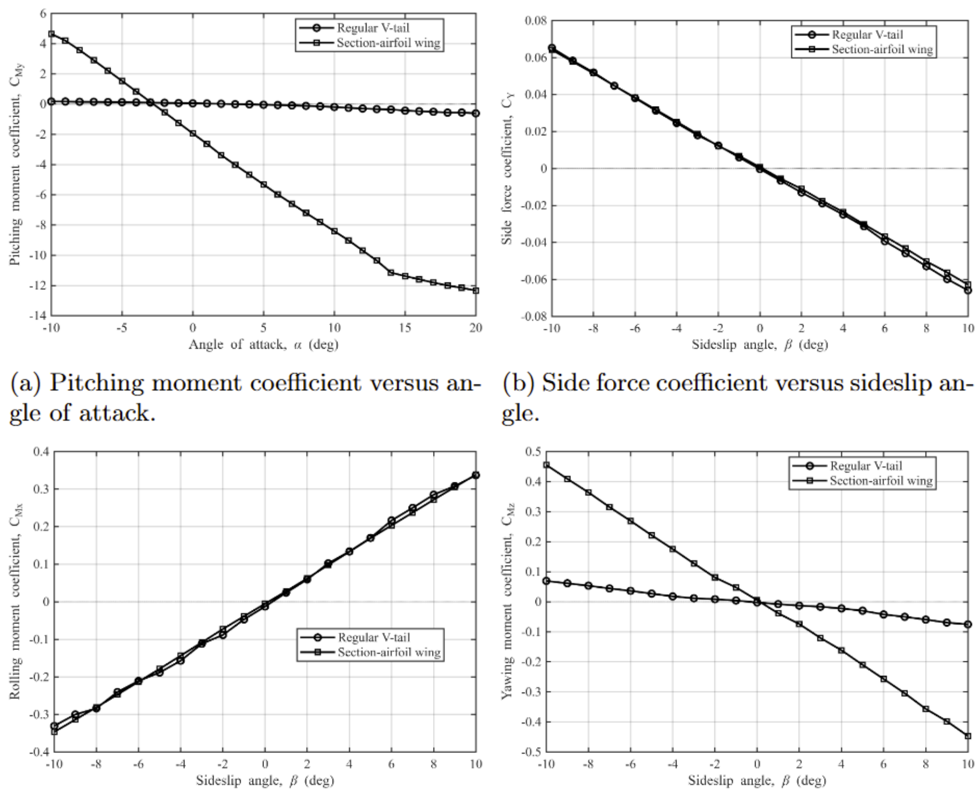

(a) Pitching moment coefficient versus angle of attack.

(b) Side force coefficient versus sideslip angle.

(c) Rolling moment coefficient versus sideslip angle.

(d) Yawing moment coefficient versus sideslip angle.

Figure 68. Combined static stability comparison for the regular V-tail and section-airfoil wing configurations across the angle-of-attack sweep.

As shown in Figure 50, the regular V-tail configuration also showed more acceptable pitch trim behavior than the section airfoil wing configuration. The regular V-Tail is trimmed for an angle of attack of approximately 3 to 4 degrees while the section airfoil is poorly trimmed for a negative angle of attack of approximately -3 degrees. Both configurations, however, are laterally stable following FlightStream's moment sign convention. As noted previously, this differs from the sign convention presented in Raymer's book for the course. Since the regular V-tail configuration was closer to a reasonable pitch trim condition, it was selected as the more appropriate configuration for the final static stability discussion.

The section-airfoil wing configuration was investigated to determine whether modifying the wing section could improve aerodynamic performance. The lift and drag trends showed that the configuration remained aerodynamically functional, but the pitching moment behavior indicated a poor trim condition compared with the regular V-tail. Because of this, the section-airfoil configuration was not treated as the preferred final configuration, although it still provided useful comparison data.

The final improved V-tail UAV configuration was evaluated against the primary mission performance requirements using aerodynamic data from FlightStream, estimated propulsion performance for the TPE331-10 turboprop, and preliminary ground-roll and mission-performance calculations. The analysis included takeoff ground roll, landing rollout, rate of climb, range, and endurance. The results indicate that the aircraft satisfies the major design requirements, including takeoff distance, landing distance, climb performance, range, endurance, maximum cruise speed, payload capacity, and operational ceiling.

Takeoff performance plots are shown in Figure 69 and Figure 70, where ground speed and ground-roll distance are plotted as functions of time for rolling friction coefficients of $\mu_r =$ 0.02, 0.03, and 0.04. These friction values were selected to represent typical paved-runway rolling resistance conditions. The aircraft accelerates to the required liftoff speed in approximately 19 to 20 seconds, depending on the assumed rolling friction coefficient. The corresponding ground roll distance remains below approximately 1,600 ft for all cases shown. This satisfies the design requirement of a takeoff distance less than 2,345 ft.

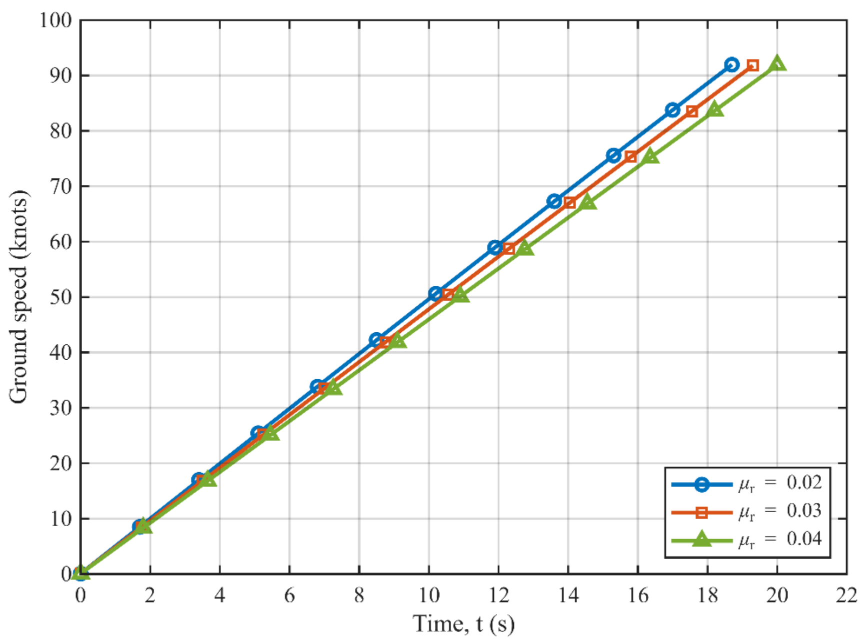

Figure 69. Final Design Takeoff Ground Roll Speed vs. Time for Multiple Friction Coefficients.

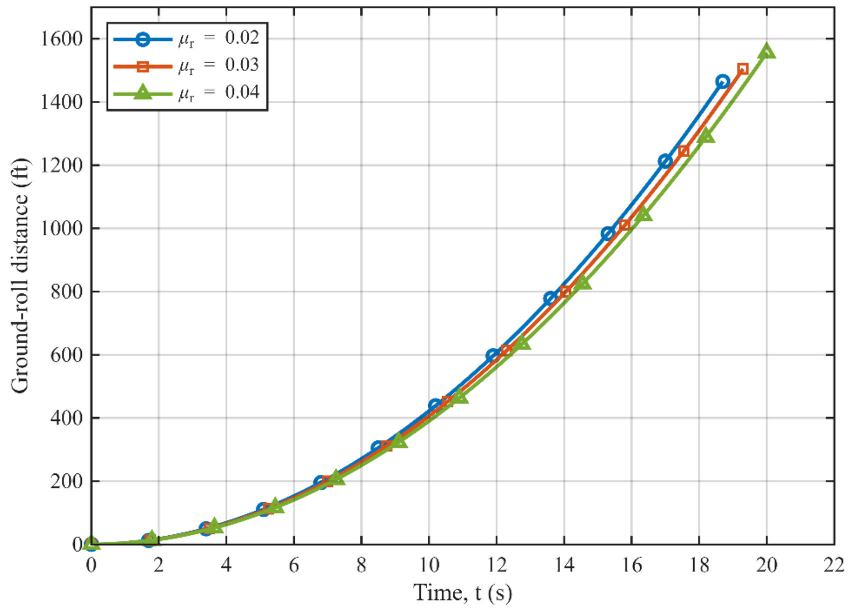

Figure 70. Final Design Takeoff Ground-Roll Distance vs. Time for Multiple Friction Coefficients.

Landing performance is shown in Figure 71 and Figure 72, where rollout distance and ground speed are plotted after touchdown for braking friction coefficients of $\mu_b = 0.25, 0.35,$ and 0.45. These values represent a range of moderate to strong braking effectiveness on a paved runway. The lowest braking case, $\mu_b = 0.25$, produces the longest rollout distance, reaching approximately 1,900 ft before the aircraft comes to a complete stop. The higher braking cases stop at shorter distances of approximately 1,400 ft and 1,100 ft, respectively. Even the most conservative braking case remains below the landing distance requirement of 2,250 ft. Therefore, the improved V-tail configuration satisfies the landing distance requirement with reasonable braking assumptions.

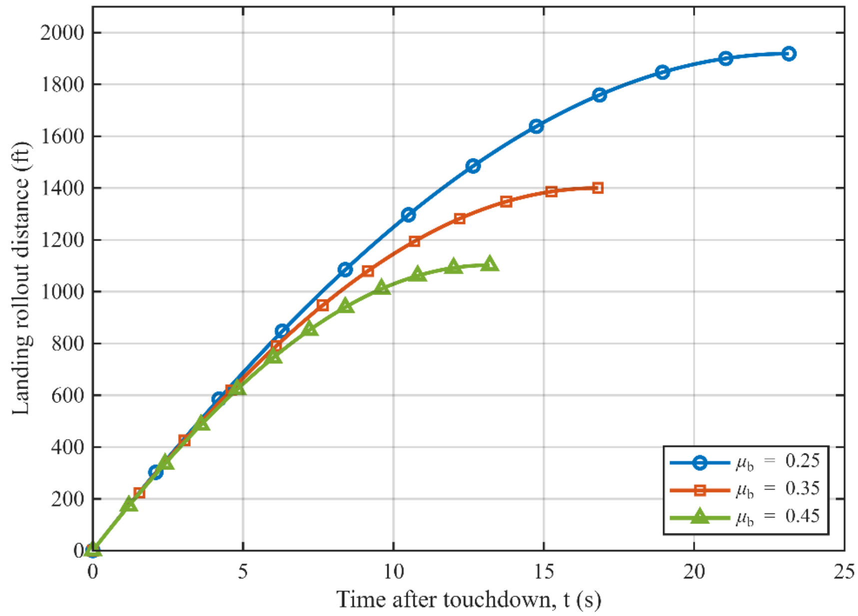

Figure 71. Landing Rollout Distance vs. Time for Multiple Braking Friction Coefficients.

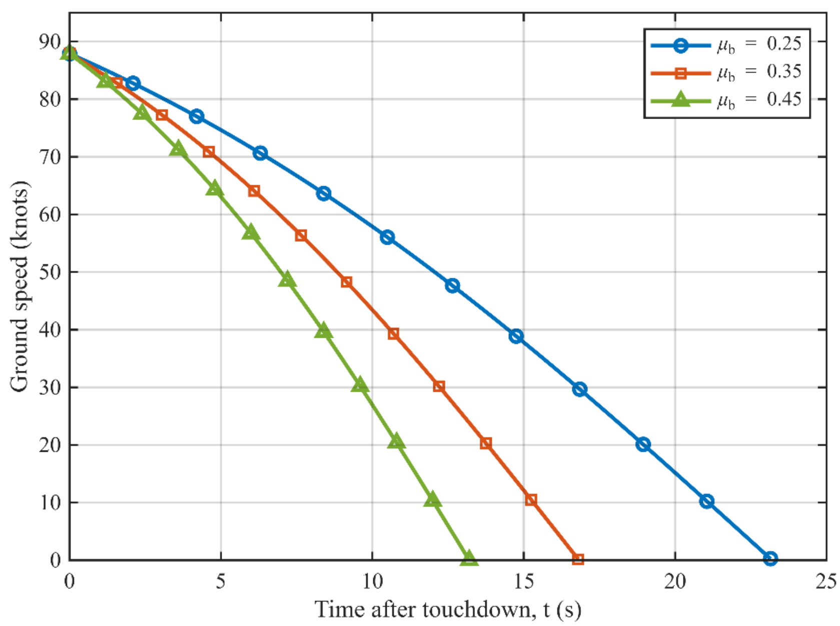

Figure 72. Landing Ground Speed vs. Time for Multiple Braking Friction Coefficients.

The rate-of-climb performance is shown in Figure 73 and Figure 74. The rate of climb decreases with altitude due to the reduction in air density and available engine power. At sea level, the aircraft achieves a maximum rate of climb of approximately 4,000 ft/min, which exceeds the target climb requirement of 3,424 ft/min. At higher altitudes, the available climb rate decreases, but the aircraft maintains positive climb capability through the evaluated altitude range. The best rate of climb plot shows that the aircraft still has approximately 1,000 ft/min of climb capability near 41,000 ft. This supports the operational ceiling requirement of 41,001 ft and indicates that the aircraft can operate at the required 30,000 ft mission altitude with adequate climb margin.

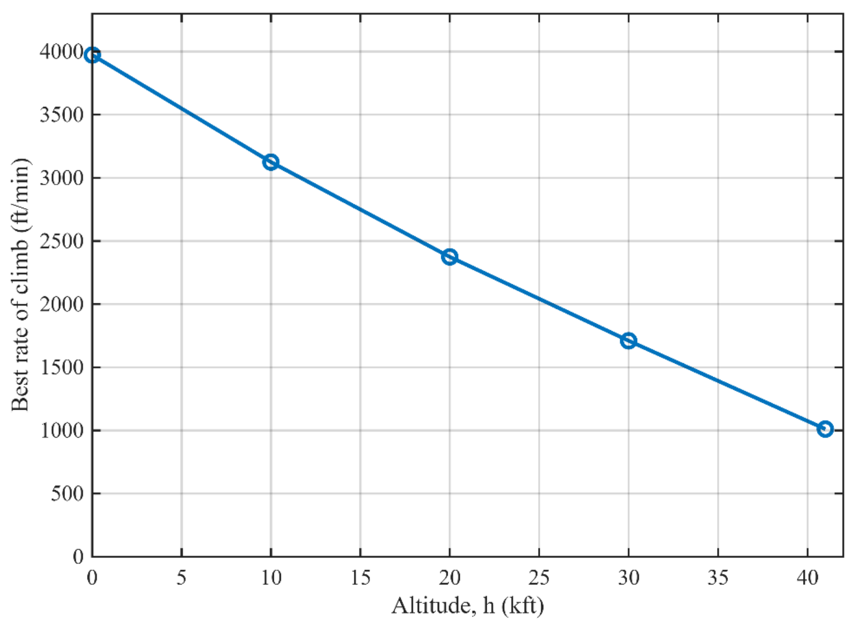

Figure 73. Rate of Climb vs. True Airspeed at Multiple Altitudes.

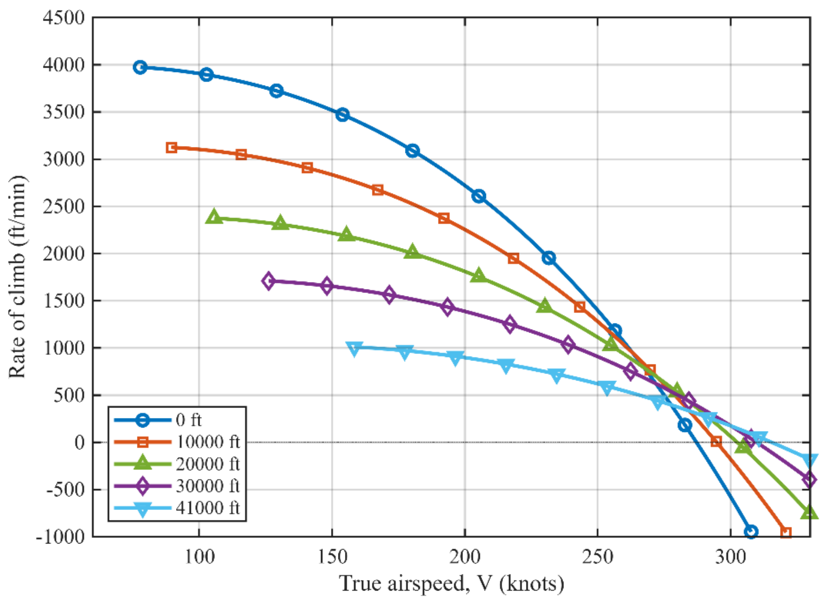

Figure 74. Best Rate of Climb vs. Altitude.

Range and endurance plots are shown in Figure 75 and Figure 76. The range plot indicates a maximum estimated range of approximately 4,200 nmi near the lower end of the evaluated cruise speed range, with range decreasing as cruise speed increases. This occurs because higher cruise speeds require significantly more shaft power to overcome drag, which increases fuel burn. The endurance plot follows a similar trend, with endurance highest at lower cruise speeds and decreasing as speed increases. The maximum estimated endurance is greater than 30 hours in the plotted range, which exceeds the required 8-hour mission endurance. The current design table lists a system range of 7,801 nmi and a total mission range of 8,977 miles; these exceed the requirements of 1,125 nmi and 750 miles, respectively. The plotted values remain consistent with the conclusion that the aircraft has substantial range and endurance margin, although the exact numerical range depends strongly on the assumed fuel burn, propulsive efficiency, and cruise condition.

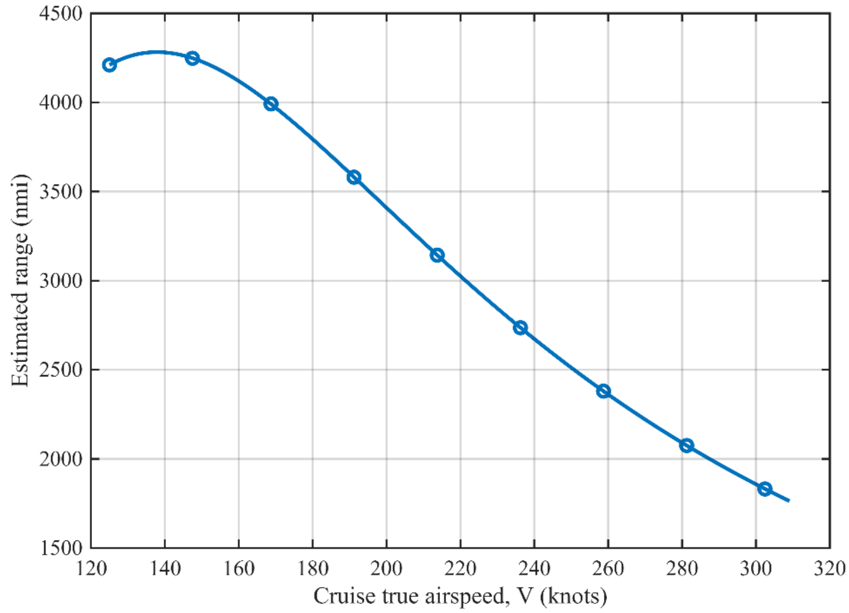

Figure 75. Estimated Range vs. Cruise True Airspeed.

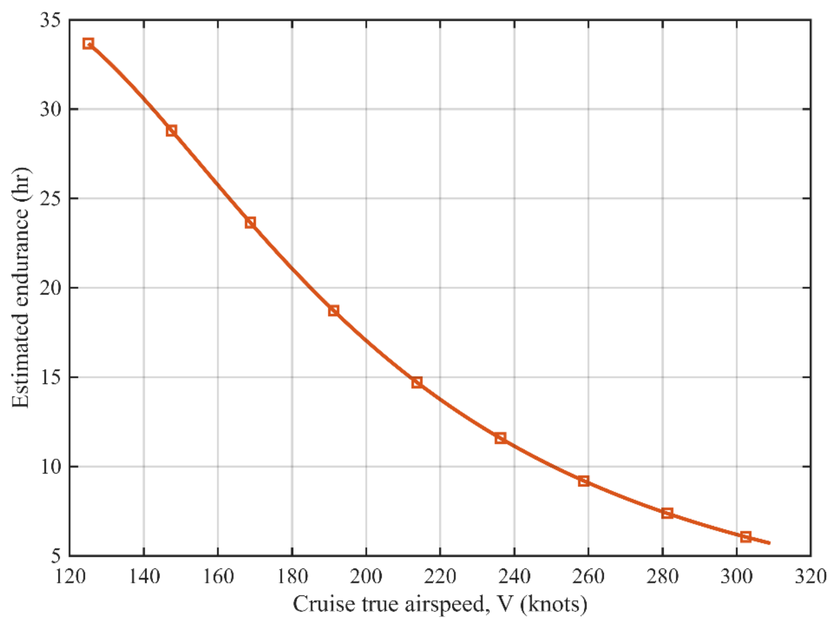

Figure 76. Estimated Endurance vs. Cruise True Airspeed.

Overall, the performance results indicate that the improved V-tail UAV configuration satisfies the major project requirements. The aircraft has sufficient takeoff and landing performance, with predicted ground roll distances below the required limits. The climb analysis shows that the aircraft exceeds the target maximum climb rate and maintains positive climb capability up to the required operational ceiling. The range and endurance estimates show significant margin relative to the mission requirements, supporting the intended long endurance ISR mission profile.

The above performance calculations were based on several assumptions. Sea-level standard air density was used for takeoff and landing. The takeoff and landing runs were assumed to occur on a level paved runway with no wind. Rolling friction coefficients of $\mu_r = 0.02$, 0.03, and 0.04were used for takeoff, while braking friction coefficients of $\mu_b = 0.25$, 0.35, and 0.45were used for landing. The takeoff and landing aerodynamic coefficients were estimated from the FlightStream lift and drag data for the regular V-tail configuration. The TPE331-10 turboprop was modeled using an approximate sea-level shaft power of 940 shp, and propulsive efficiency was assumed to be $\eta_p = 0.82$. Fuel burn and range estimates used an approximate brake specific fuel consumption value and assumed steady cruise conditions. The analysis did not include wind, runway slope, detailed propeller effects, or control surface actuation.

Based on the plotted performance results and the design verification table, the improved V-tail configuration meets the specified performance requirements. The takeoff ground roll remains below the 2,345 ft limit, and the landing rollout remains below the 2,250 ft limit for the assumed braking cases. The maximum rate of climb is approximately 4,223 ft/min, exceeding the 3,424 ft/min requirement. The aircraft is capable of operating at the required 30,000 ft mission altitude and satisfies the 41,001 ft ceiling requirement based on the available climb margin. The estimated maximum cruise speed of 310 knots remains below the 370-knot constraint, and the structural never exceeds speed requirement is satisfied. The aircraft also meets the range and endurance requirements with substantial margin. Therefore, the improved V-tail configuration is considered compliant with the major mission and performance constraints.

3.3.2 Wing Loading

The wing loading results show that the two configurations produce very similar overall structural loading at the 10-degree angle-of-attack condition. The regular V-tail configuration produced a total integrated vertical load of 901.2 lbf, while the other wing configuration produced 892.1 lbf, a difference of only about 1.0%. The integrated root shear force followed the same trend because it is directly obtained by integrating the vertical load distribution along the span. The root-bending moments were also very close, with the regular V-tail producing 10,830.6 lbf-ft and the other wing producing 10,777.7 lbf-ft, a difference of about 0.5%.

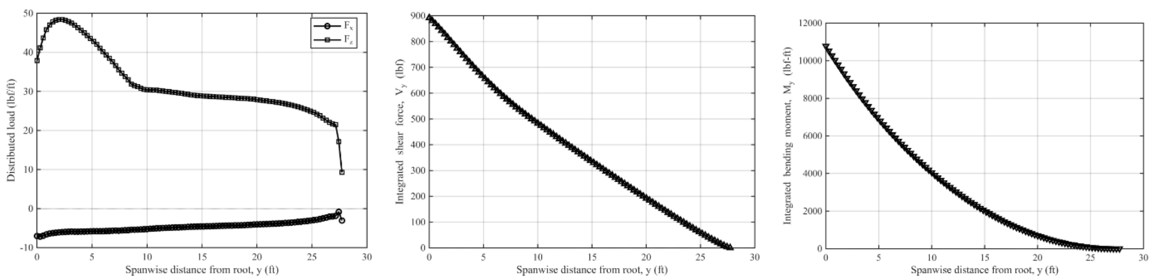

(a) Wing loading distribution. (b) Shear force diagram. (c) Bending moment diagram.

Figure 77. Spanwise loading and resulting internal force distributions for the sectional airfoil configuration half-wing

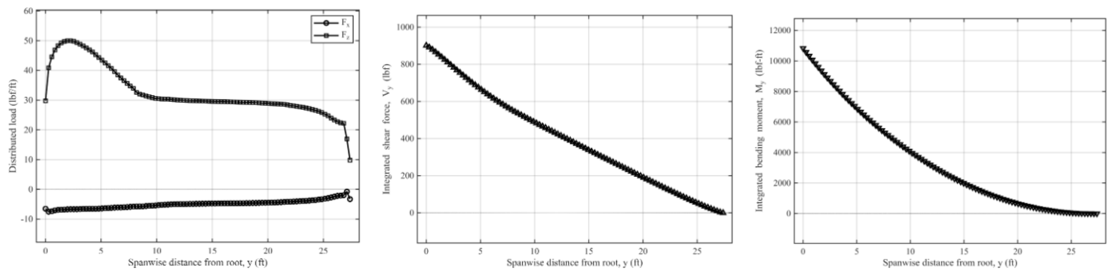

(a) Wing loading distribution.

(b) Shear force diagram.

(c) Bending moment diagram.

Figure 78. Spanwise loading and resulting internal force distributions for the regular V-tail configuration half-wing

The spanwise loading distributions are also similar in shape. Both cases show the highest sectional loading near the inboard portion of the wing, followed by a gradual reduction toward the tip. This produces the expected shear force diagram, where the shear is largest at the root and decreases toward zero at the tip. Similarly, the bending moment is largest at the root and smoothly decreases toward zero outboard. The regular V-tail case has a slightly higher peak vertical distributed load and a slightly larger integrated vertical load, which explains its marginally higher root shear and bending moment. However, the differences are small, suggesting that the two configurations would impose nearly the same primary bending requirements on the wing structure. One noticeable change from the plots generated in the interim reports is the smooth nature of the data points along the span. Previously, there were abrupt changes in the data near the root section, thought to have been caused by the number of sampling points and proximity to the root of the wing where geometry changes sharply. It should be noted that for each of design iterations in the interim report that an error went unnoticed prior to being submitted. The root section of the wing for each of the loading diagrams is not consistent with the expected distribution. This error is thought to have occurred because too few sampling points were taken. This error was realized after the fact and the number of sampling points increased for the plots generated in this section, which seems to have significantly improved the smoothness and quality of the loading distribution.

Overall, the wing loading comparison indicates that changing between these configurations does not significantly reduce the structural load demand. The regular V-tail produces slightly higher vertical loading and bending moment, but the difference is small enough that both configurations would likely require a similar wing structural design. The final configuration should therefore be selected more strongly based on aerodynamic trim, stability, and efficiency rather than wing-root bending load alone.

3.3.3 Sizing Estimations

Table 37: Weight Estimation Breakdown

	A	B
1	Wing structure	809
2	Fuselage structure	857
3	Empennage / tail Ruddervi	292
4	Landing gear	273
5	Engine + propeller	588
6	Fuel system hardware	188
7	Flight controls and hydraulics	233
8	Avionics and electrical	390
9	Sensor and payload	575
10	Support System	405
11	TOTAL EMPTY WEIGHT	4610
12		
13	FUEL WEIGHT	1407
14	TOTAL WEIGHT (MTOW)	6017

Table 37 illustrates the weight breakdown for the final AO design, organized by major aircraft subsystems. The total empty weight of the aircraft is calculated to be 4,610 lb., which includes all structural components, propulsion systems, avionics, and mission payloads, but excludes fuel. The largest contributors to the empty weight are the fuselage structure (857 lb.) and wing structure (809 lb.), which is expected since these components must carry aerodynamic loads and provide overall structural integrity. The engine and propeller system (588 lb.) and sensor/payload system (575 lb.) are also significant contributors, reflecting the importance of propulsion performance and mission capability in the overall design.

Additional subsystems such as avionics and electrical (390 lb), support systems (405 lb), and flight controls and hydraulics (233 lb.) contribute to overall functionality and control of the aircraft. The landing gear (273 lb.) and empennage/tail section (292 lb.) provide stability, control, and safe ground operations, while the fuel system hardware (188 lb.) supports fuel storage and delivery.

The total fuel weight is estimated at 1,407 lb., which is sized to meet endurance and mission range requirements. When combined with the empty weight, this results in a maximum takeoff weight (MTOW) of 6,017 lb.

Table 38: Flight Performance Estimates

Parameter	Value
Minimum Thrust Estimates	
Loiter / Level Flight	231.4 lbs
Steady Climb (5.0°)	755.8 lbs
Takeoff (within 2345 ft)	1008.6 lbs
Stall Speed	116.5 ft/s (69.0 knots)
Liftoff Speed	139.8 ft/s (82.8 knots)
Rate of Climb (Angel One)	
Available SL Thrust	1690.6 lbs (7520 N)
Target Max Climb Rate	3424 ft/min
Calculated Max Rate of Climb	3920.2 ft/min
Best Climb Speed (V_y)	213 knots
Landing Distance Estimate	
Touchdown Speed	133.9 ft/s (79.4 knots)
Calculated Total Landing	1934.1 ft (Target: 2250 ft)
Max Cruise at 41,001 ft	
Available Thrust at 41k ft	407.5 lbs
Calculated Max Cruise Speed (TAS)	349.0 knots (Target: 370 kn)
Note: V_{NE} limit of 285 kn is IAS. 370 kn TAS at 41k ft is safe.	
Range and Endurance Estimates	
Fuel Weight	1407 lbs
Target Range	1125 nmi
Calculated Range (1.10 lb/mi burn)	1111.5 nmi
Theoretical Breguet Range (Max L/D)	3582.8 nmi
Theoretical Max Endurance	22.32 hours

Table 38 details the final flight performance estimations for the Angel One configuration, generated via MATLAB. These values build on the foundational aerodynamic coefficients and structural weights established in earlier design iterations, representing the finalized capabilities of the aircraft at maximum takeoff weight.

The propulsion system provides an available sea-level thrust of 1690.6 lbs, which offers a substantial margin over the required takeoff thrust of 1008.6 lbs. This excess thrust translates directly into a calculated maximum rate of climb of 3920.2 ft/min at a best climb speed (V_y) of 213 knots. This easily satisfies the Siemens requirement to achieve a climb rate of at least 3424 ft/min, ensuring the aircraft can rapidly reach its operational altitude.

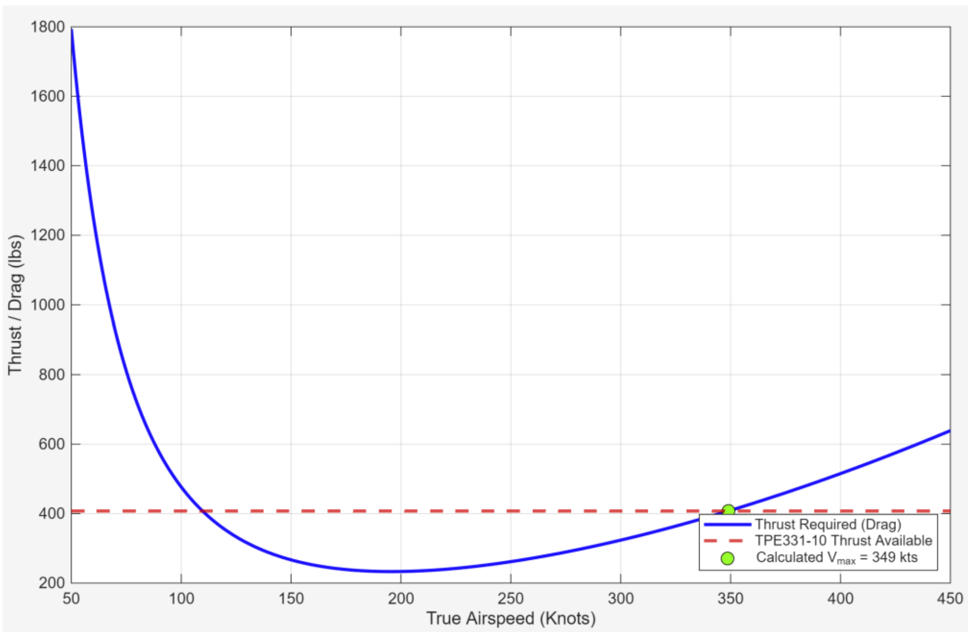

Figure 79. Thrust required vs thrust available at 41,000 ft

At the target service ceiling of 41,001 ft, as seen in figure 79, the available thrust scales down to 407.5 lbs, yielding a maximum cruise speed of 349.0 knots (TAS). This verifies that the aircraft can operate near its upper altitude limits without exceeding the 370 knot maximum cruise constraint or the 285 knot (IAS) V_NE structural limit. During recovery, a calculated touchdown speed of 79.4 knots results in an estimated total landing distance of 1934.1 ft, providing a comfortable safety margin well below the 2250 ft runway restriction.

The aerodynamic efficiency of the configuration is most evident in the endurance metrics. Relying on the 1407 lbs fuel capacity, the theoretical Breguet range extends to 3582.8 nmi, supporting a maximum endurance of over 22 hours. However, under a more conservative operational burn rate (1.10 lb/mi), the calculated system range comes to 1111.5 nmi. While this represents a marginal 1.2% shortfall against the 1125 nmi baseline requirement, the exceptional maximum endurance indicates that slight adjustments to the mission profile, loiter throttle settings, or a minor increase in fuel fraction would comfortably close this gap.

3.4 Trade-Off Study

The final trade study was limited to the aerodynamic, stability, and structural loading results because the sectioned wing V-tail represented only a minor geometric perturbation from the regular V-tail baseline. Since the two configurations used the same overall aircraft layout, propulsion system, payload assumptions, mission requirements, and similar wing planform characteristics, a full repeat of the weight buildup and sizing analysis was not performed. Any changes in total weight, fuel sizing, or major component sizing were expected to be small relative to the overall aircraft mass and would not likely alter the primary conclusions of the configuration comparison. Instead, the trade study focused on the design of drivers most affected by the wing modification: lift, drag, aerodynamic efficiency, trim, and static stability. The sectioned wing V-tail was not carried forward because it failed an essential early-stage design requirement of acceptable pitch trim. Although it remained capable of generating lift, its pitching moment behavior indicated that additional work would be needed to shift the center of gravity. This my have included adjustment to the tail redesign, incidence changes, or control surface deflection before it could be considered a well-trimmed aircraft. In addition, the sectioned wing configuration showed worse aerodynamic performance, including higher drag growth and lower lift to drag ratio at higher angles of attack. Because the modified design introduced trim concerns and reduced aerodynamic efficiency without providing a meaningful structural loading advantage, the regular V-tail configuration was selected as the preferred final design.

Table 39. Final Design Trade-Off Study

Evaluation Criterion	Weight	Regular V-Tail Score	Regular Weighted Score	Sectioned-Wing V-Tail Score	Sectioned Weighted Score
Aerodynamic efficiency, L/D	0.20	5	1.00	3	0.60
Lift generation and stall behavior	0.12	5	0.60	4	0.48
Drag performance	0.12	5	0.60	3	0.36
Longitudinal trim suitability	0.18	5	0.90	2	0.36
Longitudinal static stability	0.12	5	0.60	3	0.36
Lateral-directional static stability	0.08	4	0.32	4	0.32
Wing structural loading	0.08	4	0.32	4	0.32
Mission performance compliance	0.06	5	0.30	4	0.24
Design maturity and implementation risk	0.04	5	0.20	3	0.12
Total	**1.00**	–	**4.84**	–	**3.16**

5.0 Serviceability and Lifecycle Cost Analysis

5.1 Serviceability

The Angel Owl (AO) system was designed with a strong emphasis on aircraft readiness, rapid turnaround time, and ease of maintenance. These considerations directly influenced several key design decisions, including crew structure, component accessibility, subsystem layout, and monitoring systems. To minimize ground time while maximizing mission availability, the AO is designed to be operated by a four-person crew, split evenly between ground operations and flight operations. Two crew members are responsible for launch, recovery, and refueling procedures, while the remaining two manage flight operations. This division reduces operational bottlenecks and allows for parallel task execution, ultimately improving turnaround efficiency.

A major design driver was component accessibility. The aircraft incorporates strategically placed maintenance access doors, allowing direct access to high-failure and high-maintenance components such as the propulsion system, avionics, and fuel system. This reduces the need for extensive disassembly during inspections or repairs, significantly decreasing maintenance time and improving overall serviceability.

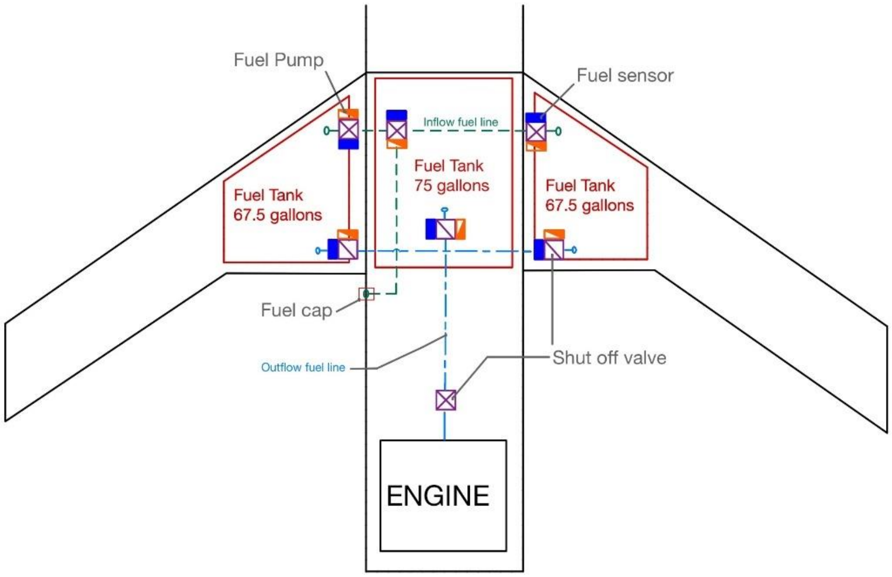

Figure 79. Fuel System Layout

The fuel system layout was also selected to simplify operations. A single fuel cap location was implemented, allowing refueling from one point while internal fuel lines and transfer pumps distribute fuel across multiple tanks. This reduces refueling complexity and time while maintaining system redundancy using valves and level sensors, as seen in the figure above. To further reduce downtime and maintenance burden, the AO uses a Honeywell TPE331-10 turboprop engine, which is known for its mechanical simplicity, reliability, and high technical readiness level. The reduced number of moving parts compared to more complex propulsion systems leads to fewer failure points and longer service intervals. Additionally, avionics systems are designed as line-replaceable units (LRUs). This allows faulty components to be quickly swapped rather than repaired in place, minimizing downtime and enabling faster return-to-service. Finally, the aircraft integrates Built-In Test (BIT) and Health and Usage Monitoring Systems (HUMS). These systems continuously monitor parameters such as temperature, vibration, and pressure, enabling early fault detection and predictive maintenance. This reduces unexpected failures and allows maintenance to be scheduled proactively rather than reactively. Overall, serviceability considerations led to a design that prioritizes ease of access, reduced maintenance time, simplified operations, and increased aircraft availability, all of which are critical for sustained mission performance.

5.2 Negative Externalities

Table 40: Negative Externalities Listing

Material	Description	Scope	Severity
JP-8 Fuel Emissions	CO_2 and N_2O emissions during operation	Environmental	High
Long Endurance Flights	Accumulation of emissions over long missions	Environmental	High
LRU Replacements	Electronic waste from component swaps	Environmental	Medium
Noise Pollution	Disturbance to wildlife and communities	Environmental	Medium
Aluminum/Titanium Production	Mining and refining emissions	Environmental	Medium
Carbon Fiber Composites	Difficult recycling and manufacturing waste	Environmental	Medium

The Angel Owl system introduces several environmental and societal impacts, primarily associated with fuel consumption, material usage, and operational characteristics. One of the primary contributors to negative externalities is the use of JP-8 fuel, which produces CO_2 and N_2O emissions during combustion. Due to the aircraft's long endurance mission profile, these emissions accumulate over time, increasing the overall environmental impact compared to shorter-duration systems. Additionally, the use of line-replaceable units (LRUs), while beneficial for maintenance, contributes to electronic waste generation as components are replaced rather than repaired. This creates disposal and recycling challenges, particularly for sensitive avionics equipment. At low altitudes, the aircraft generates noise pollution, which can disturb nearby communities and wildlife. This is especially relevant during takeoff, landing, and low-altitude surveillance operations. Material selection also contributes to environmental impact. The use of aluminum and titanium alloys requires energy-intensive mining and refining processes, which produce emissions and environmental degradation. Similarly, carbon fiber composites, while beneficial for weight reduction and performance, are difficult to recycle and present manufacturing challenges. Overall, while the AO system provides strong operational performance, these externalities highlight trade-offs between performance, sustainability, and lifecycle impact.

5.3 Costs

Table 41: Cost Breakdown

Airframe	$8,000,000
Propulsion	$1,500,000
Avionics	$500,000
Sensors	$275,000
Communications	$1,000,000
Landing Gear	$1,250,000
Fuel System	$950,000
Integration	$2,500,000
Assembly	$4,500,000
TOTAL ESTIMATED COST	$20,475,000

The lifecycle cost of the Angel Owl system includes development, manufacturing, operation, and end-of-life considerations. These costs played a significant role in shaping the final design. Cost considerations directly influenced several design decisions. The selection of the TPE331-10 turboprop engine was driven by its balance between performance, reliability, and lower operational cost compared to more complex propulsion systems. The use of LRUs reduces maintenance labor costs and downtime, even though it may increase replacement costs. Similarly, composite materials were selected to reduce weight and improve efficiency, despite higher manufacturing complexity and cost. The fuel system design, including a single refueling point, reduces operational complexity and ground crew requirements, lowering long-term operational costs. Overall, the design reflects a balance between performance, reliability, and cost efficiency, ensuring that the system remains economically viable over its operational lifetime.

6.0 Engineering Drawings

6.1 Fuselage Structure

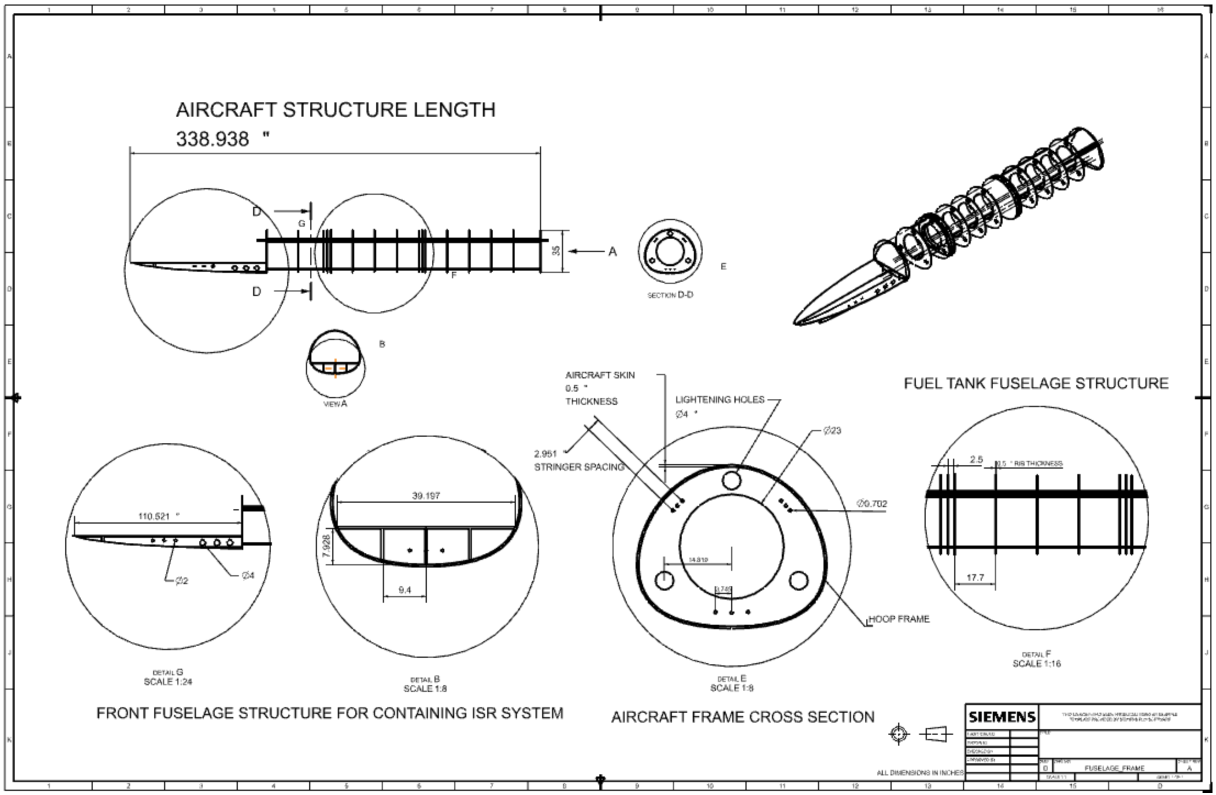

Figure 80. Fuselage Structure Drawing.

Table 42: Fuselage Area and Mass Characteristics

Property	Value	Units
Surface Area	41493.6227	in^2
Volume	9629.9380	in^3
Center of Mass	Point(0.0725, 16.6051, -3.5025)	in
Mass	2724.3095	lbm
Weight	2724.3095	lbf
Moments of Inertia	{23187838.6691, 600748.7642, 23229506.7456}	$lbm \cdot in^2$

6.2 Wing Structure

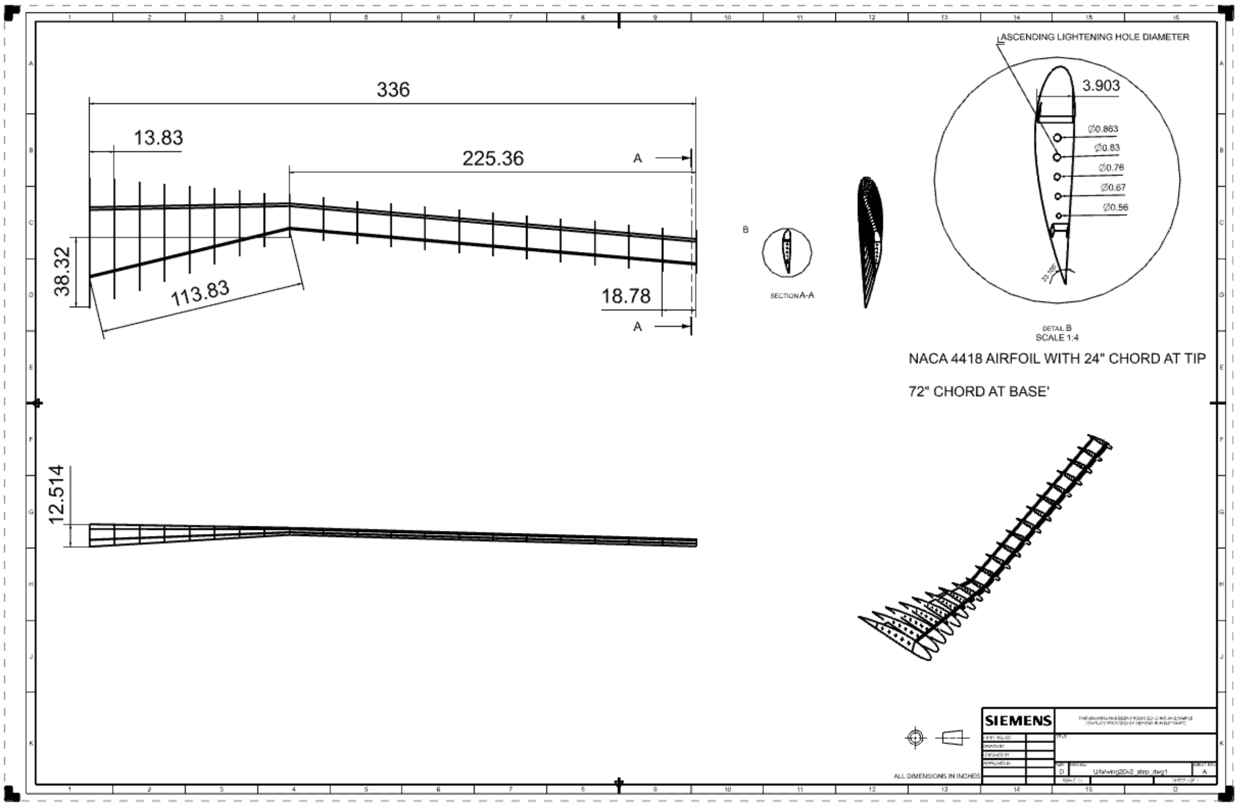

Figure 81. Main Win Internal Structure Drawing.

Table 43: Main Wing Geometric Characteristics

Property	Value	Units
Area	4191.9152	in^2
Perimeter	5868.68128	in

6.3 Tail Structure

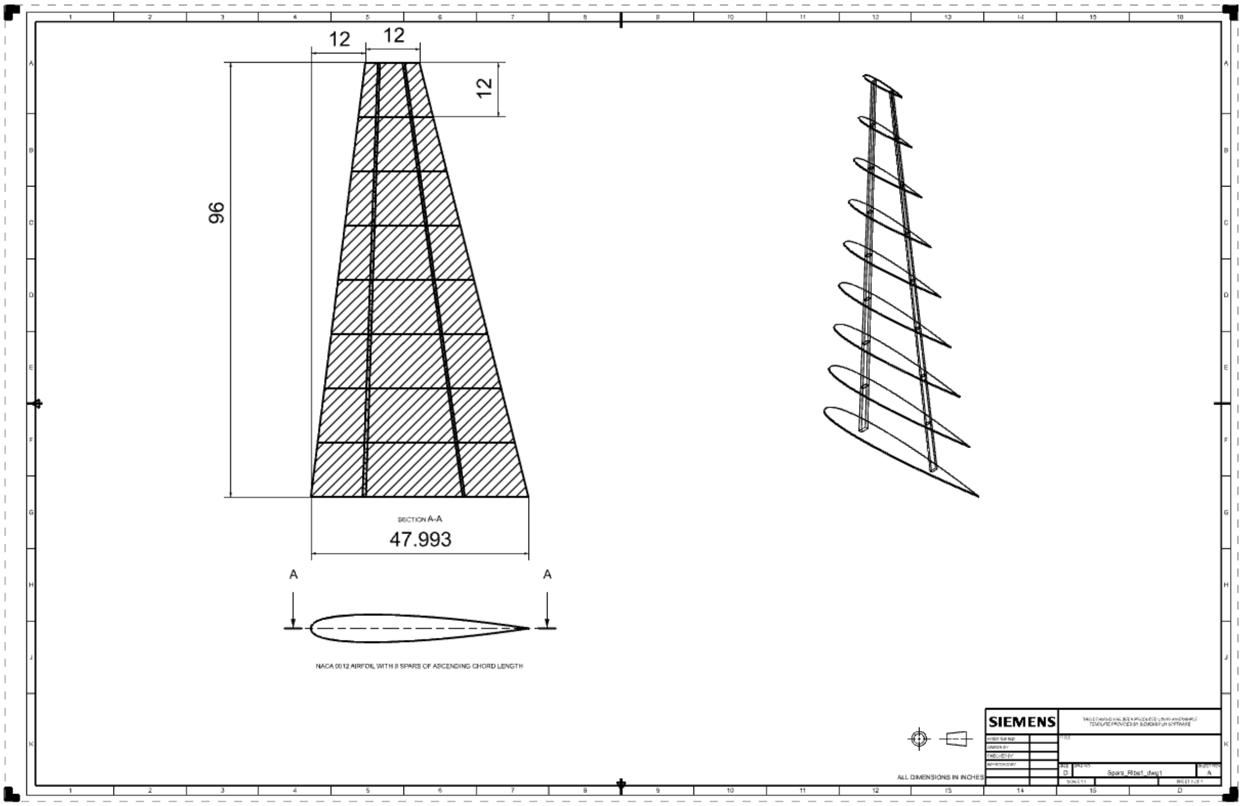

Figure 82. Tail Internal Structure Drawing.

Table 44: Tail Geometric Characteristics

Property	Value	Units
Area	2409.8021	in^2
Perimeter	3227.2656	in
Centroid	Point(19.3192, -0.0011, 32.4898)	in

7.0 Conclusion

This report presented the complete design development of the Angel One Medium-Altitude Long-Endurance (MALE) UAV for Intelligence, Surveillance, and Reconnaissance (ISR) missions. Starting from initial conceptual designs, multiple configurations were generated, analyzed, and refined through iterative modeling, trade studies, and performance evaluations. Each stage of the design process progressively improved aerodynamic efficiency, stability, and mission capability while ensuring compliance with regulatory and operational requirements.

The final configuration demonstrates a balanced solution that satisfies all key performance constraints, including range, endurance, payload capacity, and operational altitude. Trade-off studies confirmed that a turboprop propulsion system, carbon fiber composite structure, and optimized wing–tail configuration provide the best combination of efficiency, reliability, and cost-effectiveness for the mission. Additionally, the integration of mature technologies and adherence to FAA, EASA, military, and NATO standards ensures that the design is both feasible and aligned with real-world certification requirements.

Overall, the Angel One UAV represents a practical and efficient ISR platform capable of meeting modern mission demands. The design process highlights the importance of iterative refinement and engineering trade-offs in achieving a solution that balances performance, safety, and cost. This work provides a strong foundation for further development, including higher-fidelity simulations, subsystem optimization, and eventual prototype implementation.

Appendix

```
% ========================================================================
% Final Design (Iteration 3): Thrust, Range & Endurance Estimation Script
% Configuration: Angel One UAV
% ========================================================================
clear; clc;

%% 1. Input Parameters (Updated from Angel One Final Presentation)
% Aircraft Specs
W = 6017;               % Takeoff Weight (MTOW in lbs)
W_empty = 4610;         % Empty Weight (lbs)
W_fuel = 1407;          % Fuel Weight (lbs)
S = 162.278;            % Wing Area (sq ft)
LD_max = 26.0;          % Max Lift-to-Drag ratio
CL_max = 2.3;           % Max Lift Coefficient (Back-calculated for 69 kn stall speed)
AR = 22.93;             % Aspect Ratio
e = 0.85;               % Oswald Efficiency
CD0 = 0.023;            % Zero-lift drag
K = 1 / (pi * e * AR);  % Induced drag factor

% Environmental & Regulatory Requirements
rho = 0.002377;         % Air density at sea level (slugs/ft^3)
rho_41k = 0.000573;     % Air density at 41,000 ft (slugs/ft^3)
g = 32.17;              % Gravity (ft/s^2)
S_to_req = 2345;        % Required takeoff distance (ft)
S_land_req = 2250;      % Required landing distance (ft)
climb_angle_deg = 5;    % Desired climb angle (degrees)
mu_roll = 0.04;         % Rolling friction coefficient (typical for tarmac)
fuel_burn_req = 1.10;   % Operational fuel burn limit (lbs/mi)

%% 2. Loiter / Cruise Minimum Thrust
% The absolute minimum thrust to sustain level flight
T_loiter = W / LD_max;

fprintf('--- Minimum Thrust Estimates ---\n');
fprintf('Loiter / Level Flight: %.1f lbs\n', T_loiter);

%% 3. Climb Thrust
% Thrust required to maintain speed while climbing at a specific angle
gamma = deg2rad(climb_angle_deg);
T_climb = (W / LD_max) + W * sin(gamma);

fprintf('Steady Climb (%.1f deg): %.1f lbs\n', climb_angle_deg, T_climb);

%% 4. Takeoff Thrust Estimation
V_stall = sqrt((2 * W) / (rho * S * CL_max));
V_lof = 1.2 * V_stall;

a_req = (V_lof^2) / (2 * S_to_req);
F_accel = (W / g) * a_req;

V_avg = 0.7 * V_lof;
q_avg = 0.5 * rho * V_avg^2;

CD_to = 0.04;
D_avg = q_avg * S * CD_to;

L_avg = q_avg * S * (CL_max / 2);
F_friction = mu_roll * (W - L_avg);

T_takeoff = F_accel + D_avg + F_friction;

```

```
fprintf('Takeoff (within %d ft): %.1f lbs\n', S_to_req, T_takeoff);
fprintf('  -> Stall Speed: %.1f ft/s (%.1f knots)\n', V_stall, V_stall * 0.592484);
fprintf('  -> Liftoff Speed: %.1f ft/s (%.1f knots)\n', V_lof, V_lof * 0.592484);
fprintf('--------------------------------\n');

%% 5. Rate of Climb (ROC) Estimation
% Final design Honeywell TPE331-10 Turboprop equivalent thrust
T_avail_N = 7520;
T_avail = T_avail_N * 0.224809;         % Convert to lbs (~1690.6 lbs)

% Iterate to find Best Rate of Climb Speed (V_y)
V_test_knots_climb = 50:1:250;
V_test_fts_climb = V_test_knots_climb * 1.68781;
ROC_max_fpm = 0;
V_y_knots = 0;

for i = 1:length(V_test_fts_climb)
    V_fts = V_test_fts_climb(i);
    q_c = 0.5 * rho * V_fts^2;
    CL_c = W / (q_c * S);

    % Aerodynamic drag at this specific speed
    CD_c = CD0 + K * CL_c^2;
    D_c = q_c * S * CD_c;

    % ROC Equation: (Excess Thrust * Velocity) / Weight
    ROC_fts_test = ((T_avail - D_c) * V_fts) / W;
    ROC_fpm_test = ROC_fts_test * 60;

    if ROC_fpm_test > ROC_max_fpm
        ROC_max_fpm = ROC_fpm_test;
        V_y_knots = V_test_knots_climb(i);
    end
end

fprintf('--- Rate of Climb (Angel One) ---\n');
fprintf('Available SL Thrust: %.1f lbs (%d N)\n', T_avail, T_avail_N);
fprintf('Target Max Climb Rate: 3424 ft/min\n');
fprintf('Calculated Max Rate of Climb: %.1f ft/min\n', ROC_max_fpm);
fprintf('  -> Achieved at V_y (Best Climb Speed): %d knots\n', V_y_knots);
fprintf('--------------------------------\n');

%% 6. Landing Distance Estimation
V_td = 1.15 * V_stall;
theta_app = deg2rad(3);
S_air = 50 / tan(theta_app);

mu_brake = 0.4;
V_avg_land = 0.7 * V_td;
q_avg_land = 0.5 * rho * V_avg_land^2;

CD_land = 0.05;
D_avg_land = q_avg_land * S * CD_land;
CL_land_roll = CL_max / 2;
L_avg_land = q_avg_land * S * CL_land_roll;

F_frict_land = mu_brake * (W - L_avg_land);
F_retard = D_avg_land + F_frict_land;

a_land = (F_retard * g) / W;
S_ground = (V_td^2) / (2 * a_land);
```

```
S_land_total = S_air + S_ground;

fprintf('--- Landing Distance Estimate ---\n');
fprintf('Touchdown Speed: %.1f ft/s (%.1f knots)\n', V_td, V_td * 0.592484);
fprintf('Calculated Total Landing: %.1f ft (Target: %d ft)\n', S_land_total, S_land_req);
fprintf('--------------------------------\n');

%% 7. Maximum Cruise Speed (V_max) Estimation at Ceiling (41,001 ft)
sigma = rho_41k / rho;
T_avail_alt = T_avail * sigma; % Available Thrust at 41k ft

V_test_knots = 50:1:450;
V_test_fts = V_test_knots * 1.68781;
Drag_curve = zeros(size(V_test_fts));

for i = 1:length(V_test_fts)
    V = V_test_fts(i);
    q = 0.5 * rho_41k * V^2;
    CL_req = W / (q * S);
    CD_total = CD0 + K * CL_req^2;
    Drag_curve(i) = q * S * CD_total;
end

% Find Intersection (V_max)
[~, idx_vmax] = min(abs(Drag_curve - T_avail_alt));
V_max_knots = V_test_knots(idx_vmax);

fprintf('--- Max Cruise at 41,001 ft ---\n');
fprintf('Available Thrust at 41k ft: %.1f lbs\n', T_avail_alt);
fprintf('Calculated Max Cruise Speed (TAS): %.1f knots (Target Max: 370 kn)\n', V_max_knots);
fprintf('Note: V_NE limit of 285 kn is IAS. 370 kn TAS at 41k ft is safe.\n');
fprintf('--------------------------------\n');

%% 8. Range and Endurance Estimation (Propeller Aircraft)
W_initial = W;
W_final = W - W_fuel;

% --- 1. Simple Range Estimate (Using Environmental Spec Fuel Burn) ---
% Range = Fuel Weight / Fuel Burn Rate (lb/mi)
R_simple_mi = W_fuel / fuel_burn_req;
R_simple_nmi = R_simple_mi * 0.868976; % Convert statute miles to nautical miles

% --- 2. Theoretical Breguet Range & Endurance (Turboprop) ---
% Assumed generic efficiency metrics for a TPE331-class turboprop
eta_p = 0.80;            % Propeller efficiency
c_p = 0.50;              % Specific fuel consumption (lb/hp-hr)
c_p_fts = c_p / (550 * 3600); % Convert to lb/ft-lb-s for calculation

% Max Range occurs at max L/D for propeller aircraft
CL_range = sqrt(CD0 / K);
CD_range = CD0 + K * CL_range^2;
LD_max_prop = CL_range / CD_range;

% Max Endurance occurs at min power required (CL^1.5 / CD max)
CL_endurance = sqrt(3 * CD0 / K);
CD_endurance = CD0 + K * CL_endurance^2;

% Breguet Endurance Equation (Propeller) in Seconds
E_max_sec = (eta_p / c_p_fts) * (CL_endurance^1.5 / CD_endurance) * sqrt(2 * rho_41k * S) * ((1/sqrt(W_final)) - (1/sqrt(W_initial)));
```

```matlab
E_max_hrs = E_max_sec / 3600;

% Breguet Range Equation (Propeller) in feet
R_max_ft = (eta_p / c_p_fts) * LD_max_prop * log(W_initial / W_final);
R_max_nmi_theory = R_max_ft / 6076.12; % Convert to nmi

fprintf('--- Range and Endurance Estimates ---\n');
fprintf('Fuel Weight: %d lbs\n', W_fuel);
fprintf('Target Range: 1125 nmi\n');
fprintf('Calculated Range (using %.2f lb/mi operational burn): %.1f nmi\n', fuel_burn_req,
R_simple_nmi);
fprintf('Theoretical Breguet Range (Max L/D): %.1f nmi\n', R_max_nmi_theory);
fprintf('Theoretical Max Endurance: %.2f hours\n', E_max_hrs);
fprintf('--------------------------------\n');

% Plot
figure;
plot(V_test_knots, Drag_curve, 'b-', 'LineWidth', 2); hold on;
yline(T_avail_alt, 'r--', 'LineWidth', 2);
plot(V_max_knots, T_avail_alt, 'ko', 'MarkerSize', 8, 'MarkerFaceColor', 'g');

xlabel('True Airspeed (Knots)');
ylabel('Thrust / Drag (lbs)');
legend('Thrust Required (Drag)', 'TPE331-10 Thrust Available', ...
       sprintf('Calculated V_{max} = %d kts', round(V_max_knots)), 'Location', 'SouthEast');
grid on;
```

Figure 83. Matlab script for performance estimations

REFERENCES

[1] Teal Group Corporation, *World Power Systems Briefing (Aero): General Electric Catalyst Turboprops*, Feb. 2020.

[2] Honeywell Aerospace, *TPE331-10 Turboprop Engine Brochure*, Phoenix, AZ, USA, 2016.

[3] M. R. Jones, *Mechanics of Composite Materials*, 2nd ed. Boca Raton, FL, USA: CRC Press, 1999.

[4] Federal Aviation Administration, *Advisory Circular AC 20-107B: Composite Aircraft Structure*, Washington, DC, USA, 2009.

[5] B. L. Stevens, F. L. Lewis, and E. N. Johnson, *Aircraft Control and Simulation*, 3rd ed. Hoboken, NJ, USA: Wiley, 2015.

[6] K. J. Åström and R. M. Murray, *Feedback Systems: An Introduction for Scientists and Engineers*. Princeton, NJ, USA: Princeton Univ. Press, 2008.

[7] R. W. Beard and T. W. McLain, *Small Unmanned Aircraft: Theory and Practice*. Princeton, NJ, USA: Princeton Univ. Press, 2012.

[8] Federal Aviation Administration, *14 CFR Part 107: Small Unmanned Aircraft Systems*, Washington, DC, USA, 2016.

[9] Rolls-Royce plc, *The Jet Engine*, 6th ed. Derby, U.K.: Rolls-Royce plc, 2015.
[10] National Aeronautics and Space Administration, *Technology Readiness Level Definitions*, Washington, DC, USA, 2012.

[11] L3Harris Technologies, *WESCAM MX-20 EO/IR Imaging System Datasheet*, Melbourne, FL, USA, 2023.

[12] L3Harris Technologies, *WESCAM MX-20D Multi-Sensor Targeting System Datasheet*, 2023.

[13] Teledyne FLIR LLC, *Star SAFIRE HD Electro-Optical/Infrared System Datasheet*, Wilsonville, OR, USA, 2022.

[14] L3Harris Technologies, *WESCAM MX-15 EO/IR System Specifications*, 2022.

[15] Trakka Systems, *TrakkaCam TC-300 Product Overview*, 2023.

[16] Shield AI / IMSAR, *SPECTRUM 500 EO/IR Payload Specifications*, 2022.

[17] INYYO, *Q355 EO/IR Gimbal Payload Product Specifications*, 2023.

[18] Northrop Grumman Corporation, *AN/ZPY-3 Multi-Platform Radar Technology Insertion Program (MP-RTIP) System Overview*, 2021.

[19] General Atomics Aeronautical Systems Inc., *Lynx Multi-mode Radar Datasheet*, Poway, CA, USA, 2022.

[20] Raytheon Technologies, *Active Electronically Scanned Array (AESA) Airborne Radar Systems Overview*, 2023.

[21] ASELSAN A.S., *MURAD AESA Airborne Fire Control Radar Specifications*, Ankara, Turkey, 2023.

[22] IMSAR LLC, *NSP Series NanoSAR Radar Product Sheet*, Springville, UT, USA, 2022.

[23] Grepow Battery Co., Ltd. (Tattu), *6S 16000mAh LiPo Battery Datasheet*, Shenzhen, China, 2023.

[24] HobbyKing, *Turnigy Graphene LiPo Battery Technical Specifications*, 2022.

[25] DJI, *TB60 Intelligent Flight Battery User Guide and Specifications*, Shenzhen, China, 2023.

[26] Concorde Battery Corporation, *RG-390E Aircraft Battery Specifications*, West Covina, CA, USA, 2022.

[27] RTCA, *DO-160: Environmental Conditions and Test Procedures for Airborne Equipment*, Washington, DC, USA, 2010.

[28] RTCA, *DO-178C: Software Considerations in Airborne Systems and Equipment Certification*, 2011.

[29] U.S. Department of Defense, *MIL-STD-810: Environmental Engineering Considerations and Laboratory Tests*, 2019. NATO, *STANAG 4586: Standard Interfaces of UAV Control System (UCS)*, 2017.

[30] NATO, *STANAG 4671: UAV System Airworthiness Requirements (USAR)*, 2019.

[31] United Nations, *UN Manual of Tests and Criteria, Section 38.3: Lithium Battery Testing Requirements*, 2020.

[32] Federal Aviation Administration, *Technical Standard Order TSO-C173: Aircraft Lithium Batteries*, Washington, DC, USA, 2016.

[33] Federal Aviation Administration, *Airworthiness Standards: Normal Category Airplanes*, 14 CFR Part 23.

[34] Federal Aviation Administration, *Airworthiness Standards: Transport Category Airplanes*, 14 CFR Part 25.

[35] Federal Aviation Administration, *General Operating and Flight Rules*, 14 CFR Part 91.

[36] European Union Aviation Safety Agency, *Certification Specifications for Normal and Transport Category Aero planes (CS-23/25)*, Cologne, Germany.

[37] European Union Aviation Safety Agency, *Special Condition Light Unmanned Aircraft Systems (SC-LUAS)*, Cologne, Germany.

[38] U.S. Department of Defense, *Flying Qualities of Piloted Aircraft*, MIL-STD-1797, 2016.

[39] U.S. Department of Defense, *Environmental Engineering Considerations and Laboratory Tests*, MIL-STD-810H, 2019.

[40] U.S. Department of Defense, *Airworthiness Certification Criteria*, MIL-HDBK-516C, 2014.

[41] NATO, "STANAG 4761: Airworthiness Requirements for Unmanned Aircraft Systems," 2019. Available: https://nso.nato.int/.

[42] NATO, "STANAG 4586: Standard Interfaces of UAV Control System (UCS) for NATO UAV Interoperability," 2017. Available: https://nisp.nw3.dk/coverdoc/nato-stanag4586ed4.html.

[43] RTCA, *Environmental Conditions and Test Procedures for Airborne Equipment*, DO-160G, Washington, D.C., 2010.

[44] RTCA, *Software Considerations in Airborne Systems and Equipment Certification*, DO-178C, Washington, D.C., 2011.

[45] Z. S. Spakovszky, "The Breguet Range Equation," *Unified Engineering Thermodynamics*, Massachusetts Institute of Technology. [Online]. Available: https://web.mit.edu/16.unified/www/FALL/thermodynamics/notes/node98.html. [Accessed: March 20, 2026].

[46] Honeywell International Inc., *Embedded GPS/INS (H-764 EGI) Navigation System*, accessed Mar. 2026.

[47] Curtiss-Wright Defense Solutions, *Parvus DuraCOR 8043 Small Form Factor Mission Computer*, accessed Mar. 2026.

[48] Collins Aerospace (RTX), *Pro Line Fusion Flight Deck Avionics System*, accessed Mar. 2026.

[49] Mercury Systems, *Embedded Sensor Processing Product Guide (Ensemble Series)*, 2019

[50] General Atomics Aeronautical Systems, Inc., *Unmanned Aircraft Systems and Ground Control Architecture*, accessed Mar. 2026.

[51] RC Aero Notes, *"Canard Design Notes,"* Jan. 2017. [Online]. Available: https://rcaeronotes.wordpress.com/wp-content/uploads/2018/02/canard-design-notes-1-20-2017.pdf

[52] GabeFPV, *"Canard Design and Aerodynamic Theory,"* YouTube, [Online]. Available: https://www.youtube.com/

[53] SimScale GmbH, *SimScale: Cloud-Based Simulation Software*, Munich, Germany, 2026. Available: https://www.simscale.com